TECHNISCHE UNIVERSITÄT WIEN

DIPLOMARBEIT

Solution-processed Mg doped ZnO as buffer films for thin film photovoltaics

Ausgeführt am Institut für Physikalische Chemie
der Universität Wien

unter der Anleitung von Univ.-Prof. Dr. Wolfgang Kautek

eingereicht an der Technischen Universität Wien durch

Nina Winkler, BSc
1026695

Untere Augartenstraße 19/2/14
A-1020, Wien

Wien, am 10.05.2016

Contents

List of Figures

Acknowledgements

My first words of gratitude go to my supervisor Dr. Theodoros Dimopoulos from the Austrian Institute of Technology for his support and help. He helped me to focus and order my ideas. Special thanks go also to all colleges from AIT who let me enjoy the time working there. Especially Stefan who helped me with my first experiments and Jakob with whom I always had fun in the office or over a cup of coffee.

Further I want to thank my university supervisor Dr. Wolfgang Kautek, who offered to supervise my thesis. Discussions and his advice have been proven very useful to put this thesis together.

Further it is very important for me to thank my parents. Without them I would not have had the possibility to study chemistry in Vienna. They were always very supportive. I want you to know how thankful I am for having this oppurtunity and wish that you are proud of me.

Another important person in my life is my boyfriend Klaus. He always knows how to make me smile and listened to countless stories about my experiments – or at least pretended to. Thanks for your support!

Last but not least I want to thank my friends with whom I spend most of my days in the last 6 years, especially Lisi and Johanna. Special thanks to Manu who I met on my first day of university and became my best friend. I appreciate all the fun we had when we were chatting, laughing and drinking a glass of wine.

Abstract

The subject of this thesis is the development of a chemical bath deposition (CBD) route for magnesium doped zinc oxide (ZnMgO) - a wide band, n-type semiconductor material. ZnMgO is relevant for a wide range of applications, among others for optical coatings, optoelectronic devices (such as touch screens and light emitting diodes) and thin film photovoltaics (TFPV). In the last case, where this thesis focuses, ZnMgO is mainly investigated as buffer layer, combined with chalcogenide (Cu-In-Ga-S(Se) and CdTe), kesterite (Cu-Zn-Sn-S(Se)) or oxide (e.g. Cu2O) absorbers [1], [2]. The motivation to use ZnMgO does not only arise from its appropriate and tunable electronic properties (such as the band-gap width), but also from the fact that it consists exclusively of earth-abundant and non-toxic elements.

To achieve high power conversion efficiency in a solar cell, the band-offset between buffer layer and absorber is a critical parameter. The commonly used buffer layer material that matches absorbers of well-established thin film technologies, namely cadmium telluride (CdTe) and Cu-In-(Ga)-S(Se) (CIGS), is the toxic cadmium sulfide (CdS). The replacement of this enviromentally harmful material with alternatives that possess similar or better properties, is of outmost importance, as it will render TFPV more attractive for large scale implementation. ZnMgO has the benefit of a tunable band gap (3.37 - 4 eV) [3] depending on the Mg content in the ZnO lattice, which can be used to optimize band offsets with various absorber materials.

So far, ZnMgO films were mainly deposited by vacuum techniques. In order to lower the production costs, simple methods without expensive equipment, like chemical bath deposition (CBD), are desired. The available literature on solution-processed ZnMgO films is very limited. This thesis provides a fundamental investigation on the CBD of ZnMgO films. The solution chemistry was theoretically examined via speciation modelling. Experimentally it was found that deposition is only possible in a narrow pH window, due to the pH-dependent supersaturation of $Zn(OH)_2$ as a precursor for ZnO. The highest amount of magnesium incorporated into the ZnO lattice was 2.1%, quantified via inductively coupled plasma – optical emission spectroscopy measurements, suggesting that further incorporation is not possible, due to the thermodynamic solubility limit of 4 mol% under equilibrium conditions [4]. Although the achieved band-gap variation of 3.43-3.55 eV for the deposited ZnMgO films is moderate, the smooth, orientated and highly transparent (>80%) films, have implementation potential as buffer layers in solar cells .

It was further shown by X-ray diffraction, that the amount of certain Mg species in the solution defines the ZnO film morphology. The cause of this, is most likely face-selective adsorption of the bulky $[MgCit]^-$, as well as Mg^{2+} and $Mg(OH)^+$ species onto

specific ZnO faces. Film morphologies with dominant (100), (101) or (002) ZnO crystal faces were observed depending on the solution composition. Further, a correlation between Mg incorporation and the growth mechanism was proposed. The precise control of the surface morphology allows to optimize the absorber/buffer interface and therefore the conversion efficiency. The ZnMgO films were finally implemented into a Cu_2O/ZnMgO type of solar cell, showing rectification characteristics and leading to measurable photovoltaic performance.

Zusammenfassung

Das Thema dieser Arbeit war die Entwicklung eines chemischen Badabscheidungsprozesses (CBD) für Mg dotiertes ZnO (ZnMgO) - ein n-Typ Halbleitermaterial mit großer Bandlücke. ZnMgO ist ein interessantes Material für eine vielfältige Anzahl von Anwendungen, wie beispielsweise optische Beschichtungen, optoelektronische Anwendungen (wie Touchscreens und Leuchtdioden (LEDs)) und in der Dünnfilmphotovoltaik (DFPV). Diese Arbeit fokusiert sich auf die Anwendung in der DFPV, wobei hierfür hautsächlich der Einsatz von ZnMgO als Bufferschicht in Kombination mit Absorbermaterialien wie Chalkogenid (Cu-In-Ga-S(Se)) und CdTe), Késterit (Cu-Zn-Sn-S(Se)) oder Oxide (z.B. Cu_2O) betrachtet wurde [1], [2]. Die ausgezeichneten elektronischen Eigenschaften (wie die große Bandlücke), sowie die Zusammensetzung dieses Materials aus ausreichend vorhandenen und ungiftigen Elementen, waren die Beweggründe ZnMgO zu verwenden.

Der Bandabstand zwischen Absorber- und Bufferschicht ist ein kritischer Aspekt für die Energieumwandlungseffizienz einer Solarzelle. Das momentan meistgenutzte Bufferschichtmaterial für Absorber von hochetablierten Dünnfilmtechnolgien, wie beispielsweise CdTe oder Cu-In-(Ga)-S(Se) (CIGS), ist das giftige Kadmiumsulfid (CdS). Das Interesse dieses Material durch eine umweltfreundliche Variante mit ähnlich herausragenden Eigenschaften zu ersetzen, ist enorm und würde die DFPV attraktiver für large-scale Anwendungen machen. ZnMgO hat außerdem den Vorteil einer variablen Bandlücke (3.37 - 4 eV) [3], welche vom Mg-Dotierungsgehalt im ZnO Gitter abhängt und daher für die Optimierung des Materials mit verschiedenen Absorberschichten genutzt werden kann.

ZnMgO Filme wurden bis jetzt hauptsächlich mittels vakuumbasierenden Methoden abgeschieden. In der Herstellung billiger Dünnfilmsolarzellen werden jedoch einfache, lösungsbasierende Methoden ohne erforderliches teures Equipment, wie die chemische Badabscheidung, bevorzugt. Literatur über ZnMgO Filme ist nur im geringen Außmaß vorhanden. Diese Arbeit beinhaltet eine grundlegende Erforschung der chemischen Badabscheidung von ZnMgO Filmen. Die Chemie des Lösungsbades wurde theoretisch modelliert mittels Speziierungsdiagramen. Experimentell konnte festgestellt werden, dass die Abscheidung aufgrund der pH abhängigen Übersättigung von $Zn(OH)_2$ als Vorstufe für ZnO, nur in einem schmalen pH Bereich möglich ist. Mittels optischer Emissionspektroskopie konnte der höchste Mg Gehalt im ZnO Gitter mit 2.1 mol% ermittelt werden. Dies deutete darauf hin, dass eine höhere Dotierung mit Mg aufgrund des thermodynamischen Lösungslimits von 4 mol%, nicht möglich ist [4]. Es konnten ZnMgO Filme mit Bandlücken von 3.43 - 3.55 eV abgeschieden werden. Obwohl diese Bandbreite sehr gering ist, könnten die homogenen, orientierten

sowie sehr transparenten (>80%) Filme, sinnvoll als Bufferschichten in Kombination mit ausgewählten Absorbern verwendet werden.

Es konnte außerdem mittels Röntgenstrukturanalyse gezeigt werden, dass über den Gehalt bestimmter Mg Spezies in der Lösung die ZnO Film-Morphologie definiert werden kann. Der Grund hierfür ist hauptsächlich die oberflächenselektive Adsorption des $[MgCit]^-$ Komplexes, sowie von Mg^{2+} und $Mg(OH)^+$, auf spezifische ZnO Oberflächen. In Abhängigkeit der Lösungszusammensetzung, wurden Film Morpholgien mit dominanten (100), (101) und (002) ZnO Kristallorientierungen beobachtet. Des Weiteren wurde vorgeschlagen, dass der eingelagerte Mg-Gehalt vom Wachstumsmechanismus des Filmes abhängt. Die präzise Kontrolle der Oberflächenstruktur kann für die Optimierung der Grenzfläche zwischen Absorber- und Bufferschicht genutzt werden, was die Energieumwandlungseffizienz der Solarzelle immens verbessern könnte. Schlussendlich wurden die hergestellten ZnMgO-Filme erfolgreich in einer funktionsfähigen Cu_2O/ZnMgO Dünnfilmsolarzelle eingesetzt und deren Eigenschaften gemessen.

List of abbreviations and symbols

ALD	atomic layer deposition
a-Si	amorphous silicon
AZO	aluminium doped zinc oxide
BG	band gap
CA	citric acid
CB	conduction band
CBD	chemical bath deposition
CBM	conduction band maximum
CVD	chemical vapor deposition
DFPV	Dünnfilm-Photovoltaik
E_g	band gap
FTIR	fourier-transform infrared spectroscopy
HMTA	hexamethylenetetramine
ICP OES	inductively coupled plasma atomic emission spectroscopy
ITO	indium doped tin oxide
LED	light emitting diode
MBE	molecular beam epitaxy
MEMS	micromechanical system
$Mg_xZn_{1-x}O$	Mg doped ZnO with various amount x of Mg
MOCVD	metal organic chemical vapor deposition
PLD	pulsed laser deposition
PV	photovoltaic
SEM	scanning electron microscope
SILAR	successive ionic layer adsorption and reaction
TCO	transparent conducting oxide
TFPV	thin film photovoltaic
UV	ultraviolet
VB	valence band
VBM	valence band maximum
XRD	x-ray diffraction
ZnMgO	ternary oxide compound of ZnO and MgO

1 Introduction

The 21st conference of the U.N. on climate change held in 2015 in Paris ended in an agreement to limit the global temperature increase below 2 degrees Celsius [5]. The increasing awareness of the climate change and exhaustion of natural resources causes our society to invest in renewable energies. Besides hydro and wind power, photovoltaic systems is the third most important renewable energy source. This can be demonstrated in the increasing amount of global cumulative installed PV capacity (see Figure 1.1). Solar PV already covers more than 7 % of total electricity in 3 european countries (Italy, Germany, Greece) and solar power is predicted to grow in Europe by 80% by 2019 [6].

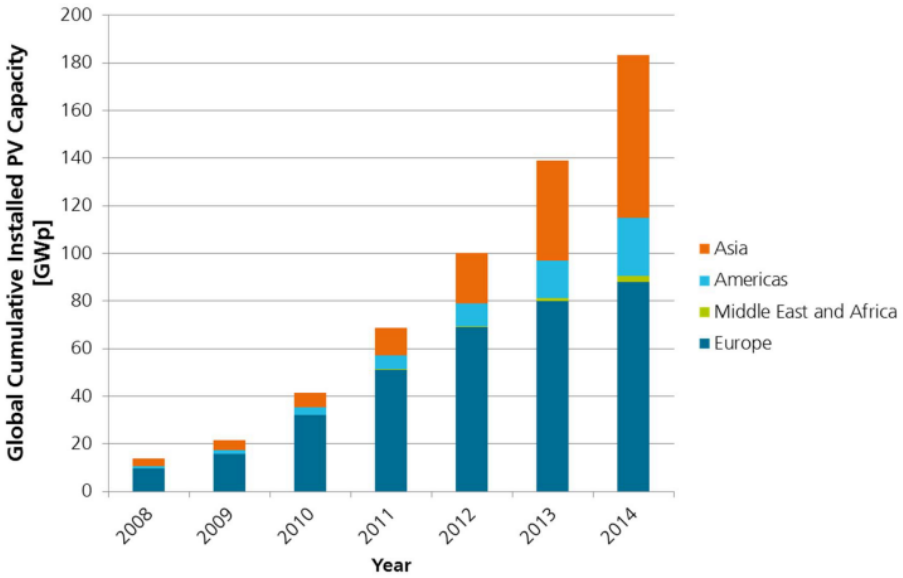

Figure 1.1: Global Cumulative Installed PV Capacity [7]

The photovoltaic market is mainly dominated by the silicon technology. Other technologies include GaAs, various thin-film or other emerging photovoltaics. Figure 1.2 shows global PV production by technology between 1980-2014. Only a small fraction of global PV production accounts for thin film photovoltaics (TFPVs). TFPV production is very unstable. Si production has a major influence on thin film technolgies. An abrupt decrease in Si production costs, can cause the insolvency of many thin film companies, because their module prices are not marketable anymore. But thin film solar cells have certain benefits compared to conventional Si technolgies. Since compared to Si, direct semiconductors are used as absorbers, less material is needed for the much thinner cells. Thin film cells are a few μm thick compared to Si with around

200 μm in thickness. Because of their low thickness, these cells can also be fabricated on flexible substrates, opening the way to many new applications. To increase the fabrication throughput, roll-to-roll processing is an interesting concept, which can only be realized with flexible solar cells. For this type of fabrication, film deposition has to be carried out by suitable methods, such as solution-based, non-vacuum methods.

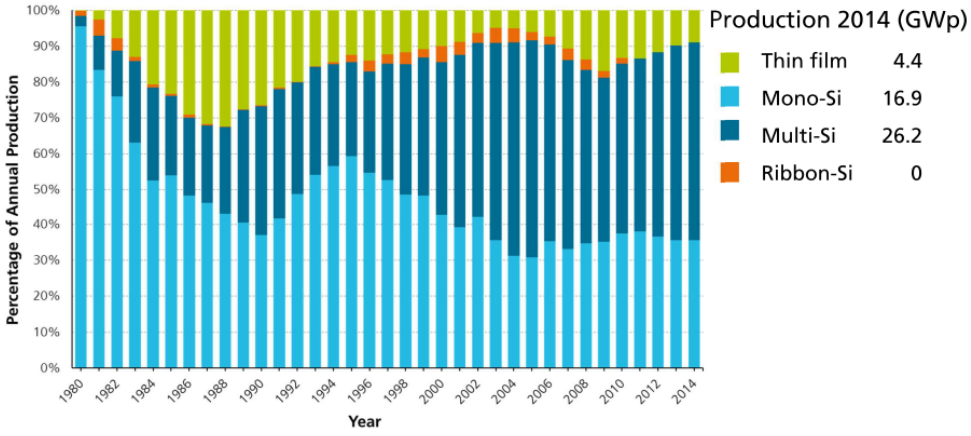

Figure 1.2: Global PV Production by Technology 1980-2014 [7]

Among thin film technologies, CIGS (Cu,In, Ga, S and/or Se) solar cells are one of the most promising technolgies, with current laboratory cell efficiency records of 22.3% (Solar Frontier [8]). In terms of thin film PV market share, CdTe is the most successful technology with current commercial module efficiencies of 16.4 % [9]. One of the main challenges for all thin film technolgies is to achieve also high efficiency in commercial modules. For commercial CIGS modules from Solar Frontier the efficiency is under 14% [7].

For emerging thin film technolgies to compete with already commercialized technologies, they have to be high efficient, while their production costs should be much lower. Besides that, durability and earth-abundance of used materials is very important. This causes following requirements for thin film photovoltaic materials [10]:

- low cost
- high abundance
- non-toxicity
- no degredation effects

The price of materials is also dependent on the abundance of the elements. Figure 1.3 shows that certain materials used for CIGS and CdTe solar cells are among the rarest elements. Especially for tellurium a significant supply shortage is expected, due to the increasing CdTe PV production volume [11]. Besides that, Cd is a toxic material and its emissions have to be reduced for the human health as well as the enviroment [12]. Apart from abundance and toxicity, also political risks associated with the main producing countries of certain materials, have to be considered. For example indium, which is used in absorbers of CIGS solar cells as well as transparent conducting electrode (as indium doped tin oxide ITO), is mainly produced in China (58%) [13].

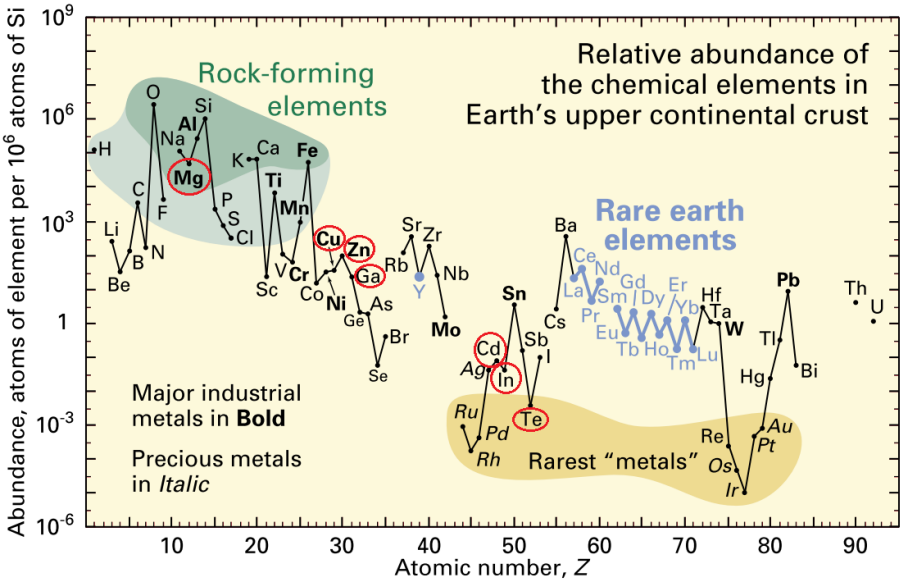

Figure 1.3: Abundance of chemical elements in Earth's upper crust as function of atomic number, red cycled elements relevant to thin film technolgies or this thesis (Modified from [14])

Table 1.1: Thin film technology with latest efficiency records

Technology	Lab cell efficiency	Manufacturer	Ref.	Main problems
a-Si	13.6%	AIST	[15]	low efficiency
CdTe	22.1%	First Solar	[15]	toxicity of Cd, low abundance of Te
CIGS	22.3%	Solar Frontier	[15]	toxicity of Cd, low abundance/political risks of In
CZTS	12.6%	IBM	[16]	low efficiency

Table 1.1 gives a short overview of the most important thin film technolgies with their latest laboratory cell efficiency records. It can be seen, that CIGS and CdTe are the most promising technologies. Besides the low abundance of Te and In both of these technologies use Cd. In both technologies, CdS is usually applied as buffer layer. An alternative to CIGS, using only high abundant materials, is the CZTS (Cu, Zn, Sn, S or Se) absorber material. But also in this case CdS is often used as buffer layer [16].

The buffer layer is essentiell to create a junction with the p-type absorber and drive carriers to the electrode for generating electricity. CdS is the material of choice for CIGS and CZTS because of the suitable band offset to the absorber layer. This band offset is very important to create high efficient solar cells. Up to now no appropriate replacement for CdS has been found. Possible candidates are In_2S_3, Zn(O,S,OH) as well as ZnMgO [17], [18]. Whereas In_2S_3 contains the rare In, the other candidates are composed of abundant elements. One of the most promising candidates is Mg doped ZnO. ZnO on its own, does not align well with CIGS and CZTS absorber conduction

band maxima. But if ZnO is doped with Mg its band gap increases as a function of doping. Therefore the conduction band maximum is shifted to align well with these absorbers. It was shown recently that record cell efficiencies in Cu(In,Ga)S_2 solar cells can be achieved with ZnMgO-buffer layers instead of CdS [19]. This is only one of many publications adressing the potential of Mg doped ZnO as alternative buffer layer material [17], [20], [21]. Also in combination with cuprous oxide (Cu_2O) as p-absorber, ZnMgO is considered a suitable buffer layer material [22]. It was shown by [23] that highest efficiences of 4.31% can be achieved with a 50nm thick $Zn_{0.91}Mg_{0.09}O$ buffer layer.

However, so far ZnMgO films were almost entirely deposited with vacuum-based techniqes such as pulsed laser deposition (PLD) [3] or sputtering [24]. In order to reduce capital investment and reduce the overall PV module production costs, non-vacuum techniques are preferred. Especially solution-based film deposition approaches are desirable, because of their simplicity and their potential to be integrated in a roll-to-roll fabrication process. When switching to non-vacuum methods, the same material performance has to be ensured. Remarkable research work towards all solution-processed CIGS solar devices was demonstrated by [25]. A review by Habas et al. [26] also points out the potential of solution-based methods for thin film photovoltaics.

Among various solution-based methods, chemical bath deposition has been proven sucessful in the deposition of high-quality thin films. Chemical bath deposition is commonly used in the deposition of CdS buffer layers, also in commercial production processes. ZnO has already been sucessfully deposited by chemical bath deposition. There are many references using chemical bath deposited ZnO as buffer layer in CIGS solar cells such as [27] and [28]. In the latter one, $Mg(OH)_2$ was also applied as a possible buffer layer opening the way to Mg doped ZnO films. These previous works make the chemical bath deposition technique obviously very interesting for $Zn_{1-x}Mg_xO$ thin films. Therefore this thesis deals with Mg doped ZnO films deposited from a chemical solution.

This thesis is organized as follows. Firstly fundamental reasons why this certain topic was investigated, are given. To understand the theoretical background, properties, doping behaviour and deposition techniques for ZnO and also for $Zn_{1-x}Mg_xO$ thin films are explained in chapter 3. Since deposition of $Zn_{1-x}Mg_xO$ films should end in the fabrications of a test solar cell, the principles of photovoltaic cells are explained in the same chapter. Further, used characterization methods for the deposited films are presented shortly in chapter 4. To understand the solution chemistry behind the chemical bath deposited ZnO and $Zn_{1-x}Mg_xO$ films, chapter 5 explains why a certain composition of precursors in the bath was used. To get insight on the deposition mechanism, speciation models were examined for various solution compositions. Finally chapter 6 presents and discusses the experimental results and chapter 7 concludes this thesis with a short presentation of the main achievements within this thesis. To see in which direction more research concerning this topic should be done, the same chapter looks into future application perspectives of ZnMgO films.

2 Research Objectives

The key goal within this thesis was to deposit Mg doped ZnO films by chemical bath deposition method for potential thin film photovoltaic applications.

This project was motivated by many recent approaches towards solution-based film deposition for thin film photovoltaics such as [25]. Compared to vacuum-based techniques, these methods offer following advantages:

- low capital investment for deposition equipment
- high solar cell fabrication throughput via roll-to-roll processing
- fabrication of flexible solar cells

These benefits over other techniques result in fast and low-cost fabrication of even flexible solar cells. Important is also the use of materials with high abundance, low toxicity as well as without political risks. If while considering these aspects also cell module efficiencies further increase, this makes solution-processed thin film photovoltaics the solar technology of choice for many applications. In fact, thin film photovoltaics should not be considered as a competitor to the highly developed silicon technology. Furthermore, benefits of TFPV compared to other PV technologies should be used to create new photovoltaic products. Especially the application as building-integrated photovoltaics (BIPV) is a prospective market for TFPV.

A key parameter to gain high cell efficiencies is the so-called buffer layer. Through optimization of the buffer band gap offset with the absorber layer the efficiency can be increased drastically. CdS is commonly used as buffer layer, in conventional thin film technolgies. The enviromental impact using the toxic Cd in production processes is undeniable. To avoid Cd emission, several alternatives have been proposed. A very promising candidate is Mg doped ZnO. This material, with its tunable bandgap depending on the Mg content in the ZnO lattice, is non-toxic as well as consists of the high abundant elements zinc and magnesium.

In order to combine the benefits of solution-processing as well as the high potential of Mg doped ZnO as buffer layer, chemical bath deposition was proposed as a suitable method for deposition of these films. A literature review displayed, that dense $Zn_{1-x}Mg_xO$ films were never successfully deposited via this method. Reasons for that might be the thermodynamic solubility limit of 4 at% from MgO in ZnO under equilibrium conditions [4].

To see whether Mg incorporation via chemical bath deposition under different conditions is possible and furthermore, to which extent, was the main goal within this thesis.

3 Fundamentals

3.1 Properties of ZnO, MgO and $Zn_{1-x}Mg_xO$

ZnO is a direct and wide band gap (3.37 eV at room temperature [29]) semiconductor. It also has a large exciton binding energy of 60 meV [30] which makes the material a promising candidate for optical devices based on excitonic effects. Further, ZnO films are interesting for piezoelectric applications and has been used as sensors and actuators in microelectromechanical systems (MEMS) [31]. ZnO has a strong luminescence in the green spectrum region. This enables its use in field emission displays for example.

In contrary to ZnO, MgO is an isolator with a wide band gap of about 7.7 eV [32]. Because of this, MgO films are widely used as insulating coating.

Through the substitution of Zn with Mg atoms a $Zn_{(1-x)}Mg_xO$ structure can be synthesized. These structures are known for their variable band gap, dependent on the amount of incorporated Mg atoms [33]. Layers of different band gaps are important to match valence- and conduction-band offsets for many applications. The properties of $Zn_{(1-x)}Mg_xO$ films depend strongly on the deposition method.

3.1.1 Crystal Structures

ZnO crystallizes under ambient conditions in the thermodynamically most stable wurtzite structure with the lattice parameters of a=3.2498 Åand c=5.2066 Å[34]. Other structures include zinc blende, which is only stable through growth on cubic structures and the high-pressure metastable rocksalt structure. Wurtzite ZnO has a hexagonal closed packed bravais lattice and belongs to the space group P63mc as shown in Figure 3.1. The lattice is characterized by two interconnecting sublattices of O^{2-} and Zn^{2+}. Each zinc cation ion is surrounded by four oxygen anions in a tetrahedral coordination. This configuration is responsible for the polar symmetry along the c-axis, which is also important in the growth of ZnO. Polar crystal face terminations along the c-axis are the polar Zn-terminated (002) and the O-terminated (00$\bar{2}$) faces. These two faces possess different chemical properties. The Zn-terminated phase is positively charged, while the O-terminated phase is negatively charge. Polar ZnO phases are metastable, while nonpolar "low-symmetry" faces with 3-fold coordinated atoms are the most stable ones. Non-polar faces include (100),(110) and (010) and contain equal numbers of oxyagen and zinca atoms. [35] According to [36] the stability of ZnO faces

is $(\bar{1}00) > (\bar{1}01) > (001) = (00\bar{1})$. A schematic view of some ZnO crystal faces can be seen in Figure 3.2.

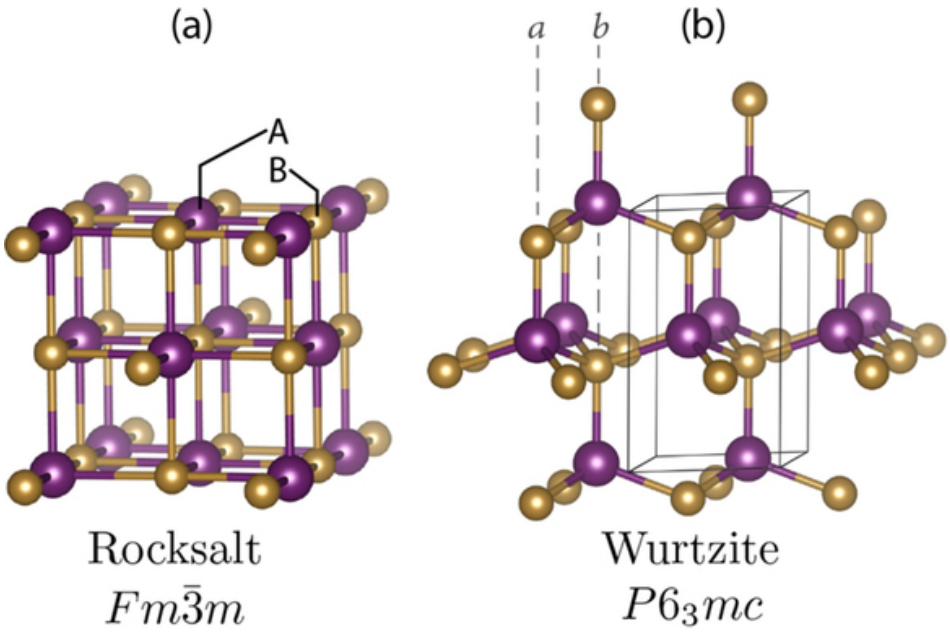

Figure 3.1: (a) Rocksalt Structure of MgO (gold: Magnesium atoms, purple: oxygen atoms) (b) Wurtzite Structure of ZnO (gold: Zinc atoms, purple: oxygen atoms) [37]

MgO crystallizes in the rocksalt structure. The cubic structure has a lattice constant a of 4.213Å[39]. Since the tetrahedral ionic radius of Mg^{2+} (0.57 Å[40]) is similar to that of Zn^{2+} (0.60 Å[40]) a replacement of Zn^{2+} ions by Mg^{2+} can be expected. The solid solution of $Mg_xZn_{1-x}O$ is of eutectic type according to the equilibrium phase diagram of the binary MgO-ZnO system [4]. It predicts a solubility limit of 4 mol% of MgO in ZnO. The solubility limit can be considerably increased at higher temperatures and high pressure. Therefore, non-eqilibrium growth processes such as molecular beam epitaxy (MBE) or pulsed-laser deposition (PLD) have to be applied. ZnMgO films with Mg content over 33 mol% have been reported [3].

$Mg_xZn_{1-x}O$ exhibits a wurtzite structure up to 40 at% incorporated magnesium ions [41]. High concentration of 50 at% incorporated magnesium ions in the lattice transforms the structure to rocksalt type. Between the two structures exists a mixed structure. This phase transformation varies with deposition technique and nature of the substrate. The crystalline structure and the composition affects the electronic properties, which gives rise to the almost linear increase of the band gap with Mg content. [42] This effect makes magnesium interesting for band gap engineering, as further discussed in subsection 3.2.3. The slightly smaller ionic radius of Mg^{2+} compared to Zn^{2+} causes a change in the lattice constants. Ohtomo et. al. [3] synthesized $Mg_xZn_{1-x}O$ films with PLD and reported an a-axis increase with higher Mg content, while the c-axis decreases with more Mg incorporated. In contrary to that $Mg_xZn_{1-x}O$ deposited with MBE showed an a-lattice paramter independent from the Mg content and a decrease in c-paramter with higher amount of Mg [43]. For chemical bath deposited

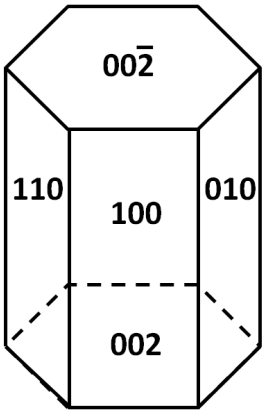

(a)Schematic view of ZnO crystal faces

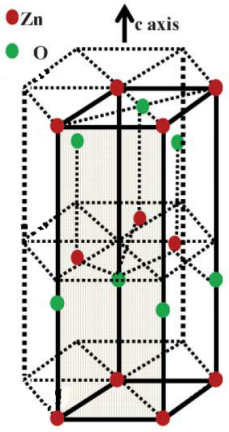

(b)O and Zn atoms in ZnO modified from [38]

Figure 3.2: Polar and non-polar ZnO crystal faces

Mg doped ZnO a very small decrease in a and c lattice paramter was reported [44] for low concentrations of incorporated Mg. These examples suggest lattice parameter dependance on the synthesis method. In general, because of the small changes in the lattice constants the cell volume remains practically unchanged.

3.1.2 Optical Properties

Optical properties are influenced by the energy band structure and the crystal lattice. ZnO is a promising material for many optoelectronic applications in the blue and UV region of the spectrum due to its high direct band gap of 3.37 eV [29] at room temperature. Due to the large free-exciton binding energy of 60 meV, stimulated emission at room temperature is possible. ZnO has also a strong luminescence in the green region of the spectrum (related to interface and bulk defects), making it appropriate for certain applications like field emission displays. [45]

Since the focus of the thesis is the application of Mg doped ZnO films as buffer layers in photovoltaic applications, the optical properties of the material have a critical significance. Light can either be reflected, absorbed or transmitted. An example of a transmittance spectrum of ZnO is shown in Figure 3.3. At short wavelengths (region (A)) with energies above the band gap, there is strong light absorption due to fundamental transitions of electrons from the valence band to the conduction band. A sharp absorption edge is observed at wavelenghts corresponding to the band gap value (region (B)). In the visible and infrared (IR) window, the transmittance presents minima and maxima due to the constructive and destructive interferences of the light reflected at the various interfaces of the coated glass. The number and position of the maxima depend on the thickness and the dispersion relation of the refractive index of the film trough the relation

$$2nd = m\lambda \quad and \quad \lambda = \frac{2nd}{m} \tag{3.1}$$

where n is the refractive index, d the thickness and m an integer for maxima and half and half an integer for minima [46]. The determination of maximum and minium value of this oscillations allows in principle a determination of zinc oxide film depth. [47]

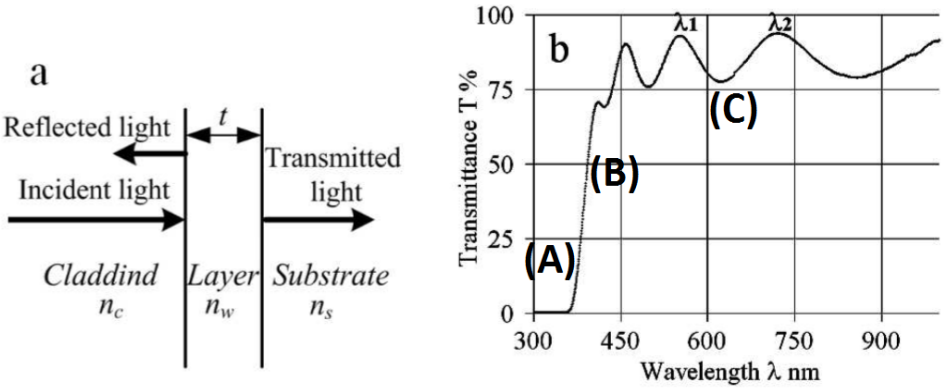

Figure 3.3: (a) Transmittance of light through a thin layer structure (b) Transmittance spectrum for ZnO [47]

MgO has in contrary to ZnO a wide bandgap of 7.7 eV [32] and is therefore electrically an isolator. The material has a higher transmittance than ZnO and is also transparent in the UV range. This and the high durability justifies the wide use of MgO as protective layer for example in AC-plasma display panels.

$Zn_{1-x}Mg_xO$ films have a higher band gap than ZnO films (further discussed in subsection 3.2.3). Therefore the absorption edge in the transmittance spectrum is shifted to lower wavelenghts causing a higher transmittance in the UV region of the spectrum. This makes $Zn_{1-x}Mg_xO$ films suitable for the fabrication of UV photodetectors.

3.2 Doping of ZnO

As clarified before, ZnO can be classified as a wide band gap semiconductor. This means the band gap between valence band maximum (VBM) and conduction band minimum (CBM) is small enough, so that electrons can be promoted from VCM to the CBM at ambient temperatures leaving positive holes in the VB. As the temperature further increases, more electrons can be excited to the CB and therefore the electrical conductivity is increasing (see also Figure 3.4 a)).

Doping of ZnO is an essential tool to tailor electrical and optical properties for certain applications. In general, doping of a semiconductor means to incorporate impurities

in the crystal structure. These impurities can either be added on purpose to provide free carriers or are unintentionally added during the growth process. If dopants are providing additional electrons to the semiconductor they are called donors. Donors form a narrow band that supplies electrons to the conduction band. This semiconductor is called n-type. If dopants add holes to the material they are called acceptors. Since in this case the dopant has fewer electrons than the host VB, they form a narrow band that accepts electrons from the VB, leaving holes in the CB. This semiconductor is called p-type (see also figure Figure 3.4 b)).

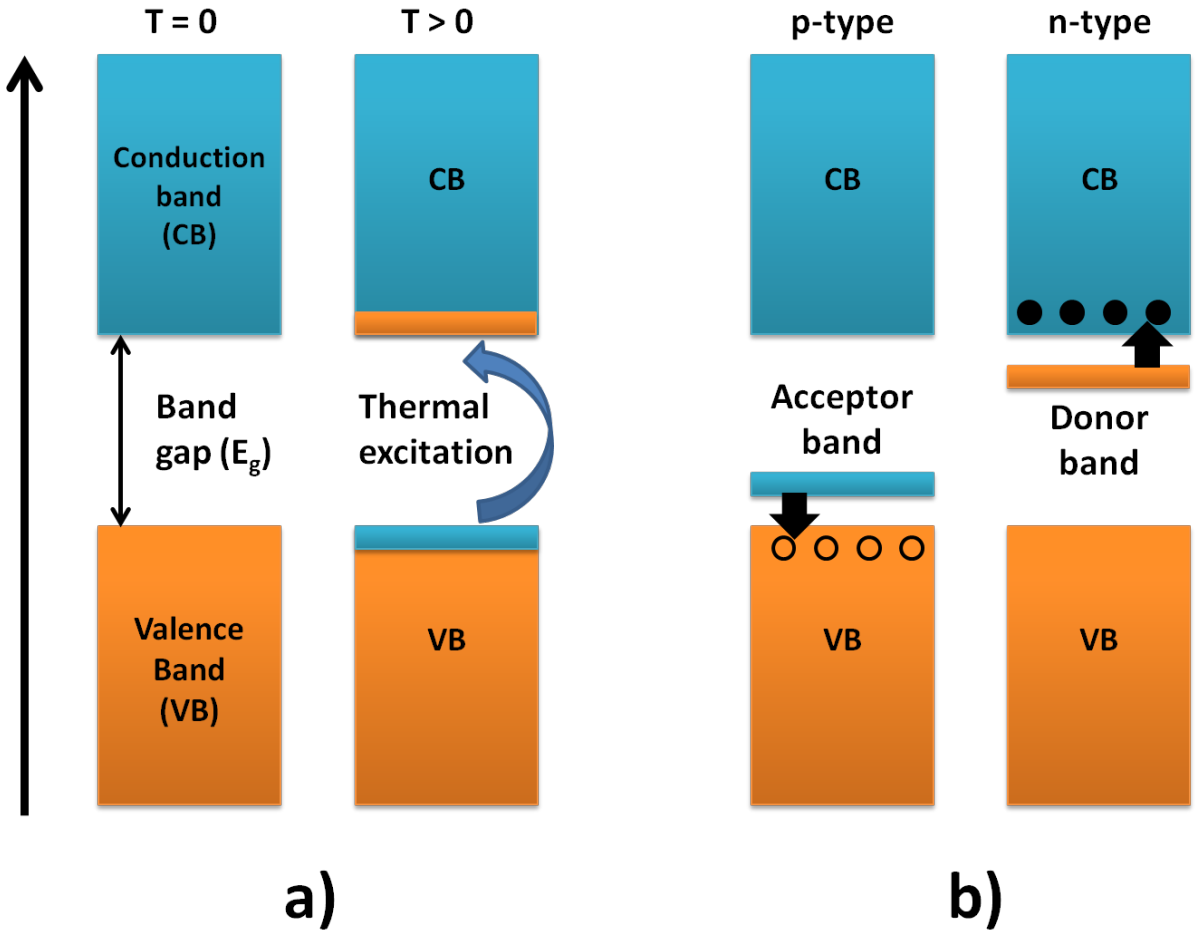

Figure 3.4: (a) Principle of a conductivity in semiconductors (b) p- and n-type doping of semiconductors

Some common used acceptor and donor impurities for ZnO doping with their tetrahedral ionic radii are listed in table Table 3.1. Besides that dopants can also be added for the purpose of band gap engineering. The most prominant dopants for this case are Mg for increasing the band gap and Cd for decreasing it.

The properties of the resulting material depend on the deposition method, film thickness and structure, growth temperature and the nature of the dopant, as well as its concentration. Most doping studies for ZnO are done with vacuum deposition methods for producing doped ZnO films such as CVD, sputtering, MBE or PLD. Hence

Table 3.1: Donor and acceptor impurities for doped ZnO

Dopant	Character	substitutes in ZnO	ionic radius [Å] [40]
H^+	Donor	oxygen	0.38
Al^{3+}	Donor	zinc	0.39
Ga^{3+}	Donor	zinc	0.47
In^{3+}	Donor	zinc	0.62
F^-	Donor	oxygen	1.31
Li^+	Acceptor	zinc	0.59
Na^+	Acceptor	zinc	0.99
K^+	Acceptor	zinc	1.37
Cu^+	Acceptor	zinc	0.6
N^{3-}	Acceptor	oxygen	1.46

the influence of dopants on solution-processed ZnO films is lacking fundamental research. Most efforts are directed towards Al doped ZnO as a replacement for indium doped tin oxide (ITO) for transparent conducting electrodes (TCOs).

As grown ZnO is unintentional n-type, the cause of which is still not entirely solved. It is crucial to understand the role of native point defects (e.g. vacancies, interstitials and antisites) and incorporation of impurities to explain the electrical properties of ZnO. It has been proposed that the unintentional n-type conductivty comes from oxygen vacancies or zinc interstitials [48]. However later on, Kohan et. al. [49] showed by first-principle studies that oxygen vacancies are deep donors and are therefore incapable of causing n-type conductivity. Zinc interstitials are shallow donors but the high formation energy limits their ability to influence the n-type conductivity [50]. The cause of the stable n-type conductivity is instead attributed to substitutional hydrogen, whereas H substitues O in ZnO [51].

3.2.1 Donor Doping

Besides H^+, as discussed before, several other dopants can contribute to the n-type conductivity of ZnO. Among them, group-III impurities such as B^{3+}, Al^{3+}, Ga^{3+} and In^{3+} are the most common ones. Besides them fluorine can also act as a shallow donor.

Group-III impurities have an extra valence electron compared to the zinc atom. They substitute. Al^{3+} is the most common dopant added to ZnO (AZO). Carrier concentrations up to $8 \cdot 10^{20} cm^{-3}$ were obtained. In table Table 3.1 the ionic radius of Al^{3+} and other group-III dopants can be found. To compare, Zn^{2+} has a tetrahedral ionic radius of 0.6 Å. So Al^{3+} and Ga^{3+} have smaller ionic radii than Zn^{2+} causing a reduction in lattice parameter if they are substitutionally incorporated. In^{3+} has almost the same ionic radius to Zn^{2+}, thus when incorparated the lattice constants do not change a lot. Al^{3+} can be incorporated beyond the thermodynamic solubility limit. The conductivity of the Al doped ZnO (AZO) film increases till an Al concentration of 7 at% in the

lattice. Further Al incorporation causes a decrease in conductivity [52]. Due to its high conductivity AZO is widely used as transparent conducting oxide and is considered replacing the costly ITO. Applications of AZO are in displays, LED or in solar cells.

Fluorine has, compared to oxygen, one more electron and almost the same ionic radius as the oxygen ion (1.37 Å). Therefore it can act as a shallow donor in ZnO. Fluorine incorporation causes a large displacement of one of the neighboring Zn atoms. Because of that, the bond between the F atom and one of its Zn neighbors is broken [53].

As discussed before, incorporation of hydrogen is thought to be the reason for the unintentional n-type conductivity of ZnO. Sine hydrogen is present in all growth techniques this explanation is plausible. Hydrogen as dopant is a so called amphoteric impurity. This means that in p-type materials it is incorporated as H^+ and in n-type materials as H^-. However as dopant in ZnO it can only incorporated as H^+ donor forming a very strong bond with an oxygen atom [53].

3.2.2 Acceptor Doping

So far, acceptor doping has been a challenging task compared to the easy achievable n-type doping. This doping asymmetry problem is well known and inhibits ZnO device fabrication (homojunction), where both types of doping are essential. One reason for that is, that the defects causing unintentional n-type conductivity can self-compensate other acceptor dopants.

To overcome the difficulties in p-type doping, several approaches have been investigated [54]. One technique is to substitute Zn sites with group I elements such as Li, Na or K. There are only limited reports of Li as sucessful acceptor dopant in ZnO because Li substitution is relatively unstable to higher temperatures [55]. Altough it can be used to compensate n-type doping in the so called co-doping method. Besides that, also Na and K could not used sucessfully p-type ZnO doping.

Nitrogen would probably be the most suitable candidate to achieve p-doped ZnO, due to the similar ionic radius compared to oxygen. There are several publications on N doped ZnO produced with various methods such as PLD [56] or MBE [57]. Nitrogen can for example be incorporated by fluxing with N_2 gas during deposition. In contrast to this, many reports using theoretical calculations indicated that nitrogen can not act as a shallow acceptor [58]. In fact, there are many publications giving reasons why nitrogen doping can be mistaken for p-type conductivity [59]. A simple explanation gives the band structure of ZnO and nitrogen [60]. The valence band maximum arising from the O 2p orbitals in ZnO is 2.9 eV higher than the N 2p orbitals. Therefore, N can not be a shallow acceptor for ZnO. Other group V elements such as P, As or Sb are also not suitable acceptor doping candidate, because their p-orbitals are even higher in energy than nitrogen.

3.2.3 Doping for Tuning the Band Gap

Tailoring the band gap of ZnO (3.37 eV) opens a wide range of new applications for this material. Many semiconductor devices need a heterojunction for providing carrier or optical confinement. These electronic and optoelectronic devices consist of layers with specific band gaps as well as definded valence- and conduction band offsets between the layers. The preferred choice for band-gap engineering materials are compounds with group-II metal oxides like MgO or CdO. An alternative to them is ZnS. If ZnO is alloyed with MgO the band gap increases while with CdO smaller band gaps can be achieved.

Because of the similiar tetrahedral ionic radii of Mg^{2+} (0.57 Å) and Zn^{2+} (0.6 Å), alloying with these materials induces almost no stress in the lattice. With Mg the band gap can be tuned in a wide range. Experimentally it was found that the band-gap increases almost linearly with Mg content [33]. As seen in Figure 3.5 the slope for the cubic ZnMgO is double as high as for hexagonal ZnMgO.

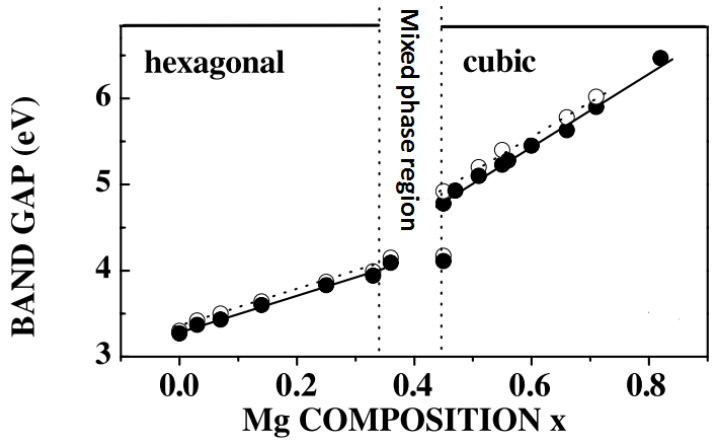

Figure 3.5: Band gap energies dependent on Mg content in ZnO (adapted from [61])

First-principle studies revealed that the band gap widening of $Zn_xMg_{1-x}O$ with higher Mg content is due to the decrease of Zn 4s states [62].

There have been numerous publications on studying this material over the last decade. Nevertheless, reports on solution-based deposition methods for ZnMgO films are relatively rare. An overview of $Zn_xMg_{1-x}O$ (ZMO) film depositions by various methods is given in section 3.3.

3.3 Deposition Techniques for ZnO and $Zn_(1-x)Mg_xO$ thin Films

A thin film is in general a material created by random nucleation and growth process of various species on a substrate. The thickness range is between a few nm up to a few μm.

The preparation of ZnO and ZnMgO thin films often demands a controlled morphology and thickness. In this section various methods commonly used for depositing thin films, will be presented shortly. The focus will lay on techniques that are suitable for deposition of ZnO and ZnMgO.

Thin film deposition techniques can generally be classified in physical and chemical methods. Physical methods include various evaporation methods and sputtering. Chemical deposition can be divided in gas phase and liquid phase methods as shown in graph Figure 3.6. The most relevant techniques for this thesis are the solution-based techniques therefore they are discussed in more detail.

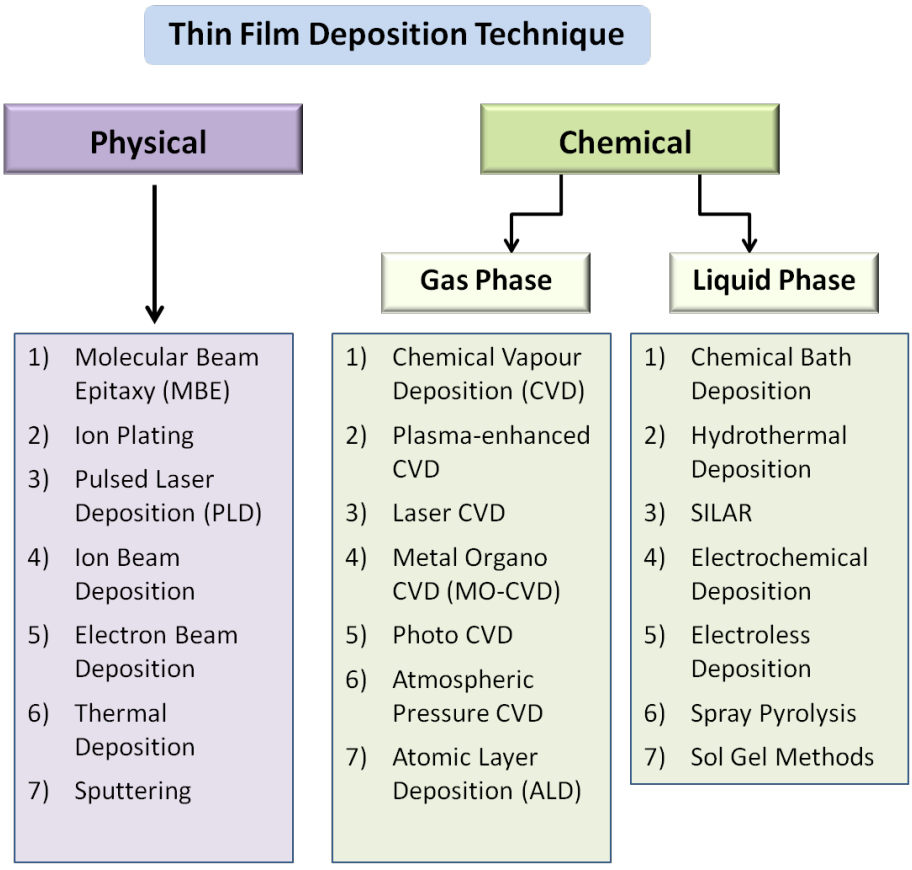

Figure 3.6: Chemical and Physical Deposition Techniques

3.3.1 Physical Deposition

In general, physical methods involve the transfer of material vapor to the substrate resulting in the deposition of a thin film. The vapor can be generated via evaporation or sputtering. Evaporation is usually performed under high vacuum conditions. Therefore, this methods are also called vacuum deposition methods.

Some commonly used physical methods for the deposition of ZnO and ZnMgO are molecular beam epitaxy (MBE) and pulsed laser deposition (PLD). Besides that also various types of sputtering are frequently used.

Molecular beam epitaxy [63] is a thin film deposition method were an epitaxial (which means surface arranged) film, grows on a substrate under ultrahigh vacuum. Solid source materials are evaporated to form a molecular beam, which reacts with the substrate surface. Reactive oxygen is provided through a radio frequency plasma source for oxidizing metals (e.g. ZnO). Through alteration of the evaporation rate of the source materials, different film compositions or doping levels can be achieved. The substrate is heated, so that the enhanced surface mobility of atoms allows them to migrate to favorable sites. The growth rate is very low around but very smooth films are deposited. Because of the slow deposition process, the method is only useful for producing high quality thin films (nm range). Advantages of MBE compared to other physical vacuum deposition methods is the precise control of growth conditions. Growth is mainly governed by kinetics of surface processes far away from thermodynamic equilibrium conditions. This makes the method especially interesting for depositing thin Mg doped ZnO films, because the phase diagram of MgO-ZnO shows only low solubility of Mg in ZnO under equilibrium conditions as discussed in detail in subsection 3.1.1.

In the pulsed laser deposition [64] a laser beam ablates from the target material. Each laser pulse vaporizes a small amount of material. The thus created material plasma plume provides the flux for the film growth on the substrate. Through the choice of the laser wavelength and pulse rate, different species (e.g. atomic or diatomic) of the material in the plasma can be generated. The target material should have a high optical absorption coefficient at the selected laser wavelength. As targets, ceramics or single crystals are often used. A background gas, such as oxygen, can react with the ablated species to produce for example oxides. Advantage of PLD is the stochiometric transfer of material from the targets. Therefore, a target material, which contains different cations, provides approximately the same composition in the resulting film. Similiar to MBE, the pulsed laser deposition is also a non-equilibrium process.

Sputtering [66] is a method where ions from a plasma are bombarding the surface of a target material To create the plasma a gas such as argon is introduced into a vacuum chamber. A negatively charged electrode (cathode) accelerates present electrons away. These electrons hit argon atoms causing the neutral gas to be positively charged (Ar+). These positively charged ions are than attracted by the cathode with the target material. If the kinetic energy of the ions is high enough, this leads to the removal of source material in form of particles (atoms, clusters or molecules). These neutral particles are, when getting into contact with a solid substrate, deposited onto its surface.

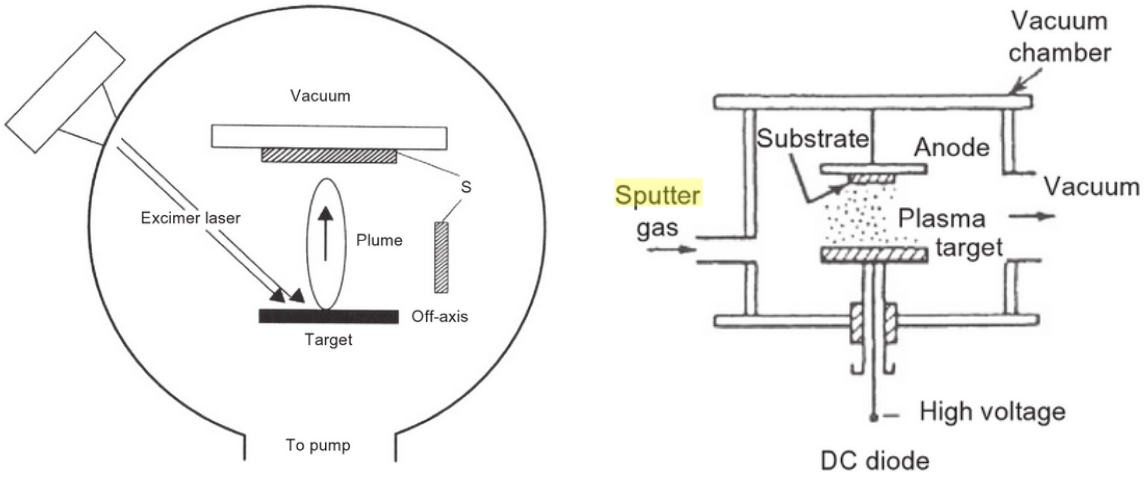

(a)PLD system [65] (b)DC sputtering system [65]

Figure 3.7: PLD and sputtering deposition systems

Besides that, also free electrons are created which maintain the plasma by forming new Ar+ ions. Depending on the target material coating the cathode, DC voltage (for conductive materials) or a RF generator (for non-conductive materials) is used. To reach high deposition rates, magnets are commonly used to trap free electrons in a magnetic field close to the target surface (magnetron sputtering). This enhances the probability of ionizing the gas, which than increases the eroding of target material significantly. From the industrial perspective in the fabrication of thin film solar cells, sputtering is a widely employed technique. Reasons for that are the high deposition rate and quality of resulting films.

A list of some physical methods used for the deposition of Mg doped ZnO are shown in Table 3.2. It displays publications from a research perspective. Because of that as substrate the standard role model sapphire was used and temperatures are very high compared to conventional deposition conditions of these methods. The goal was to investigate the properties of high quality films.

Summarizing the role of physical methods for fabricating solar cells with a ZnMgO buffer layer it can be concluded, that sputtering is the most relevant technique in this context. For example [1] fabricated solar cells with a sputtered ZnMgO buffer layer achieving an efficiency of 16.2%.

Table 3.2: Publications of physical deposition of Mg doped ZnO

Method	Mg and Zn Precursors	Temperature /Atmosphere	Mol% Mg	Substrate	Reference
MBE	oxygen plasma, metal zinc and magnesium	390°C, annealed at 710°C	till 51%	sapphire ($11\bar{2}0$)	[67]
PLD	ZnO and MgO ceramic targets	600°C, 5 * 10^{-5} Torr in pure oxygen	till 33%	sapphire (0001)	[3]
Electron beam Evaporation	Sintered (at 1500°C) MgO and ZnO powder	250°C, oxygen gase 5*10^{-2} Pa	47 - 60%	sapphire (0001)	[68]
RF magnetron sputtering	Mg_xZn_{1-x} ceramic targets	700°C, oxygen and argon, 10^{-1} bar	20%	sapphire (0001)	[24]

3.3.2 Chemical Deposition

Chemical thin film deposition involves chemical reactions during the deposition process. If a substance is vaporized and decomposed, or reacts with other gases/vapors on the substrate surface, this process is called chemical vapor deposition. An alternative deposition concept regards the synthesis of thin films from chemical solutions. These deposition methods will be discussed in more detail, since they are relevant to this thesis.

CVD is usually performed at high temperatures (1000°C) and at near atmospheric pressure. There are several types of CVD. The most common CVD technique for the fabrication of ZnO or Mg doped ZnO is metalorganic CVD (MOCVD). In MOCVD, metalorganics such as metalalkyls or alkoxides are commonly used as sources for group II and III elements. Because of the high volatility of metalorganics, deposition can be carried out at moderate temperatures (300 - 1000°C). The composed metalorganics react with hydrids (e.g. NH_3) in a hydrogen atmosphere or are oxidized in an oxygen atmosphere to form metal oxide films.

Another gas phase chemical deposition technique is atomic layer deposition (ALD) [69]. In contrary to other CVD techniques, in which reactive gases are mixed in the chamber, the highly reactive precursors in ALD react separately by surface reactions. ALD growth proceeds in cycles. In each cycle gaseous precursor molecules react with the surface till all reactive surface sites are consumed. This layer-by-layer growth leads to highly uniform films. Besides that, through variation of cycle numbers the film thickness can be controlled precisely. By alternating ALD cycles with different precursor materials (e.g. Zn or Mg), a layer-by-layer doping of films can be achieved. Compared to other CVD methods, the deposition rate for ALD is rather low. Although

because of the increasing interest in this technique especially for the fabrication of solar cells, many approaches towards large throughput ALD processing have been made recently [70].

Deposition from solution can be divided into two categories. Methods that use

- direct growth on a substrate during deposition process
- liquid coating and thermal or chemical post-treatment afterwards

Direct deposition methods include electrodeposition, chemical bath deposition or successive ionic layer adsorption and reaction (SILAR) method. Liquid coating methods include all kind of sol-gel deposition techniques and spray pyrolysis deposition. [26]

General benefits of solution-based techniques compared to vacuum deposition methods include the deposition of films at near room temperature (except spray pyrolysis) and atmospheric pressure. This leads to minimal equipment cost and the solutions can often be recycled. Other advantages in therms of device fabrication are that these methods are suitable for flexible substrates in combination with high throughput processing.

The chemical bath deposition technique is explained in section 4.1. The implemented solution chemistry is discussed in detail in section 5.1. Methods that are similar to CBD are the SILAR technique and hydrothermal depostion.

Hydrothermal deposition is carried out at temperatures higher than 100°C under high atmospheric pressure in a closed autoclave. Nucleation and film growth is similar as in the CBD process. Besides higher temperature and pressure the main difference to CBD is that volatile by-products can not be released during the deposition process in the hydrothermal system.

The SILAR [71] method is a modification of the chemical bath deposition (CBD). In CBD all precursors needed for the deposition are in one reaction vessel. In contrary to that, in the SILAR technique precursor solution are in different reaction vessels. The substrate is immersed alternating in the vessels containing cation precursor or anion precursor with an intermediate rinsing step. The substrate is rinsed with a pure solvent, mostly water. Films can be grown layer by layer through repetition of these cycles. A schematic view of the four steps in the SILAR process can be seen in Figure 3.8.

Through substrate immersion in the cation solution the ions are adsorbed onto the surface of the substrate. Adsorption of the positively charged cation happens, because substrate surfaces (such as glass or metal oxides) have an oxide layer on top of it. This layer is negatively charged in aqueous solution with pH > 2. A double layer with cations and anions is formed on the substrate. Through rinsing in the next step only the immobile double layer remains on the substrate surface. In the following step the substrate is immersed in the anion solution. This ions diffuse into the surface and react with the adsorbed cations. This is now the top layer of the film on the substrate surface. After rinsing a second time, to remove ions from the diffusion layer, the growth cycle can continue by immersion in the cation solution again. A reaction of the overall process is:

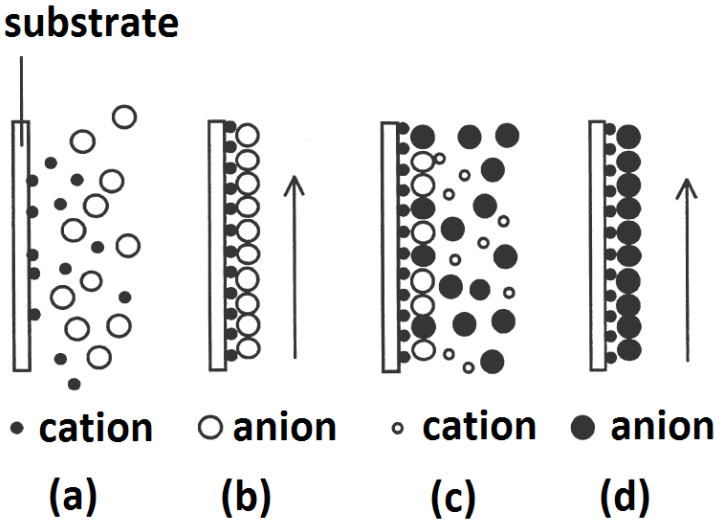

Figure 3.8: Thin film growth during one SIlAR cycle (a) cation adsorption, (b) rinsing, (c) anion reaction, (d) rinsing. Modified from [71]

$$mM^{n+}(aq) + nA^{m-}(aq) \longrightarrow M_mA_n(s) \tag{3.2}$$

The film growth is affected by many factors such as concentrations, pH, nature of counter-ions of the precursor solutions or temperature.

An advantage of SILAR compared to CBD is the facile control over film thickness, which is determined by the number of deposition cycles. Another benefit is that the system is totally closed and all chemicals can be easily recycled. The main disadvantage is the slow growth rate. Film thickness of one deposition cycle is only 1-3 Å. In addition to that, long rinsing steps are also needed.

In electrochemical deposition [72] electrons are used to reduce metal ions from aqueous or organic electrolyte solution to deposit a film. Electrons can be provided through an external power supply or an electroless deposition process. Electroless deposition uses a reducing agent as electron source. In both cases deposition takes place on the solid metal electrode. Ions from the aqueous solution react as presented by following equation:

$$M^{z+}(\text{solution}) + ze^- \longrightarrow M(\text{lattice}) \tag{3.3}$$

In Figure 3.9 (a) an electrolytic cell for the electrodeposition is demonstrated. It consists of two electrodes immersed in an aqueous electrolyte solution containing dissolved ions. To understand the deposition process the metal-solution interphase formation is from utmost importance.

Reduction always takes place at the cathode. If the potential of this electrode (= subtrate) is decreased from its eqilibrium value to lower negative potentials, the cations

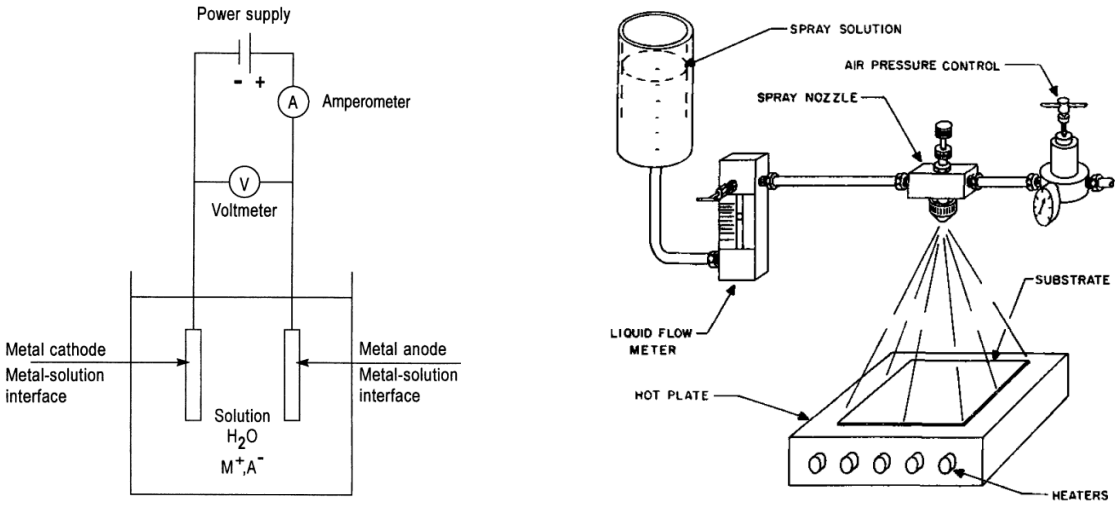

(a)Electrolytic cell for electrodeposition

(b)Spray Pyrolysis system

Figure 3.9: Electrochemical deposition and spray pyrolysis

in the electrolyte solution with the most positive redox potential (E^o) will be reduced first onto the substrate. The conditions of electrodeposition depend on the individual electrochemical reactions of the species to be reduced. This reaction can be expressed with the Nernst equation.

$$E = E^o + \frac{RT}{zF} \cdot log(\frac{[Ox]}{[Red]}) \tag{3.4}$$

This equation gives the electrode potential with respect to the standard hydrogen electrode. The electrode potential is dependent on the standard electrode potential of the species of interest (E^o), on z the number of electrons transfered during the reaction and the concentrations of reactant (Ox) and product (Red). R is the gas constant (8.314 $JK^{-1}mol^{-1}$) and F is the Faraday constant (96485 C/mol).

The main disadvantage of electrochemical deposition is that it requries a conductive substrate.

In the spray pyrolysis technique [73] a precursor solution is atomized to an aerosol. The atomizer usually works as air blast (liquid in air stream), ultrasonically (ultrasonic frequencies for short wavelengths) or electrostatically (electric field). The aerosol is then transferred onto a heated substrate. As the solution droplets reach the surface they spread into disk shaped structures and undergo thermal decomposition. An experimental setup of the system can be seen in Figure 3.9 (b). Substrate surface temperature is one of the main parameters that influences the resulting film morphology. The temperature determines for example whether the solvent evaporates during droplet flight and a dry precipitate hits the substrate, or the droplet splashes onto the substrate. Also the composition of the precursor solution in therms of type of salt, concentration and additives, influence the film deposition.

An advantage of spray pyrolysis over chemical bath deposition is that the chemical composition of the precursor solution roughly the same in the deposited film [73]. This makes this method very easy for various doping concentrations. Also upscaling this solution-based method is easier than for example sol-gel methods. A disadvantage of spray pyrolysis is the large amount of pure solvents needed.

The most advanced methods for fabricating Mg doped ZnO from solution are sol-gel based techniqes [74]. The sol-gel deposition process can by divided in three parts:

1. preparation of precursor solution
2. deposition of prepared sol onto the substrate
3. heat treatment of the gel

All three stages influence the film growth. The precursor solution contains the metal salt or alkoxide, a solvent and some additives. For metal salts, similar aspects as in the chemical bath deposition process have to be considered (see also section 5.4). As solvents, in the case of metal salts, mainly alcohols with low carbon number up to 4 are used, because they dissolve inorganic salts. Additives are added to act as chelating agents which help to complete dissolution. Through hydrolysis and polymerization a collodial system is achieved (= sol). This solution is then coated on a substrate by spin-coating or dip-coating for example. Through a pre-heat treatment around 40-500°C the solvent can be evaporated. To obtain well-crystallized films a post-heat treatment from 250 - 900°C is often employed.

Advantage of this method compared to chemical bath deposition is the precise control of precursor structure. So this method can be used to create films with certain crystal structure orientation. A disadvantage of all sol-gel based methods is that organic solvents are involved, which have to be removed properly for a high film quality. Since this involves heating to high temperature not all materials are suitable for this treatment.

Some of the described chemical deposition methods have already been used in the deposition of Mg doped ZnO films. A short overview of some examples is shown in Table 3.3.

Among these methods CVD and ALD processes are the most costly ones. On the other hand ALD is up to now the only chemical process applied for the deposition of ZnMgO buffer layers in the fabrication solar cells. For example [2] fabricated CIGS solar cells with ALD deposited ZnMgO buffer layers and achieved efficiencies of 16.2%. It has to be also mentioned that non of the above mentioned published solution based deposition of ZnMgO confirmed the Mg content by methods like ICP OES. The band gap was always determined through Tauc's plot approximation of transmittance spectra.

Table 3.3: Publications of chemical deposition of Mg doped ZnO

Method	Mg and Zn Precursors	Temperature /Atmosphere	Mg content	substrate	Ref.
MO-CVD	Diethylzinc, Biscyclopentadienylmagnesium	600°C, oxygen and nitrogen gas, 10^4 Pa	0-5% Mg	sapphire (0001) with ZnO seed layer	[75]
ALD	Diethylzinc, Cyclopentadienylmagnesium	120°C, nitrogen as carrier gas	0-20%	CIGS absorber on glass substrate	[2]
electrochemical deposition	$Zn(NO_3)_2$, $Mg(NO_3)_2$	65°C, KNO_3 as electrolyte + urotropine	0-25%	ITO-coated glass substrate	[76]
Spray Pyrolysis	$Zn(CH_3COO)_2$, $Mg(CH_3COO)_2$	400°C, air	0-21%	p-type Si substrate	[77]
Sol-gel	$Zn(CH_3COO)_2$, $MgCl_2$ + monoethanolamine	60° in 2-methoxyethanol, dried (300°C), annealed (500°C) in oxygen	0-10%	Pyrex glass substrate	[78]
sol-gel dip method	$Zn(CH_3COO)_2$ and $Mg(CH_3COO)_2$	Spin coated 0.1 - 1 mm/s, baked in air 500°C	0-25%	quartz glass, sapphire (001)	[79]

3.3.3 Solution-processed Mg doped ZnO Literature Review

Some solution-processed methods for Mg doped ZnO films are summarzized in subsection 3.3.2. In general, solution-based deposition methods have many advantages compared to vacuum methods. Deposition from the liquid phase is simple and low-cost also due to low energy requirements. Altough the material quality for vacuum-based methods is in many cases better, there are some examples which prove otherwise. A prominant example is chemical bath depositon of CdS buffer layer in the fabrication of CdTe and CIGS thin film solar cells. In the following, state-of the art for chemical bath deposited Mg doped ZnO films are discussed.

Literature on Mg doped ZnO prepared by chemical bath deposition method has to be viewed very critically. In most publications the Mg doping content in the film is very low. The solution chemistry varies a lot, as can be seen in table Table 3.4. Publication [80] reports chemical bath deposition of Mg doped ZnO from triethanolamine and hydrochloric acid up to 30 at% Mg, but does not confirm this by a composition analysis such as EDX or ICP OES. An XRD spectrum is shown, which indicates that all peaks correspond to wurtzite phase of ZnO. A SEM picture is shown which indicates

Table 3.4: Literature on chemical bath deposition of Mg doped ZnO

Mg and Zn Precursors	Additves	Synthesis Conditions	Max. mol%	Substrate	Ref., Year
Zn(CH3COO)2, MgCl2	TEA, conc. HCl	pH = neutral, 80°C, 120 min	30 %	cleaned glass slides	[80], 2008
Zn(CH3COO)2, MgCl2	NaOH, ammonia	pH = 8 +/- 0.2, 80°C, 60 min	1.5 %	cleaned glass slides	[44], 2013
Zn(NO3)2 x 6H2O, MgCl2 x 6H2O	HMTA	80°C, 2h	6 % (0.85 % confirmed)	ZnO coated FTO	[81], 2014
Zn(CH3COO)2, Mg(CH3COO)2 x 4H2O	ammonia	pH = 11-9.5, 60°C, 30 min, dried + annealed 300-500°C	48 %	Quartz substrates	[82], 2015

that the depostited film is not dense.

Reference [44] showed flower-shaped ZnMgO deposits using a chemistry of sodium hydroxide and ammonia. EDX analysis confirmed a Mg content of 1.5 at%. The authors' also claimed that with more Mg content in the film the band gap decreases from 3.3 to 3.2 eV compared to the undoped ZnO. These findings are in contrast to the widely accepted and confirmed view of a number of sources in which the band gap increases with more Mg incorporated into the ZnO lattice [62] [33] (see also chapter doping of ZnO subsection 3.2.3). Furthermore through an XRD investigation it was shown that peak intensities for ZnMgO increased compared to undoped ZnO films due to a higher crystallinity. Calculated lattice paramter a was 3.253 Åand c 5.208 Åfor undoped ZnO. Through Mg doping the lattice paramters decreased to 3.251 Åand 5.207 Å.

In paper [81] only 0.85 mol% Mg in ZnO was confirmed by EDX measurements altough the solution contained 6 mol% Mg. Up to 4 at% Mg in the solution the (002) peak increased indicating a higher crystal quality. Lattice constants a increased from 3.25 Åto 3.26 Åand c from 5.21 Åto 5.22 Åfor Mg doped ZnO nanorods. SEM images showed aligned nanorod formation. The band gap increased from 3.26 to 3.32 eV compared to undoped ZnO.

In reference [82] a novel method for chemical bath deposition of Mg doped ZnO is proposed. Special attention was paid to pH and temperature to find a condition were $Zn(OH)_2$ and $Mg(OH)_2$ can coprecipitate. Finally they obtained a mixed gel of the two hydroxides which was than annealed at 500°C. ICP and EDX confirmed Mg content up to 48 at%. The band gap calculation showed an almost linear increase in band gap with higher magnesium content. This increase in band gap can also be due to quantum-confinement effects since the SEM pictures showed no uniform film

rather than depostion of nanoparticles. Also the film density is very low with many voids due to the high annealing temperature. The XRD investigation of these samples showed some contradictory results: Even for high Mg content (up to 50 mol%) no shift in the ZnO XRD peaks could be observed, as expected from the contraction of the lattice due to the smaller Mg^{2+} radius. This suggests that the Mg may not be substitutionally incorporated in the film, at least to a large extent. In summary, more information is needed to fully understand and evaluate the results of the particular paper.

To sum it up, there is very limited literature on the chemical bath depostion of uniform ZnMgO films with a verified high Mg content incorporated. Besides that, there is no work reporting on possible mechanisms determing the chemical bath deposition of Mg doped ZnO. This thesis tries to provide insights in the chemistry and possible problems concerning this process.

3.4 Applications of $Zn_{1-x}Mg_xO$ Films

In the following some applications of $Zn_{1-x}Mg_xO$ films are discussed. The focus will lay on their use in thin film photovoltaics. Therefore some principles of thin film photovoltaic devices will be explained first.

3.4.1 Thin Film Photovoltaics

A solar cell converts UV and visible light directly into electricity through the photovoltaic effect. In comparison to the silicon cell, a thin film solar cell consists of material layers from a few nm to a few μm in thickness. The total thickness is also in the range of a few μm with the absorber and substrate materials being the thickest components. In comparision to that, the classic c-Si solar cell exhibits a thickness of around 200 μm. Therefore, for thin film technologies lower production costs per surface area are expected.

The photovoltaic energy conversion can be broken down in four steps:

1. Absorption of photons in the material
2. Creation of charge carriers (electrons and holes)
3. Separation of oppositely charged carrier before they recombine
4. Collection of charge carriers in an external circuit to create electric currrent

A perfect energy conversion cycle would look like Figure 3.10. Due to several types of losses the real conversion cycle looks more like Figure 3.11. If the energy of photons is lower than the band gap of the absorber semiconductor, electrons are not excited. Therefore no electrical energy can be tranferred to the external circuit. Some photons may also be reflected by the surface before they can be absorbed. Other losses can come from thermalization or recombination.

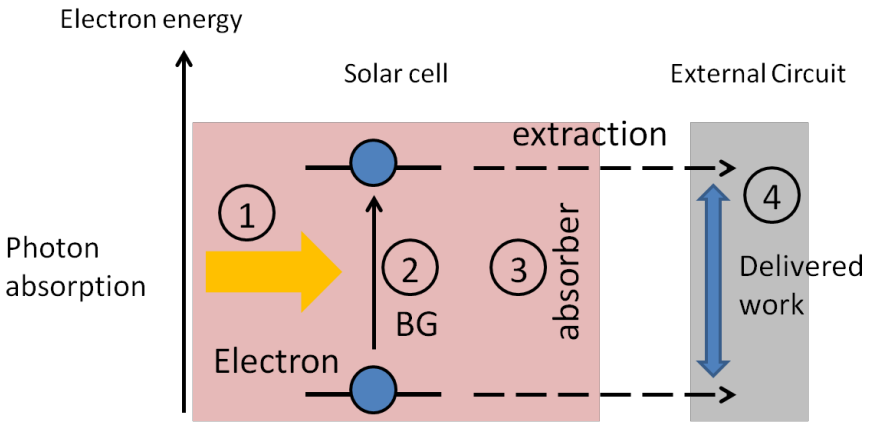

Figure 3.10: Ideal energy conversion cycle for solar cells

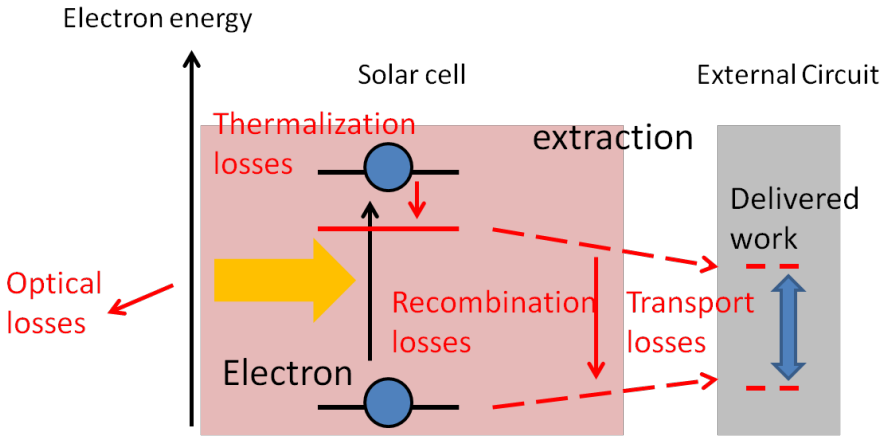

Figure 3.11: Realistic energy conversion cycle for solar cells

To garantee a high conversion efficiency appropriate materials have to be chosen. Therefore a thin film solar cell consists of several thin layers each of them achieving specific goals. A schematic structure of a typical thin film solar cell can be seen in Figure 3.12.

A transparent conducting oxide (TCO) collects the photogenerated electrons, while allowing through its high transparency light to enter the solar absorber. An often used TCO is indium doped tin oxide (ITO), but certain absorber/buffer materials require different properties as provided by alternatives like aluminium doped ZnO (AZO). The buffer layer is needed to create a junction with the p-type absorber layer and drive carriers to the electrode. In the absorber layer of the solar cell, photons with an energy higher than the band gap of the semiconductor are absorbed. Electrons are therefore excited to a higher state of energy, leaving a positively charged holes behind. Thus free charge carriers are created in this layer. Because of the internal electric field arising from the p-n junction charge carriers are separated. The p-n junction is the essential part of a solar cell. Therefore it is explained here shortly.

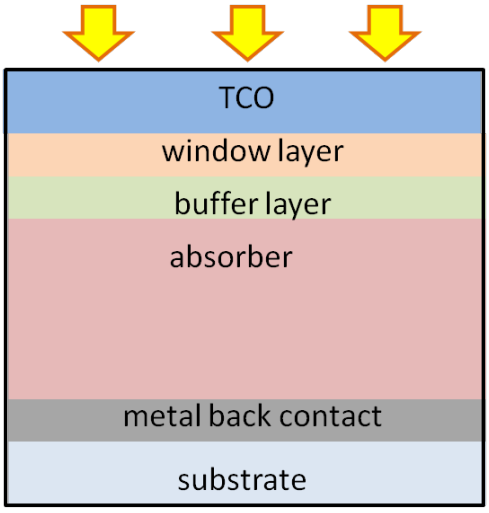

Figure 3.12: Schematic structure of a thin film solar cell

A p-n heterojunction as often used in thin film photovoltaics consists of p-type absorber material and a n-type buffer layer. By combining this two layers electrons from the n-type material diffuse to the p-type region leaving positively charged holes behind. This charge transfer creates an electric field as seen in Figure 3.13.

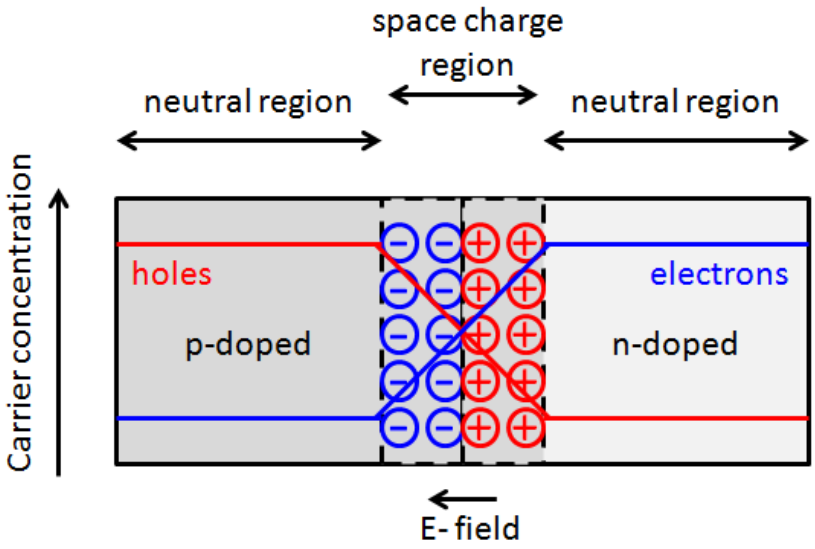

Figure 3.13: Principle of a p-n junction

This created electric field is the driving force for the charge carrier separation. When electrons are excited in this space charge region through absorption of photons, the charge carriers (electrons and holes) are separated as seen in Figure 3.14. The resulting band bending causes generated minority carriers to be drawn in opposite directions. If the internal electric field is too weak charge carriers will recombine. To avoid these losses in energy a rather wide depletion zone in combination with a strong electric

field is necessary[83]. To collect the generated holes a highly conductive thin metal layer is also needed. As substrate for the deposition of all subsequent layers often glass or a flexible polymer is used.

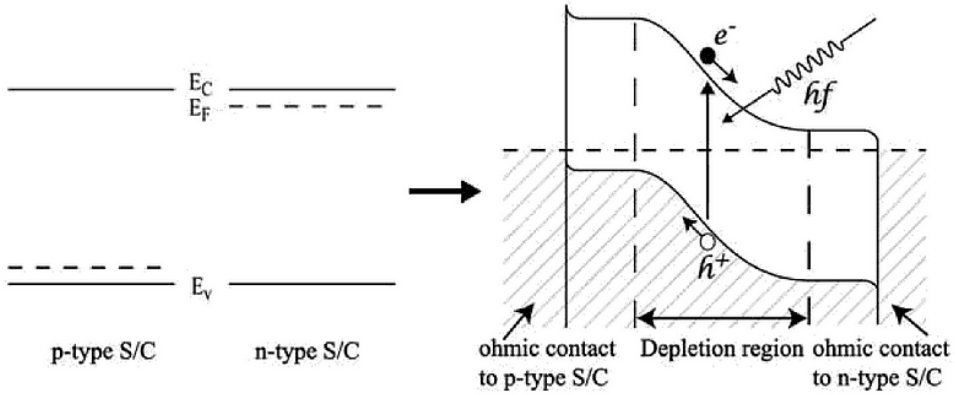

Figure 3.14: Energy diagram and principle of a p-n junction [83]

As discussed in section 3.2 ZnO is unintentionally always a n-type material. Because of that, ZnO and n-doped analogues are suitable candidates as buffer layers for the p-n junction.

An ideal n-buffer layer should be aligned according to the conduction band maximum of the p-absorber. Difference in CBM are expressed as band offset. There are three possible cases (see also Figure 3.15). If the conduction band of the n-buffer layer is below the absorber a "cliff" is formed. This cliff acts as barrier against injected electrons and recombination between majority carriers occurs. Because of this the open-circuit voltage decreases causing a lower cell efficiency. If the conduction band of the n-buffer is above the absorber a barrier for electron transport (called "spike") is formed. This causes a decrease in short-circuit current, hence decreasing the cell efficiency. The optimum for the band-offset lies in betwen these two. The ideal band-offset varies with absorber/buffer-layer combination. [84]

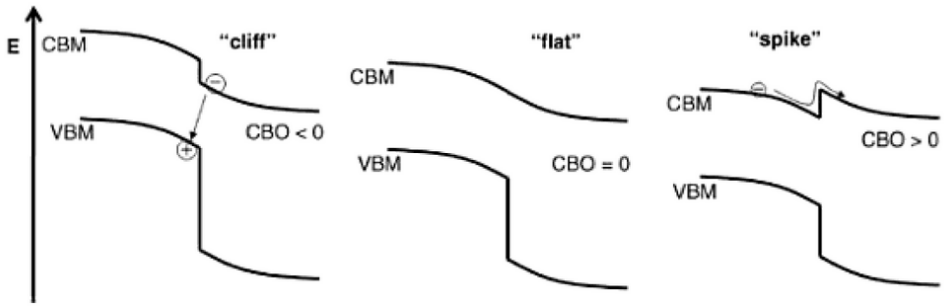

Figure 3.15: Possible conduction band alignments for pn-heterojunction [84]

Undoped ZnO has a band gap of around 3.37 eV and a rather large conduction band offset compared to the typical thin film photovoltaic absorbers like p-CIGS or p-CZTS.

As discussed in previous chapters the bandgap of Mg doped ZnO can be tuned between 3.37 to 6.7 eV. Therefore this makes $Mg_xZn_{1-x}O$ films a promising candidate as buffer layer in thin film photovoltaic devices. Band gap engineering makes the conduction band offset between buffer layer and absorber material controllable through variation of the conduction band maximum.

So far CdS is the standard buffer layer in CIGS and CZTS thin film solar cells. CdS has an optimum band offset with these absorbers as can be seen in Figure 3.16.

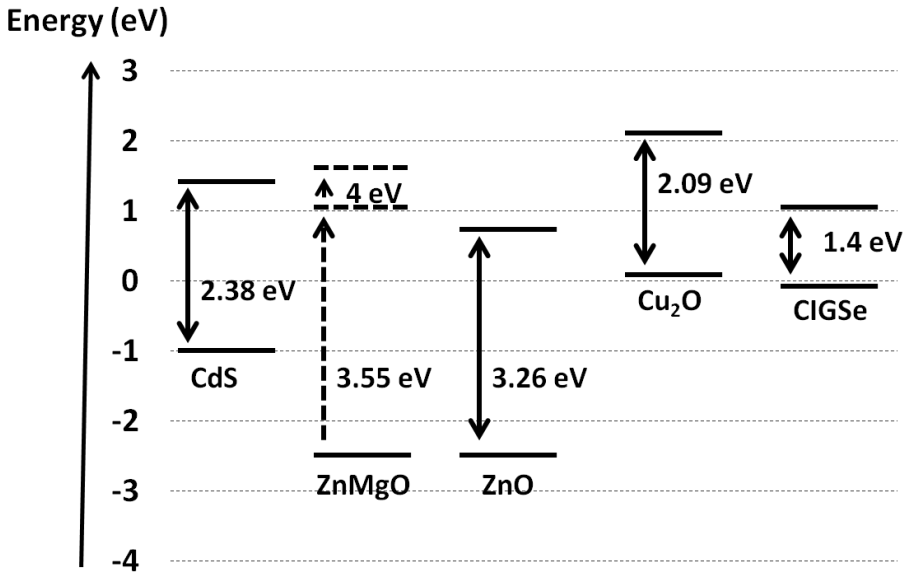

Figure 3.16: Band diagrams for buffer and absorber materials (data from [85], [84])

Because of the enviromental impact arising from the deposition process of the toxic CdS, replacing this material with an enviromental friendly and abundant alternative is from utmost interest. Mg doped ZnO consists of high abundant elements without any harm to human health and the enviroment. Another reason to replace CdS with a high band gap material is the low band bap of CdS (2.4 eV). Due to absorption in the CdS layer a current loss can not be avoided. A larger band gap material would reduce this loss and therfore enhance the cell efficiency. Another not implicitly beneficial effect of ZnMgO layer is the light-soaking behaviour. It was shown that the fill factor of cells with CIGS absorber and ZnMgO buffer layer increased with light soaking [86]. Figure 3.16 shows the band alignment of ZnMgO and ZnO with suitable absorber candidates.

An example where a ZnS/ZnMgO buffer layer combination was sucessfully used in fabricated CIGS solar cells is [20]. In this publication $Mg_xZn_{1-x}O$ films were deposited by RF magnetron sputtering from ceramic targets. The efficiences for small laboratory cells was 18%, while cell mini-modules (10 x 10cm^2) reached an efficiency of 15.2%. In therms of chemical $Mg_xZn_{1-x}O$ film deposition methods ALD deposited $Mg_xZn_{1-x}O$ layers were integrated in CIGS solar cells by [2]. The efficiencies for the devices (8 cells

of 0.5cm^2) where 16%. Solution-based chemical deposition methods for $Mg_xZn_{1-x}O$ buffer layers where so far never used in thin film solar cell fabrication.

3.4.2 Other Applications

ZnO and $Mg_xZn_{1-x}O$ are attractive candidates for the fabrication of UV (ultraviolet) photodetectors. Up to now Si photodiodes dominate the market because of the low price and well-developed technology. Since the band gap of Si is only 1.1 eV, external filters are needed to block the long-wavenlength response to achieve UV detection. This causes a low photoresponsivity due to reflection of these filters. Because of these issues, the band gap tunable $Mg_xZn_{1-x}O$ is considered as a potential replacement [87]. Since the aborption edge of $Mg_xZn_{1-x}O$ is abrupt and can be tuned to the deep-UV region, this material can also be used for deep UV detection. A metal-semiconductor-metal (MSM) device with a peak responsivity at 270 nm was fabricated by [88].

Because $Mg_xZn_{1-x}O$ is a non-toxic material, biosensing is also a possible area for applications. An ion-sensitive ZnO/ZnMgO heterojunction field-effect transistor (HFET) with an amine-modified gate electrode was for example developed by [89]. Thin-film transistors (TFT) can also be fabricated with ZnMgO layers. TFTs are used in many applications for example in liquid crystal displays (LCD) or organic light-emitting displays (OLEDs). The wide band gap cubic-ZnMgO can be used as gate insulator, while the hexagonal-ZnMgO is used as channel [90]. Since these two materials can be grown in the same deposition chamber, contamination problems are not an issue, compared to TFT devices with different materials for gate and channel.

It is not facile to fabricate a laser with a predetermined wavelength. Band gap engineering opens the way to such applications. Stimulated emission from ZnMgO alloy nanowires at room temperature was reported by [91]. This behaviour can be used for light-emitting device applications

In general ZnMgO films have a huge potential in various optoelectronic applications. Their attraction mainly rises from the largely tunable band gap. Besides that, ZnMgO is an enviromental friendly, abundant and low-cost material. One of the main challenges for large scale implementation of such devices and cells is the development of a cost-efficient and high throughput deposition technique that produces films of adequate quality.

4 Methods

4.1 Chemical Bath Deposition

The first chemical bath deposition was performed in 1933 depositing a thin film of PbS [92]. Chemical bath deposition got more attention when CdS deposited films in CdTe and CIGS solar cells showed superiour cell performance. The CBD technique refers to the deposition of a film onto a substrate through a chemical reaction in a solution. Details about the solution chemistry are discussed later on. Prerequisite for a material to be deposited are, that the formed compound precipitates in the solution and is therefore insoluble. Compounds that have been deposited with CBD include oxides, sulphides, selenides, tellurides and halides.

In practice CBD is a low-cost deposition method because it does not require much equipment. Basically a solution container and a hot plate/stirrer for controlling the temperature as well as stirring process are needed. To immerse the substrate in the solution a substrate holder is necessary. Besides that, a pH probe is useful to control the highly pH-dependent process. As material precursors various metal salts are used. Important process paramters are temperature, pH, concentration of salts, additional agents, deposition time and stirring rate.

In CBD compared to other solution-based methods substrates do not have to be conductive and can be of various natures. Because of its simplicity CBD can be integrated in a roll-to-roll device fabrication process. CBD grown films are often compact and homogeneous. A drawback of the method is the generated waste solution. The solution can only be re-used a numbered amount of time, because it depletes over time. Therefore, when integrated in device fabrication, the solution has to be changed regularly.

4.2 Characterization of Thin Films

The optimization of thin film deposition processes demands a fundamental knowledge of the produced material. Therefore analytical characterization is very important to tailor certain properties of the deposited film. Depending on the material requirements various characterization tools are available. For thin film photovoltaics morphology and transmittance of the material are some important properties. Therefore the scanning electron microscope (SEM) and x-ray diffraction (XRD) were used to

give insights in the morphology of the produced films. Fourier transform infrared-spectroscopy (FTIR) was used to show transmittance and calculate the band gap of the material. Since the ZnO films were doped with Mg also the elemental composition of the film was important. Therefore inductively coupled plasma atomic emission spectroscopy (ICP-OES) was used to determine the amount of Mg in ZnO.

4.2.1 SEM

The scanning electron microsope is one of the most useful tools to determine the morphology and thickness of thin films. It can magnify samples 100,000x (or a few nm), compared to a conventional light microscope which has a maximum magnification of 2000x.

A basic SEM device consists of an electron beam source, electromagnetic lenses which focus the beam onto the specimen, and detectors (as seen in Figure 4.1). To avoid scattering of electrons by gas atoms, a vacuum enviroment is needed. As electron gun a tungsten filament is heated which causes thermal emission of electrons. Through applying a negative bias on the so called Wehnelt cylinder the electrons are focussed forming a beam.

To display the surface morphology a focused electron beam is rastered over the surface. As the electrons penetrate the sample surface, many interactions happen. For example electrons from the sample can be ejected by the electron beam through inelastic scattering. This generated electrons are called secondary electrons (SE). They give valuable topographical information because most of them are produced within the first few nm of the surface. It can be distinguished between slow and fast secondary electrons. Most SE detectors collect slow low energy SE ejected from the conduction or valence band. The incident electron beam can also scatter elastically with the specimen atoms producing back-scattered electrons. Heavy elements backscatter electrons more strongly so that the chemical composition can give a constrast in the SEM image. Therefore detecting backscattered electrons give topographical and elemental information. The electron beam can also eject inner shell electrons from the specimen producing characteristic x-rays. Analysis of x-ray signals can be used to display elemental information.

Within this thesis SEM was used to display the surface morphology of the deposited films by detection mainly secondary electrons. It was important to see that a dense film was produced and to determine differences in the crystal structure. By breaking the samples and investigating the cross sections, the film thickness was determined. Further, these images showed how film growth proceeded.

The used device was a Zeiss Supra 40 SEM.

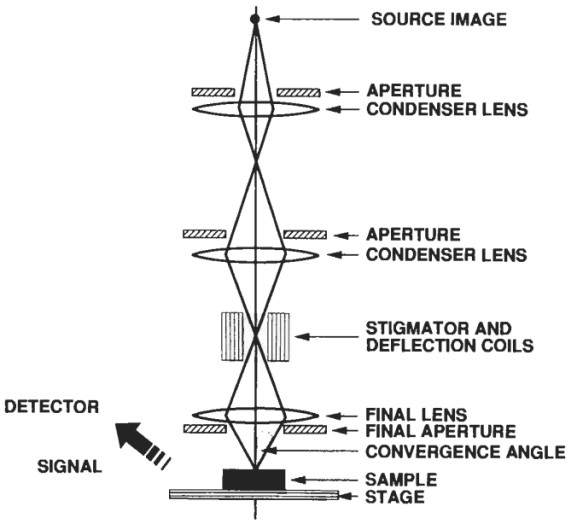

Figure 4.1: Scheme of a scanning electron microscope [93]

4.2.2 FTIR

In the fourier transform infrared spectroscopy (FTIR) the absorption of light at each wavelength is measured in general. Instead of using a monochromatic light beam (a certain wavelength), the FTIR uses a Michelson interferometer, which allows to detect all frequency contributions simultaneously. An FTIR consists of a light source, interferometer and a detector. Depending on the wavelength range different light sources are used. The core of a FTIR is the Michelson interferometer. The concept is displayed in Figure 4.2.

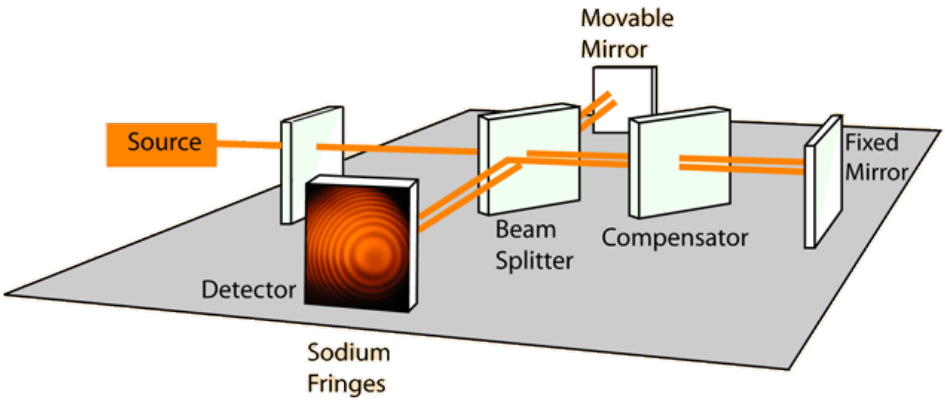

Figure 4.2: Scheme of a Michelson interferometer [94]

Incident light is splitted into two beams, one of them is directed to a stationary mirror, the other one to a movable mirror. The beams are reflected by the mirrors and recombined. By moving one of the mirrors the paths of the two beams become different. This results in constructive or destructive interference depending on the difference in

pathlengh the light travelled. The minima and maxima in dependence of the mirror positions lead to an interferogram of the incident light. In an interferogram intensity is a function of time. A fourier-transformation translates the interferogram into a spectrum, with intensity as a function of frequency.

The FTIR is often used in the transmission mode. If the sample is very thin incident light can transmit through. Depending on the chemical composition of the sample, light of certain wavelengths is absorbed. The intensity of light after absorption is measured as a function of wavelength. The attenuation of incident light related to the material, through which the light travels, can be described with Lambert-Beer's law. The relationship of the absorbance and the two intensities before and after passing the sample is given by:

$$A = log(\frac{I_0}{I}) \quad and \quad T = \frac{I}{I_0} \tag{4.1}$$

Another possibility would be to measure the reflection of a sample. In thin film characterization this is often used to determine the carrier concentration. This is important for example in tranparent conducting electrodes, in which conductivty is one of the main criteria.

Within this thesis the FTIR was mainly used to determine the film transmittance in the UV/Visible region. With Tauc's model the optical band gap of a semiconductor material can be extracted from the transmittance spectrum. The absorption coefficient α near the band edge shows an exponential dependence over a limited range of photon energies hν. The relationship is given with:

$$\alpha h\nu = \beta(h\nu - E_g)^n \tag{4.2}$$

α is the absorption coefficient, β is defined as the band edge paramter, hν is the photon energy (with h = Planck constant and ν is the frequency) and E_g is the optical band gap. n characterizes the transition process of the semiconductor. For direct transitions, as in ZnO, n = $\frac{1}{2}$. The intercept of the linear extrapolation of the absorption coefficient against the photon energy with the abscissa axis is defined as the Tauc optical band gap. [95]

The used device was Bruker Vertex 70 FTIR.

4.2.3 XRD

X-ray diffraction is a important tool to determine the crystal structure of a material. X-rays are electromagnetic radiation with wavelengths around 10^{-10}m. Because the wavelength is in the same order of magnitude as the spacing between d planes of a crystal, x-rays produce significant diffraction.

X-rays are typically generated by accelerating electrons onto a metal anode. The electrons are decelerated on the anode and release radiation with a continous range of wavelengths, which is called Bremsstrahlung. Besides that, there are also spectral lines released. Spectral lines are generated when electrons remove inner shell electrons from the target material. Electrons of higher energy drop into the vacancies. While doing so, they emit their exess energy as x-ray photons. Depending on the energy transition of the electrons these radiations are labelled K_α or K_β lines (electron falls into K shell) for example. When these characteristic x-rays are directed onto a crystalline material the crystal lattice atoms cause the incident beam to diffract into specific directions. The energy of the diffracted beam depends on the diffraction angle 2Θ. 2Θ is the angle between incident and diffracted x-rays. If there is constructive interference from x-rays through scattering by the crystal planes, a diffraction peak is observed (see also Figure 4.3). The condition of such a constructive interference is given by the Bragg's law:

$$n\lambda = 2dsin(\Theta) \tag{4.3}$$

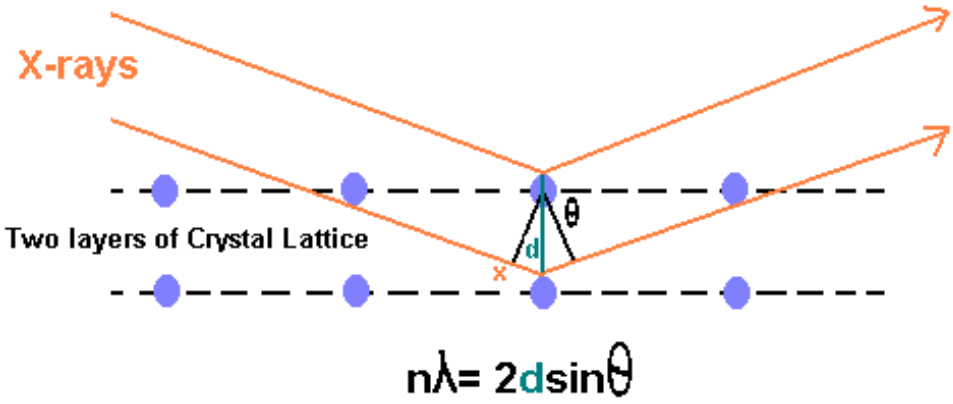

Figure 4.3: Bragg's law for XRD [96]

Where n is any integer, λ is the beam wavelength and d is the spacing between crystal planes. The diffracted intensities are usually measured as a function of 2Θ. Through scanning with different diffraction angles different reflections can be measured. Intensities of every spot are recorded at every crystal orientation. The resulting diffraction pattern is characteristic for a crystalline structure. The diffraction peaks are compared with a database containing all kinds of crystal structures, to verify the crystal structure. Besides that XRD can also be used to determine strain and crystallite size. If for example dopants are incorporated into a crystal lattice this often causes an increase or decrease in strain because of the different ionic radius. Theses shifts the diffraction peak positions depending on the size of the incorporated atoms to higher or lower diffraction angles. If the two mixed components have the same crystal structure their composition can be estimated using Vegard's law. Diffraction peaks can also give information about the size of crystallites. The broadening of a peak can be related to

the size of particles with the Scherrer equation. But this equation is only applicable to nano-scale particles not larger than 10 nm.

Within these thesis XRD was used to verify that the films were wurtzite ZnO and MgO was not present. Also the dominant crystal orientations of the deposited films were very important, since these give insights in the deposition mechanism. Through face-selective adsorption during deposition, certain crystal faces can be stabilized. Besides that special attention was paid to the peak positions to see if Mg was incorporated.

The used device was a XPert MPD.

4.2.4 ICP-OES

The inductively coupled plasma atomic emission spectroscopy (ICP OES) is one of the most important analytical instruments in the detection of trace elements. In this type of optical emission spectroscopy a inductively coupled plasma is used to generate excited atoms and ions of the sample. When these excited atoms return to the low-energy position they emit radiation with a characteristic wavelength. The wavelength is used to determine the type of element, while the intensity determines its concentration.

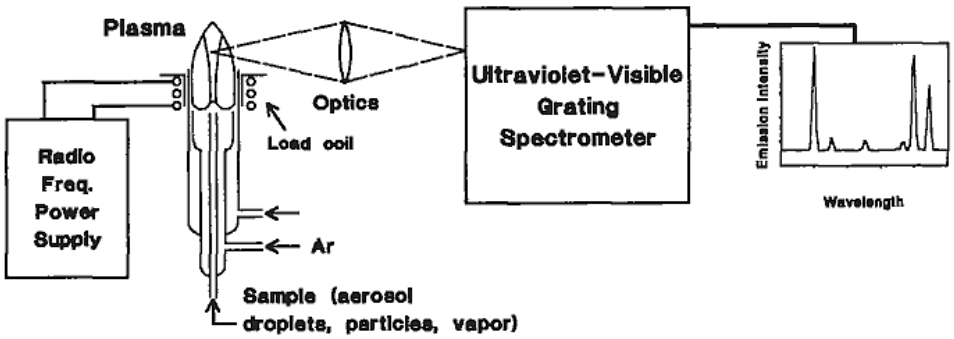

Figure 4.4: Instrumentation for ICP OES [93]

A general scheme of a ICP OES device can be seen in Figure 4.4. It consists of a sample introduction system, a plasma torch, a power supply for the plasma and an optical measurement system. Plasma is a high temperature partially ionized gas. It is generated through oscillating magnetic fields from a radiofrequency generator. Argon is most commonly used as plasma gas. The sample is introduced in form of small droplets. Through energy transfer via collisions from the plasma to the sample, bonds are broken and the resulting atoms and ions are excited. Through recording the UV and visible region of the spectrum, the specific emission line for each element can be detected. To quantify the amount of an element through the peak intensitiy, calibration curves with a standard series of the elements to be determined, are needed. [93]

The ICP OES can only analyze samples that can be introduced into the plasma as liquid or aerosol. For analyzing the elemental composition of a thin film deposited onto

a substrate, the film has to be dissolved in an analyte solution. Therefore the analyt should not react with elements present in the film. After calibration with standards, containing a similar composition than the sample solution, the amount of elements present in the solution is given as a concentration (e.g. mg/mL). ICP OES if often used to determine doping concentrations in thin film depositions. To decide whether the doping atoms are only interstitially in the lattice or substitionally incorporated, other characterization methods such as XRD have to be used for confirmation.

ICP OES was used within this thesis to determine the doping amount of Mg in ZnO. Therefore the intensities of Mg and Zn were measured simultaneously. The device was calibrated with standard series of Mg and Zn as well as a reference standard. The used device was an Optima 5300 DV. Liquid samples were prepared for the analysis. The thin film was dissolved in a solution containing 1 ml of 5 M ultrapure HNO_3 and 4 ml ultrapure water. To ensure the whole film is etched from the glass substrate, samples were put in an ultrasonic bath for 20 minutes at room temperature. Afterwards the glass slides were removed from the sample solutions. Besides the non-diluted solution samples, also a series of 1:10 diluted solutions was measured to ensure the concentrations of the samples are in the calibration standard series range. The error of the measurement was defined as the deviation of the reference standard from the target value. This is for Zn +/- 3% and for Mg +/- 2%. The error for the indicated mol% Mg in the films is therefore in average +/- 0.045 mol% off.

5 Solution Chemistry

5.1 Basic Principles of Chemical Bath Deposition

The chemical bath deposition uses a controlled chemical reaction to deposit a thin film on a immersed solid substrate.

For the understanding of the solution chemistry in the chemical bath deposition some fundamental basics have to be known:

- Hydrolysis of Metal Ions
- Solubility Product
- Complexation in aqueous solution

If a metal salt is dissolved in water the ions are removed from the solid salt lattice and are becoming a hydrated species in the solution to a greater or lesser extent:

$$Mx+ + nH_2O \rightleftharpoons M(H_2O)_n^{x+}$$

The negative oxygen from the water molecule is attracted to the positively charged cation. This results in a weakening of the –OH bond of the water molecule through electron transfer to the oxygen atom. Finally this breaks the bond resulting in the formation of the soluble metal hydroxy complex and generating an acidic solution:

$$M(H_2=)_n^{x+} + H_2O \rightleftharpoons M(H_2O)_{n\text{-}1}OH^{(x-1)+} + H_3O^+$$

E.g. $Zn(NO_3)_2$ hydrolysis in aqueous solution:

$$[Zn(H_2O)_6]^{2+} + H_2O \rightleftharpoons [Zn(H_2O)_5OH]^+ + H_3O^+ \tag{5.1}$$

$$[Zn(H_2O)_5OH]^+ + H_2O \rightleftharpoons Zn(OH)_2 + H_3O^+ + 4H_2O \tag{5.2}$$

The solubility product represents the level a salt dissolves in a solution. This behavior is defined by the solubility product constant K_{sp} which is the product of dissolved ions.

$$K_{sp} = [M^{n+}]^a [X^{m-}]^b \tag{5.3}$$

E.g.: $K_{sp} = [Zn^{2+}][O^{2-}]$

This means the higher the K_{sp} value is, the more soluble is a salt. The solubility product gives the concentration of ions before precipitation occurs. Since the deposition of oxides from solution proceeds via the metal hydroxide, the concentration of OH- ions, hence the pH, is important. The OH- concentration increases with higher temperature due to the temperature-dependence of the ionization constant of water. Therefore, temperature is very important for the precipitation and deposition of ZnO.

Another concept crucial for the understanding of solution chemistry is complexation. Complexing agents are added to the solution to prevent the metal hydroxide from precipitating. This complexant helps to buffer the concentration of free metal ions below the precipitation point causing supersaturation of the solution. For example if ammonia is added to a solution of Zn^{2+} ions, no precipitation of $Zn(OH)_2$ occurs. Instead, the following complexation happens:

$$Zn^{2+} + 4NH_3 \rightleftharpoons [Zn(NH_3)_4]^{2+} \tag{5.4}$$

This equilibrium is characterized by the complex stability constant:

$$K_s = \frac{[Zn(NH_3)_4]^{2+}}{[Zn^{2+}] \cdot [NH_3]^4} \tag{5.5}$$

Literature data is mostly available as $\beta = -logK_s$. From this equilibrium the amount of ammonia required to prevent precipitation can be calculated. At higher temperature the pH decreases and therefore, the ammonium hydroxide equilibrium shifts to the ammonia (see also Equation 5.9). In addition to that, the complex stability constant decreases with increasing temperature. This can be explained with the Le Chatelier principle, which says if there is an increase in temperature the reaction will react in the opposite direction as in absorbing heat, which causes the dissociation of the complex. The relation between temperature and equilibrium constant is given by the Van't Hoff approximation.

$$ln(K) = \frac{-\Delta H^{f_0}}{RT} \tag{5.6}$$

ΔH is the standard enthalpy change in the complex formation process and R (8.314 $JK^{-1}mol^{-1}$) is the gas constant. If the solution contains more than one cation, complexation can be used to offset the difference in the solubility product between the metal (hydr)oxides to co-precipitate the elements.

E.g.from [97]:

$$Zn(OH)_2 \text{ (s): } K_{sp} = 10^{-16.5}$$
$$Mg(OH)_2 \text{ (s): } K_{sp} = 10^{-11.25}$$

According to the solubility product of these metal hydroxides, $Zn(OH)_2$ and to a larger extent ZnO, will predominately precipitate. Incorporation of Mg^{2+} ions in the ZnO lattice can happen only by adsorption. To increase the amount of magnesium in the deposited film, a ligand that forms a stronger complex with zinc than magnesium (e.g. ammonia) is needed.

5.2 Nucleation and Growth

Film formation can be divided into two steps: nucleation and growth. For the formation of a solid material from solution, the bath has to be thermodynamically unstable, which means supersaturated. In general, there are two nucleation reactions leading to the formation of a solid metal oxide competing with each other:

- Homogeneous precipitation (within the bulk of the solution)
- Heterogeneous precipitation (at the surface of the substrate)

The key to film deposition is to control the rate of metal oxide formation to form slowly a film on the substrate or diffuse there and adsorb onto the surface, rather than precipitate in the solution. Energetically heterogenous nucleation is preferred over the homogenous one. This is because the energy required to form an interface between the (clustered) ions and the solid substrate is much lower than forming stable particles with high surface areas [98].

Basically there are two distinct models which describe film growth:

- Ion-by-Ion Mechanism
- Cluster-by-Cluster Mechanism

In practice both processes are present at the same time. The extent of homogenous and heterogeneous nucleation describes which mechanism is dominant. The degree of supersaturation in the solution and the catalytic activity favors one process over the other [99].

The ion-by-ion mechanism is generally characterized by following ionic reaction:

$$M^{n+} + X^{m-} => M_m X_n \tag{5.7}$$

An adsorbed solid $M_m X_n$ is formed on the surface, based on the principle that the solubility product is exceeded. If K_{sp} is not exceeded, the small nuclei redissolve before reaching a stable size. Once nucleation on the substrate begun, deposition occurs more easily on the surface, promoting further growth. Practically there are several ionic reactions involved in this process making the chemical bath deposition process complicated. One method to favor film formation on the substrate is deposting

a seed layer prior to the chemical bath deposition. This process is discussed in detail in section 5.3.

In the cluster-by-cluster mechansim, agglomerates of homogenous precipitated particles are absorbed onto the surface to form a film. This solid film consists mostly of metal hydroxides in alkaline solutions. That is the reason why this mechansim is often called hydroxide mechansim. The initial step for film growth is the adsorption of the hydroxide on the substrate. This hydroxide can then be converted to the oxide via dehydration. The amount of homogenous precipitate in the solution can be decreased by choosing appropriate process parameters. [98]. Both growth mechanisms are schematically illustrated in Figure 5.1.

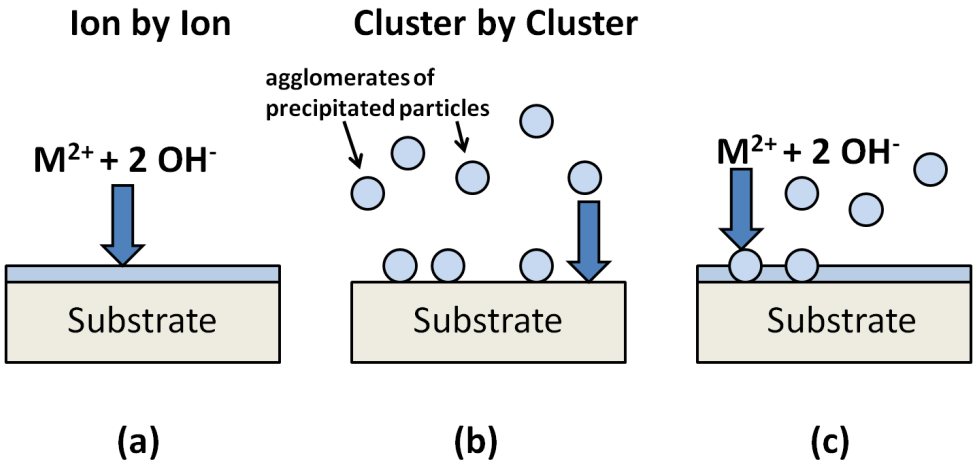

Figure 5.1: Various growth mechanisms (a) Ion-by-Ion growth, (b) Cluster-by-Cluster growth, (c) Mixed growth

5.3 ZnO Growth on Seeded Glass Substrates

Almost every ZnO chemical bath recipe uses an initial seed layer as undercoat prior the main film deposition process (frequently called two step deposition). In contrary to that, no seeding is needed for ZnS or InS_x. Often glass slides are used as substrates. Attempts to deposit films directly there, led to non reproducible or no growth at all. An unconventional method depositing films without a seed layer was proposed by [100]. They developed a reproducible deposition method with Fe contaminants acting as nucleation centers for ZnO growth.

There are various seeding methods which include sol-gel methods (e.g. spin coating) such as [101] and sputtering. In this context only sol-gel methods are discussed because they are often performed at lower temperatures and do not need vacuum conditions, compared to other approaches.

The presence of a thin seed layer is crucial to induce nucleation and formation of ZnO films. A seed layer of ZnO can, due to the high affinity of wurtzite ZnO nuclei for

the surface, promote heterogenous nucleation. An investigation that the density of nanorod arrays is proportional to the number of nucleation sites on the surface was described by [102].

Structural properties of the growing ZnO film are strongly influenced by the morphology of the seed layer. Especially the orientation of the film is altered by the thickness and preparation conditions of the seed layer. The preparation conditions include temperature and concentration of precursor solutions. [103]

It is also possible to deposit ZnO on Si wafer with a seed layer undercoat as shown by [104]. In this case the surface was activated by spin casting of ZnO nanocrystals with a diameter of 5-10 nm. Because heat treatment is not necessary for all seeding procedures, also polymer sheets can used as substrates [102]. These two examples show that seeding provides a possibility for growth of ZnO on various substrates with new applications in mind.

The used seed layer recipe was adapted from [105]. The exact recipe is described in section 5.5. This seeding method was chosen because it is a simple and fast low temperature approach using the same reactants as in the chemical bath solution. So impurities can not effect the further ZnO growth. Especially also residues from any other solvents can be avoided.

5.4 Formulation of Chemical Bath Solutions

The typically alkaline solution contains the metal ion, a base as a source of hydroxide ions and a complexing agent to control the hydrolysis of the metal ion. Besides that, capping agents are used to design specific film morphologies. In the following, the different possibilites for solution ingredients are presented and their differences discussed. For each species a chemical was chosen. This led to the final recipe of the experimental chemical bath deposition within this thesis (see section 5.5).

5.4.1 Zinc

As zinc source, various salts have been reported. As described in section 5.1 metal salts dissociate in water. The degree of dissociation depends on the Brönsted acid strength of the anion and can be ordered as follows [106]:

$$ClO_4^- > Cl^- > NO_3^- > COO^- > CN^- > CO_3^{2-}$$

Anions play also a role as additional complexing agents forming zinc-ligand complexes. The complex stability is different for the various counter-anions. This causes small differences in speciation calculations for the supersaturation of zinc hydroxide. Among commonly used anions, nitrate is not forming any stable complexes, while sulfate anions form the most stable ones. The effect of this complex stability constants

of various anions on growth rate, film composition, optical transmittance and band gap of deposited ZnS films was investigated by [107].

The influence of different counter-anions such as nitrate, chloride, perchlorate, acetate and sulfate on the film morphology was investigated by O'Brien et. al. [108]. Some of these species act as nucleation and growth promoter/inhibitors. If the growth is hindered in certain directions, either by electrostatic attraction or specific adsorption of the counter-ions on the charged surface of ZnO, the crystal shape is altered.

Another aspect of different anions is their volatility. For example zinc carboxylates are very volatile, compared to nitrate or chloride salts. Li et. al. showed that ZnO deposition is only possible with zinc carboxylates by releasing volatile by-products [36]. This can be done either by a pressure release during hydrothermal ZnO growth, or by an open bath as used in the chemical bath deposition.

Taking into account the high dissociation in aqueous solution and the complexation behaviour, nitrate was chosen as counter-anion in these experiments. There is also esample literature using nitrates in the chemical bath deposition of ZnO, which can also be useful for comparision.

Used reagent

Zinc nitrate hexahydrate $Zn(NO_3)_2 \cdot 6H_2O$

5.4.2 Magnesium

As reviewed in section subsection 3.3.3 there is not much literature on performing chemical bath deposition with magnesium. In the available publications magnesium chloride or acetate are mainly used.

Similar to zinc in the previous section, magnesium salts dissociate in water forming aqua-complexes. In comparison to zinc, magnesium always forms complexes of lower stability. Altough zinc and magnesium ions have the same charge and almost same ionic radii, the electronegativity of zinc is higher. This is due to the fact that zinc contains more electrons as well as electrons in d-orbitals. d-orbitals behave different in shielding from the nuclear charge compared to the p or s-orbitals in magensium. Certain factors influence the stability of metal complexes. With increasing electronegativity of the metal ion also the complex stability increases [109].

Because of the low complex stabilty, anions as additional complexing agents do not play a role in the case of magnesium. Counter-anions can still influence the morphology of the film.

Since zinc nitrate was used in the experiments, also for the magnesium the nitrate salt was added to avoid additional effects on the morphology from another counter-anion species.

Used reagent

Magnesium nitrate hexahydrate
$Mg(NO_3)_2 \cdot 6H_2O$

5.4.3 Hydroxide

Hydroxide ions are essential in the formation of the solid $Zn(OH)_2$, which coverts to ZnO at temperatures above 60°C [110] (see also discussion in subsection 5.6.1). As discussed before, zinc, as well as magnesium, are forming a hexaaqua-complex with water, when dissolved in an aqueous solution. Adding hydroxide ions to the solution leads to a deprotonization of the complexes, resulting in precipitates of the corresponding metal hydroxides. Since zinc has an amphoteric behaviour, an excess in hydroxide ions leads to a soluble anionic complex (see Equation 5.8).

$$[Zn(H_2O)_6]^{2+}(aq) \xrightarrow{OH^-} Zn(OH)_2(s) \xrightarrow{OH^-} [Zn(OH)_4]^{2-}(aq) \tag{5.8}$$

In contrary to that, magnesium is not amphoteric. Therefore, only $Mg(OH)_2$ according to the solubility product at higher pH ($p(K_{sp})$ = 11.25 [97]) is formed.

The amount of hydroxide ions in the solution determines directly the pH of the solution. It is well known that the solution pH plays an important role in the deposition mechansim, as well as the speciation of various species in the solution.

The main hydroxide source for ZnO deposition is ammonia since it provides hydroxide ions, aside from acting as complexing agent. Ammonia can either be added directly, as ammonium salt or as decomposition product of another species such as hexamethylentetramine (HMTA) or urea.

Ammonia is very soluble in water and acts as a weak base:

$$NH_4^+(aq) + OH^- \rightleftharpoons NH_3(aq) + H_2O(aq) \tag{5.9}$$

The equilibrium of this reaction lies almost entirely on the right of the arrow. At higher temperatures the reaction shifts to the left causing a higher ionization of ammonia.

HMTA is an often used reactant in the synthesis of ZnO nanorods from solution. Despite several discussions about the role of HMTA, it was shown that it has a double function as buffering agent, because of a slow hydroxide release from decomposition and as capping agent promoting nanorod growth through steric hindrance [111].

Decomposition of HMTA yields ammonia and formaldehyde:

$$(CH_2)_6N_4 + 6\,H_2O \longrightarrow 6HCHO + 4NH_3 \tag{5.10}$$

Other common hydroxide sources are the rather strong bases potassium hydroxide or sodium hydroxide. Since the tetrahedral ionic radius of sodium (0.99 Å[40]) is comparable with the one of zinc (0.60 Å[40]) sodium ions can theoretically be incorporated into the ZnO lattice. This incorporation can be avoided by using the potassium hydroxide, because potassium has a much larger ionic radius.

Because ammonia provides hydroxide ions as well as forms with zinc a tetraammine complex, this hydroxide source was chosen for the performed deposition within this thesis. The use of ammonia makes also sure that no other cations, which might be incorporated into the ZnO lattice, are present in the solution. Therefore Mg is the only cation available for incorporation.

Used reagent

Ammonium hydroxide NH_4OH

5.4.4 Additives

As additional reagents, complexing agents, as well as capping agents for changing the film morphology, are used.

The complexing agent is the essential ingredient in the chemical bath deposition process, since it allows a slow release of the metal salt for deposition. There are various possibilities that were already sucessful used in the deposition of ZnO such as ethane-1,2-diamine [112], dimethylamineborane [113], triethanolamine [112], HMTA [114] or ammonia [115].

Research on the influence of different complexing agents was done by [116]. Not with every complexing agent, uniform and transparent films were obtained. For example, if dimethylamine was used, homogeneous precipitation dominated, leading to poor-quality films.

The effect of different ammonium salts on the growth of ZnO films was investigated by Imai et.al. [102]. The mode of precipitation (homogeneous or heterogeneous) is influenced, besides the pH, by the molar ratio of complexing agent to zinc source. For low ratios $NH_4^+/Zn^{2+}\sim20$, deposition of ZnO with NH_4F took place between pH 9-10.5 for a high ratios $NH_4^+/Zn^{2+}\sim50$, ZnO films were only deposited at pH 11.5-12.5. The use of different ammonia salts did not give different results in terms of pH dependent ZnO deposition, since non of the cations coordinates with Zn^{2+} in the common deposition area of pH 9-13.

Ammonia was used in this deposition because it conveniently acts as hydroxide source, as well as a complexing agent, forming strong complexes with zinc and very weak ones with magnesium. This behaviour is useful to adjust the offset in solubility products between $Zn(OH)_2$ and $Mg(OH)_2$ as discussed in section 5.1. Further, a rather low ratio of NH_4^+/Zn^{2+} was chosen for the deposition.

Used reagent

Ammonium hydroxide NH_4OH

There is a wide range of capping agents available in literature, such as ethylenediamine, citrates, diblock compolymers and amino acids. These growth modifiers undergo face-specific reactions with distinct crystal faces changing the surface energies of distinct faces. This alters the growth rates of certain ZnO faces which results in a morphology change of the deposited film [117]. For example, citrate adsorbs strongly to the (001) face whereas ethylediamine adsorbs to the $(10\bar{1})$ face, causing different surface morphologies [118].

Citric acid and its esters (citrates) are widely used in the surface modification of ZnO films. There is a difference in the activity between various citrates and citric acid for modifying the ZnO growth direction. The activity depends on the concentration of fully ionized citrate anions. Therefore, citric acid and triammonium citrate suppress most effectively the growth in the (001) direction. The crystalline structure is also strongly dependent on the concentration of citric acid or citrates [117]. Besides their adsorption behaviour, citrates also form rather strong complex with Zn^{2+} and Mg^{2+}, acting as complexing agent.

Citric acid was used in the chemical bath recipe within this thesis, because it is known for its strong adsorption to the (001) face of ZnO surface, promoting lateral growth and thus, leading to a uniform and smooth film deposition even at low concentrations in the solution.

Used reagent

Citric Acid $C_5H_8O_7$

5.5 General Recipe

Zinc oxide films with and without magnesium were grown on cleaned Nesterion® B borosilicate glass substrates (2.5 x 2.5 cm^2 samples). In the first step the glass substrates were cleaned with washing solution Hellmanex® III (Hellma Analytics) under sonication at 50°C. In the subsequent cleaning steps, the glass slides were rinsed with pure water as well as isopropanol and blown dry by air. Then a seed layer of ZnO was spin coated (200 rpm, 60s) on the substrate surface with a solution of 50 mM ZnO in 5 M NH_4OH, followed by 5 min hot plate annealing in air at 100°C. The seed layer recipe was modified from [105]. Also ZnMgO samples were seeded solely with ZnO, but the same recipe could further be extended to a mixture of ZnO and MgO in the spin-coating solution.

Three separate stock solutions containing 0.8 M zinc nitrate hexahydrate ($Zn(NO_3)_2$ x 6 H_2O), 0.1 M magnesium nitrate hexahydrate ($Mg(NO_3)_2$ x 6 H2O), and 0.1 M citric acid (CA, $C_6H_8O_7$) were prepared. An open 150 ml beaker was filled with the chemical solution, containing different volumes of the stock solutions depending on the solution composition (see Table 5.1). Some experiments were done with varied citric acid concentrations between 0.5 and 4 mM. To achieve a solution pH of 10.8 at 25°C 4.7 ml of 28-30% ammonium hydroxide was added so that the total solution volume in the beaker was 100 ml.

Table 5.1: Volumes from stock solution for main solution compositions

mol% Mg in solution	V (Zn(NO3)2) [ml]	V(Mg(NO3)2) [ml]	V (Citric acid) [ml]	V (MQ water) [ml]
0	5 (40mM)	0	1 (1mM)	89
5	5 (40mM)	2 (2mM)	1 (1mM)	87
10	5 (40mM)	4.5 (4.5mM)	1 (1mM)	85
15	5 (40mM)	7 (7mM)	1 (1mM)	82
20	5 (40mM)	10 (10mM)	1 (1mM)	79

The beaker was almost entirely closed with a lid and heated up to 80°C under stirring on the hot plate. At a solution temperature of 80°C, measured with a thermocouple inserted in the solution, the substrate was immersed vertically for the depostion. After a certain amount of time - typically 15 min - the sample was removed from the bath, dipped in ultrapure water and blown dry by air to remove excess preciptates on the film surface. A sketch of the experimental set up can be seen in Figure 5.2

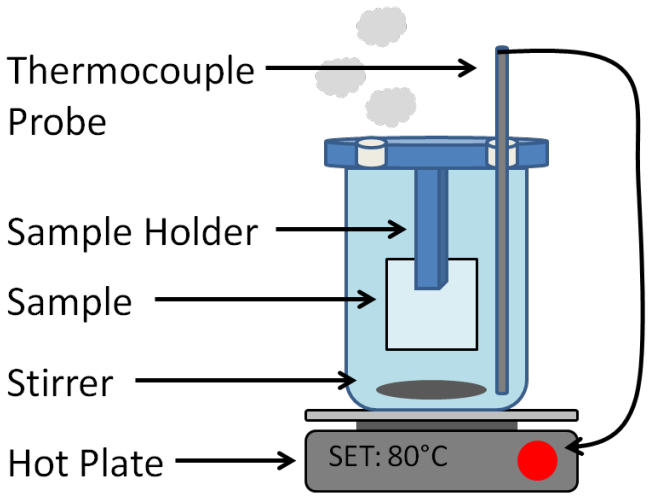

Figure 5.2: Experimental set-up for chemical bath deposition

To perform deposition at different pH values, the heating period was adjusted. The longer the solution was heated up, the lower the pH value was. The reason for that is controlled evaporation of ammonia through the holes in the lid covering the chemical bath. Also certain reactions and precipitates such as $Zn(OH)_2$ or $Mg(OH)_2$ contribute

to the pH decrease. An example for the pH variation with increasing heating periods can be seen in Figure 5.3. In this case 5 mol% Mg was added to the solution. pH variations slightly differ in solutions containing more Mg, because then $Mg(OH)_2$ is more likely to precipitate causing a faster decrease in pH with heating time. It was found by using a closed deposition bath, that the pH decrease of 0.1 mainly arises from reactions in the solution during a 15 minutes deposition. This suggests that ammonia evaporation is very low during such a short deposition time.

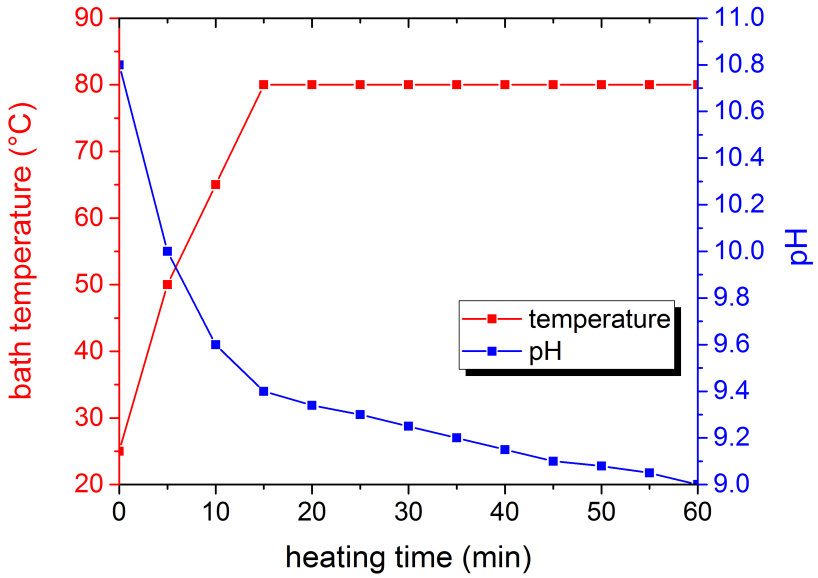

Figure 5.3: Temperature and pH profile with bath solution heating time for 5 mol% Mg solution

5.6 Speciation modelling

To get insights on the solution kinetics and the role of complexing agents on the deposition of ZnO, speciation modelling is a useful tool to understand the thermodynamic reactions. Since speciation modelling is widely used to estimate hazardous pollutants in the environment, various computerized chemical speciation models, based on thermodynamic knowledge, are available. These computer programs include [119] Visual MINTEQ, MEDUSA, JESS, PHREEQE, EQ3/6, SPECIES and HySS. Critical for these models are the thermodynamic databases in particular the values for the stability constants of the metal complexes. The programs Visual MINTEQ [120] and MEDUSA [121] include their own database. Visual MINTEQ data are based on the NIST database [122], while MEDUSA uses the integrated Hydra database [123], which is based on various sources. The reliability of published stability constants is difficult to estimate, since data diversity is drastic. Besides that, data for certain complexes are not available.

To understand what kind of species are in the solution some basic reactions are discussed firstly. Afterwards, speciation modelling was performed at 25° and 80°C. Therefore, data from different sources were used and compared.

5.6.1 Reactions leading to ZnO Formation

The starting material $Zn(NO_3)_2 \cdot 6\,H_2O$ immediately dissociates in water forming a complex with six water molecules $[Zn(H_2O)_6]^{2+}$ [111].

$$[Zn(H_2O)_6]^{2+} + H_2O \rightleftharpoons [Zn(H_2O)_5OH]^{+} + H_3O^{+} \tag{5.11}$$

$$[Zn(H_2O)_5OH]^{+} + H_2O \rightleftharpoons Zn(OH)_2 + H_3O^{+} + 4H_2O \tag{5.12}$$

Through forced hydrolysis, the H_2O molecules, as complexing ligands, are displaced by hydroxyl groups to form the solid zinc hydroxide. The oxide can be formed via deprotonation [124]:

$$Zn(OH)_2 \rightleftharpoons ZnO + H_2O \tag{5.13}$$

Zinc oxide is amphoteric and has in aqueous solution a high solubility at high and low pH. If ammonia is added in excess, a stable zinc tetraamine complex $[Zn(NH_3)_4]^{2+}$ is formed. Lange et.al. [115] showed through a thermodynamic analysis that this complex causes a high solubility of zinc over a wide range of pH. Furthermore, if the solution is heated to 90°C the pH region where the complex is formed shrinks to lower pH, causing a lower solubility of ZnO. This is referred as retrograde solubility [115]. Heating up the ammoniacal solution causes a supersaturation of ZnO, which provides the thermodynamic driving force for the chemical bath deposition of ZnO films onto substrates.

These reactions are involved in the equilibrium:

$$ZnO(c) + 3NH_3(aq) + 2\,H^{+}(aq) \rightleftharpoons [Zn(NH_3)_3]^{2+}(aq) + H_2O \tag{5.14}$$

$$ZnO(c) + 4NH_3(aq) + 2\,H^{+}(aq) \rightleftharpoons [Zn(NH_3)_4]^{2+}(aq) + H_2O \tag{5.15}$$

Since the high ammonia concentration (0.7 M) provides hydroxide ions in excess, also the formation of zinc hydroxide complexes is favored at higher pH:

$$ZnO + H_2O \rightleftharpoons Zn(OH)_2(aq) \tag{5.16}$$

$$ZnO + 2\,H_2O \rightleftharpoons [Zn(OH)_3]^-(aq) + H^+ \tag{5.17}$$

$$ZnO + 3\,H_2O \rightleftharpoons [Zn(OH)_4]^{2-}(aq) + 2\,H^+ \tag{5.18}$$

5.6.2 Speciation modelling of ZnO deposition

Table Table 5.2 gives a short summary of complex stability constants (log β) from four different sources, addressing the problem of data discrepancy. A zinc citrate complex was not considered because it is only stable at near neutral pH values.

Table 5.2: Stability constants (log β) for ZnO deposition from ammonia solution (25°C), in bold highlighted stabilities with large deviation compared to other sources

Reaction, stability of species	MINTEQ (NIST) [122]	Richardson and Lange [115]	IUPAC SC-Database [125]	Medusa (Hydra) [123]
Equation 5.9, NH_3	-9.24	-9.3	-9.47	-9.24
Equation 5.14, $[Zn(NH_3)_3]^{2+}$	-20.87	-23.3	7.31	7.1
Equation 5.15, $[Zn(NH_3)_4]^{2+}$	**-28.09**	**19.7**	9.46	9.3
Equation 5.16, $Zn(OH)_2$	-16.89	**-6.7**	-16.9	-16.4
Equation 5.17, $[Zn(OH)_3]^-$	-28.39	**-16.5**	-28.4	-28.2
Equation 5.18, $[Zn(OH)_4]^{2-}$	-41.19	**-29.3**	-41.2	-41.3

Since the deposition was carried out at 80°C the stability constants have to be calculated for higher temperature. A simple approximation is the Van't Hoff equation which assumes that the reaction enthalpy is independent from the temperature. Calculated stability constants for various data sources at 80°C are displayed in Table 5.3.

$$ln(\frac{\beta_2}{\beta_1}) = \frac{-\Delta H^{f_0}}{R}(\frac{1}{T_2} - \frac{1}{T_1}) \tag{5.19}$$

Furthermore, if solutions are highly concentrated, an ionic strength correction is necessary to obtain adequate results. Since the ionic strength was moderate in this case, no correction method was used. [119]

Based on the different data sources, four different diagrams were visualized with HySS software [126] for the given experimental concentrations at room temperature. As can be seen in Figure 5.4 the diagram based on NIST data drastically differs from the other diagrams. This is due to the much lower stability for the $[Zn(NH_3)_3]^{2+}$ complex (see also Table 5.2). Diagram Figure 5.4 (b) fits to the published diagram at 25°C from [115]. IUPAC and Hydra stability data predict a higher stability for the $[Zn(NH_3)_3]^{2+}$ complex. Besides that, data shows lower stability for the hydroxide complexes than data used by Richardson and Lange [115].

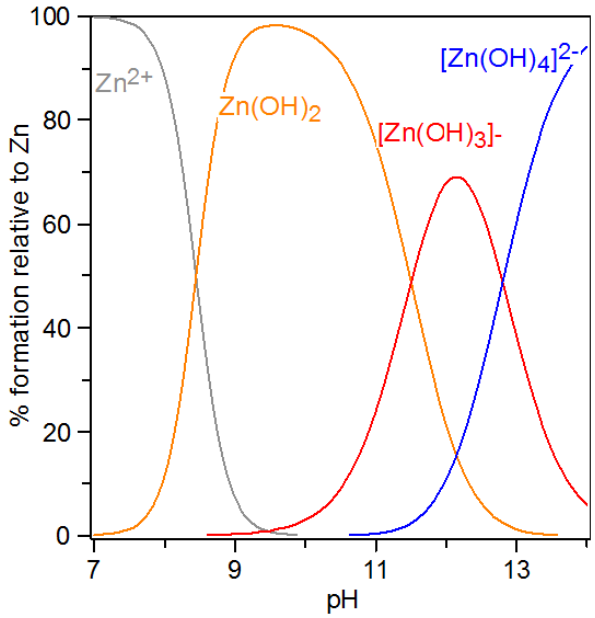

(a)25°C with MINTEQ (NIST) data

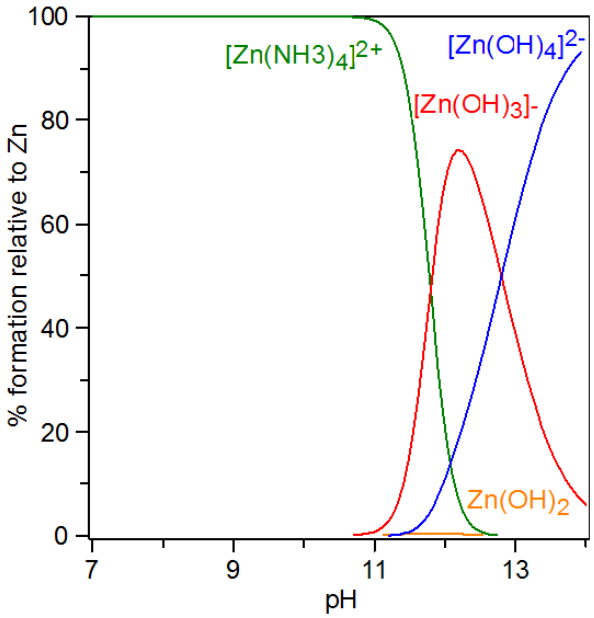

(b)25°C with Richardson & Lange data

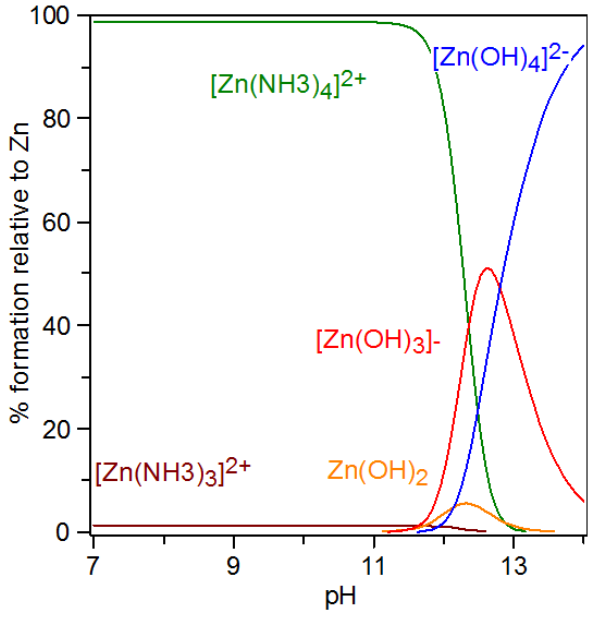

(c)25°C with IUPAC data

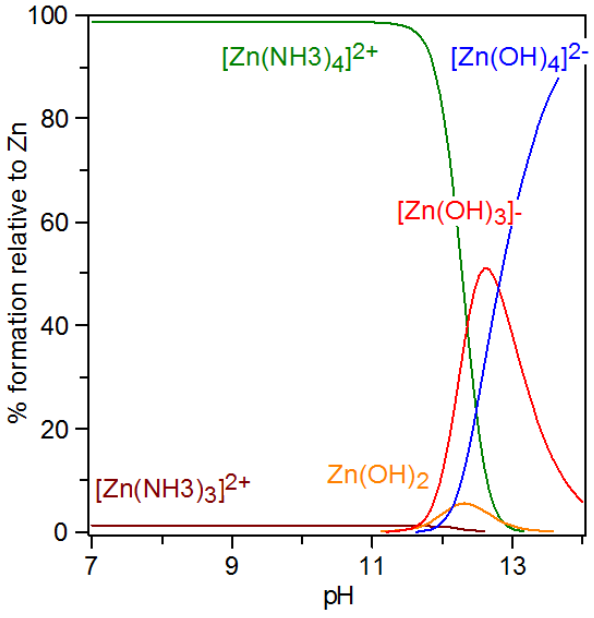

(d)25°C with Medusa (Hydra) data

Figure 5.4: Speciation diagrams ZnO deposition from ammonia solution modelled at 25°C with stability constants from various sources (see also Table 5.2)

Table 5.3: Stability constants (log β) ZnO deposition from ammonia solution at 80°C

Reaction, stability of species	MINTEQ (NIST) [122]	Richardson and Lange [115]	IUPAC SC-Database [125]	Medusa (Hydra) [123]
Equation 5.9, NH_3	-10.66	-10.72	-10.89	-10.66
Equation 5.14, $[Zn(NH_3)_3]^{2+}$	-24.04	-26.47	4.14	3.93
Equation 5.15, $[Zn(NH_3)_4]^{2+}$	-32.08	15.71	5.47	5.31
Equation 5.16, $Zn(OH)_2$	-16.89	-6.7	-16.9	-16.4
Equation 5.17, $[Zn(OH)_3]^-$	-28.39	-16.5	-28.4	-28.2
Equation 5.18, $[Zn(OH)_4]^{2-}$	-41.19	-29.3	-41.2	-41.3

Using Van't Hoff approximation and enthalpy values from the NIST database [122], speciation diagrams were calculated at 80°C. Again the diagram based on NIST stability constants data is completely different compared to the other diagrams. Diagram Figure 5.5 (b) at 80°C fits to the published diagram modelled at 90°C by [115]. This means that the Van't Hoff approximation is in good agreement with other temperature correction methods for stability constants. Calculated stability constants for various data sources at 80°C can be seen in Table 5.3

In general, complexation of zinc with ammonia is less favored at higher temperatures. Aqueous $Zn(OH)_2$ formation, which is essential for the ZnO deposition, is more stable at higher temperatures. Besides that, formation of $Zn(OH)_2$ is shifted to lower pH values with increasing temperature.

5.6.3 Reactions leading to Mg doped ZnO Formation

The magnesium ion from the $Mg(NO_3)_2 \cdot 6\,H_2O$ salt hydrolyses in solution immediately to form complexes with water molecules, similar to the reactions for zinc (see Chapter subsection 5.6.1).

Since Mg doped ZnO thin films were never deposited via chemical bath deposition with this composition, details about the mechanism are not known. From basic chemistry knowledge, following reactions most likely play a role in the deposition process:

$$Mg^{2+} + 2NH_3(aq) \rightleftharpoons [Mg(NH_3)_2]^{2+}(aq) \tag{5.20}$$

$$Mg^{2+} + [C_6H_5O_7]^{3-} \rightleftharpoons [Mg(C_6H_5O_7)_2]^{-}(aq) \tag{5.21}$$

$$Mg^{2+} + H_2O \rightleftharpoons [Mg(OH)]^{+}(aq) + H^{+} \tag{5.22}$$

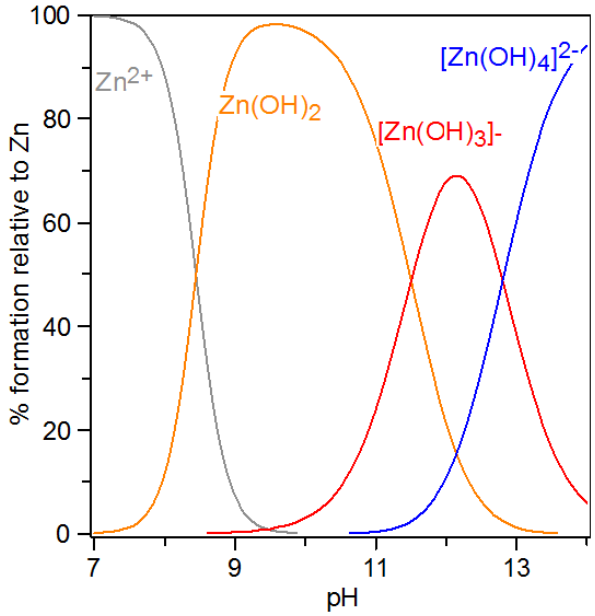

(a)80°C with MINTEQ (NIST) data

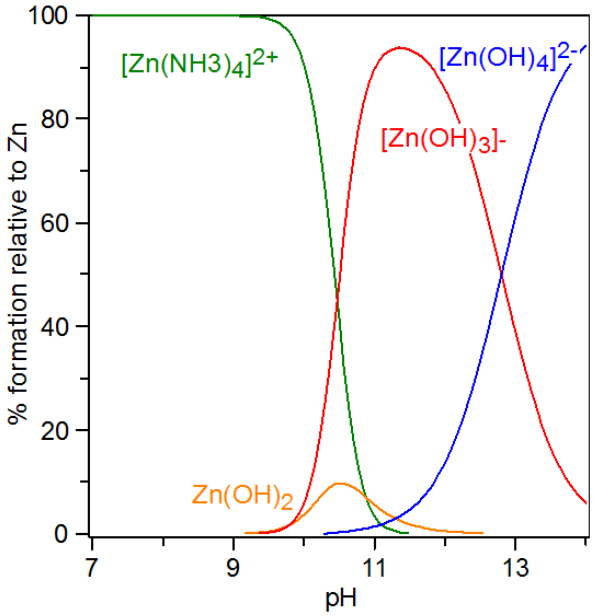

(b)80°C with Richardson & Lange data

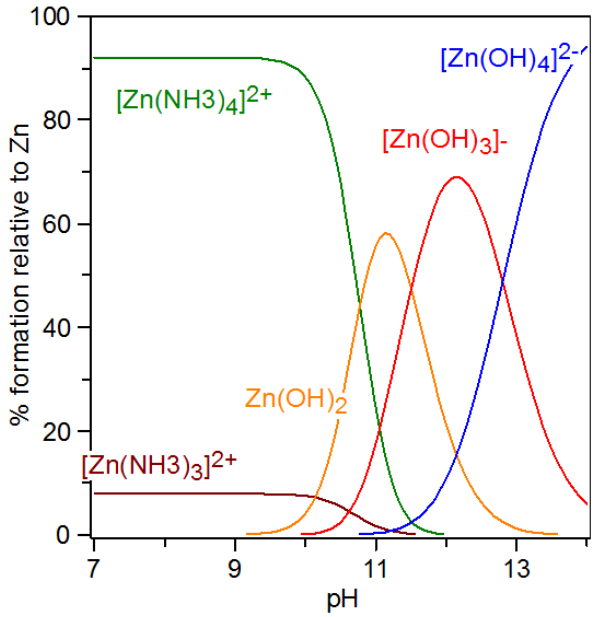

(c)80°C with IUPAC data

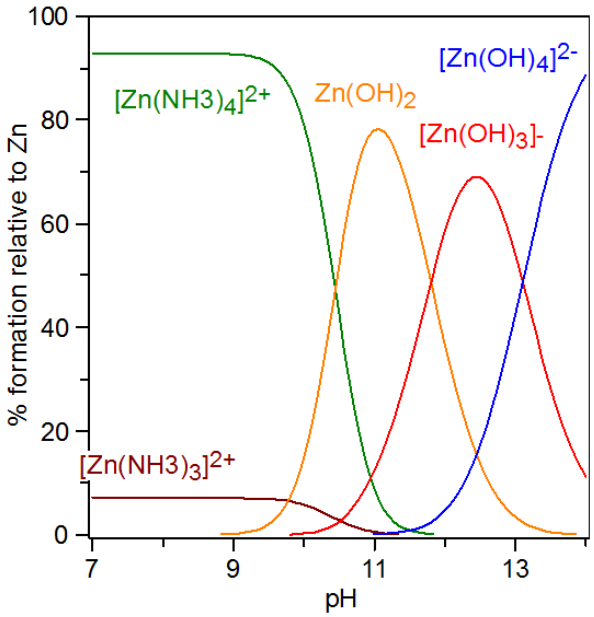

(d)80°C with Medusa (Hydra) data

Figure 5.5: Speciation diagrams ZnO deposition from ammonia solution modelled at 80°C with stability constants from various sources (see also Table 5.3)

Magnesium does only form a weak complex with ammonia in comparison to zinc. At pH greater 7 magnesium is partly complexed with citric acid to form $[Mg(C_6H_5O_7)]^-$. The rest of magnesium stays as Mg^{2+} ions and magnesium hydroxo ions $[Mg(OH)]^+$ in solution.

5.6.4 Speciation modelling of Mg doped ZnO deposition

Stability constants for the reaction of magnesium and zinc in ammoniacal solution are displayed in Table 5.4 for 25 °C. Since citric acid is involved also the dissociation constants of the triprotonic acid have to be considered. Stability constants approximated with Van't Hoff approximation at 80°C are displayed in Table 5.5

Table 5.4: Stability constants (log β) for the reactions in CBD of Mg doped ZnO at 25°C, in bold highlighted stabilities with large deviation compared to other sources

Reaction	MINTEQ (NIST) data base [122]	IUPAC SC-Database [125]	Medusa [123]
$Mg_2^+ + 2NH_3 \rightleftharpoons [Mg(NH_3)_2]^{2+}$	**-18.29**	0.06	0.20
$Mg_2^+ + H_2O \rightleftharpoons [Mg(OH)]^+ + H^+$	-11.42	-11.44	-11.44
$Mg_2^+ + [C_6H_5O_7]^{3-} \rightleftharpoons [Mg(C_6H_5O_7)_2]^-$	4.89	3.49	4.89
$Zn_2^+ + [C_6H_5O_7]^{3-} \rightleftharpoons [Zn(C_6H_5O_7)_2]^-$	6.06	4.71	6.25
$C_6H_8O_7 \rightleftharpoons [C_6H_7O_7]^- + H^+$	14.29	14.29	14.29
$[C_6H_7O_7]^- \rightleftharpoons [C_6H_6O_7]^{2-} + H^+$	11.16	11.16	11.16
$[C_6H_7O_7]^- \rightleftharpoons [C_6H_5O_7]^{3-} + H^+$	6.40	6.40	6.40

Table 5.5: Stability constants (log β) for the reactions in CBD of Mg doped ZnO at 80°C

Reaction	MINTEQ (NIST) data base [122]	IUPAC SC-Database [125]	Medusa [123]
$Mg_2^+ + 2NH_3 \rightleftharpoons [Mg(NH_3)_2]^{2+}$	-20.99	-2.64	-2.50
$Mg_2^+ + H_2O \rightleftharpoons [Mg(OH)]^+ + H^+$	-9.57	-9.59	-9.59
$Mg_2^+ + [C_6H_5O_7]^{3-} \rightleftharpoons [Mg(C_6H_5O_7)_2]^-$	4.67	3.27	4.67
$Zn_2^+ + [C_6H_5O_7]^{3-} \rightleftharpoons [Zn(C_6H_5O_7)_2]^-$	5.84	4.49	6.03
$C_6H_8O_7 \rightleftharpoons [C_6H_7O_7]^- + H^+$	14.36	14.36	14.36
$[C_6H_7O_7]^- \rightleftharpoons [C_6H_6O_7]^{2-} + H^+$	11.12	11.12	11.12
$[C_6H_7O_7]^- \rightleftharpoons [C_6H_5O_7]^{3-} + H^+$	6.31	6.31	6.31

NIST data predict a much lower stability for the $[Mg(NH_3)_2]^{2+}$ complex than the other data sources. Since the deposition was carried out at 80°C, the magnesium ammine complex is not stable at that temperature anyway. Besides that, NIST data for other

complexes predict about the same stabilities as Medusa data. IUPAC data deviate only little from the other two sources. In Figure 5.6 IUPAC data were compared with Medusa data for solutions containing 5 mol% Mg and 1 mM citric acid. The stability difference of Mg-citrate comparing these two data sources, causes some deviations in the diagrams. Basically it can be seen that in both diagrams the concentration of $[Mg(OH)]^{+}$ increases at higher pH. $MgCit^{-}$ has a stable concetration in the pH range (8.8-9.3), in which the deposition was carried out. Mg^{2+} concentration increases with lower pH.

Since zinc is not involved in these equilibria, only Mg was considered. For zinc speciation in this solution, the diagrams from subsection 5.6.2 are valid with little differences in complex stabilities caused by the interaction with various Mg species.

Since Medusa data were similar to the NIST database, these stabilities were chosen to model further solution. The source of these concrete complex stability constants is from Martell et al. [127]. This was evaluated as a reliable source.

In Figure 5.7 speciation diagrams at 80°C for solutions with 5 mol% Mg and different citric acid concentrations can be seen. The more citric acid is present in the solution the more Mg-citrate complex is formed in the interesting pH region 8.8-9.3. This decreases simultanously the Mg^{2+} and $Mg(OH)^{+}$ concentrations in the solution.

Different concentrations of Mg in solution with 1 mM citric acid at 80°C are displayed in Figure 5.8. Increase in $Mg(NO_3)_2$ concentration causes an higher amount of Mg^{2+} ions in the solution at the measured solution pH of 8.8-9.3. At the same time the amount of Mg-citrate stays the same at 1 mM. Concentrations of $Mg(OH)^{+}$ ions also increase with more Mg precursor salt.

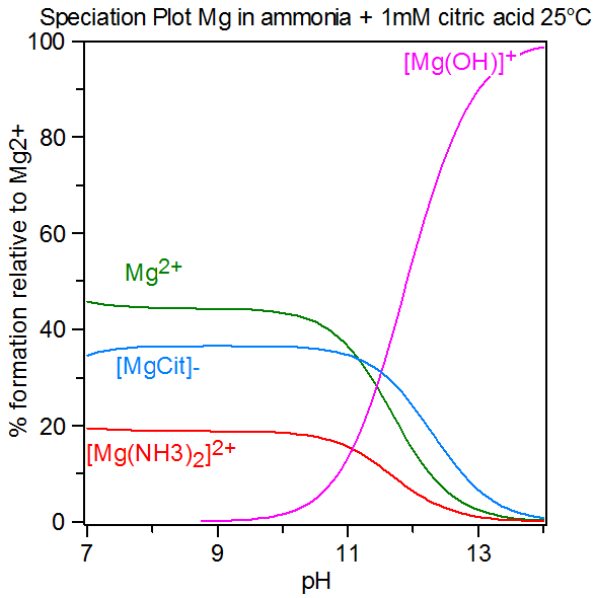

(a)25°C with IUPAC data

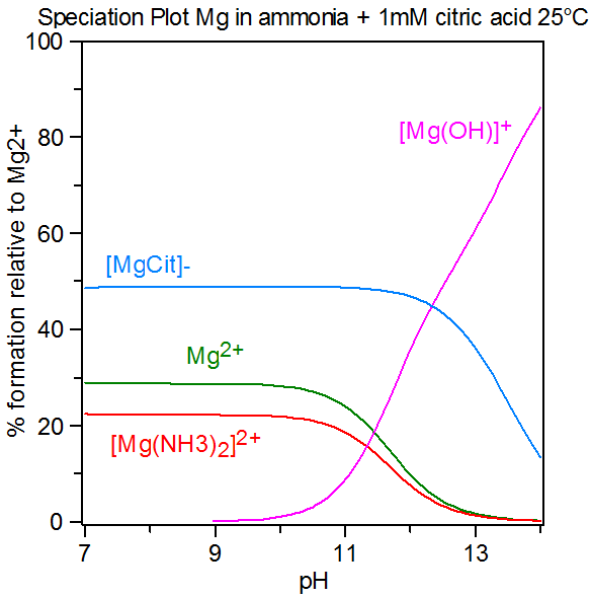

(b)25°C with Medusa (Hydra) data

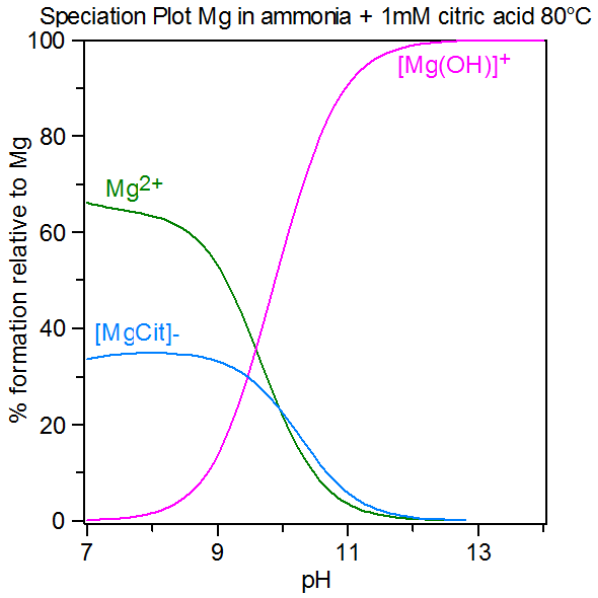

(c)80°C with IUPAC data

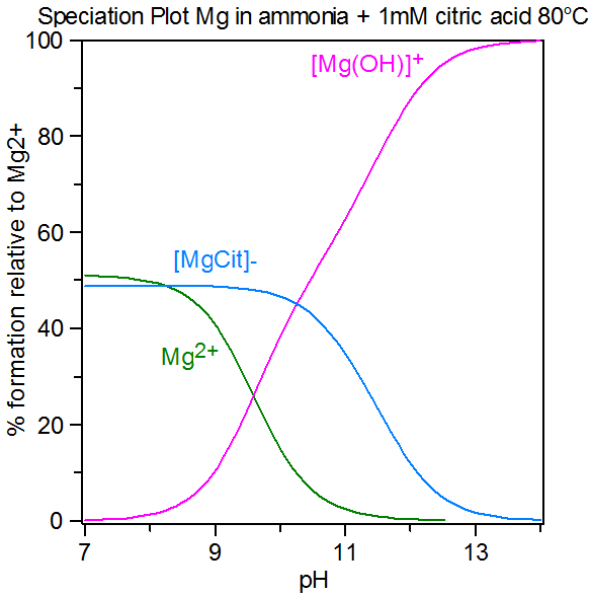

(d)80°C with Medusa (Hydra) data

Figure 5.6: Speciation diagrams 0.002 mM $Mg(NO_3)_2$ in ammonia/citric acid solution modelled at 25 and 80°C with different data sources

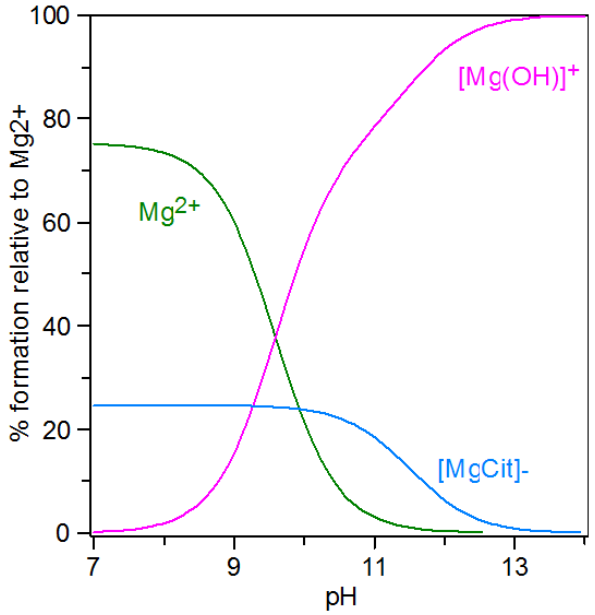

(a)5 mol% Mg 0.5 mM citric acid

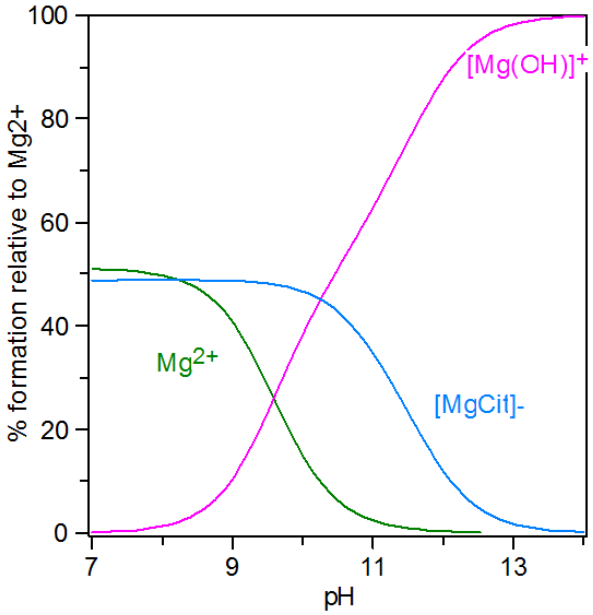

(b)5 mol% Mg 1mM citric acid

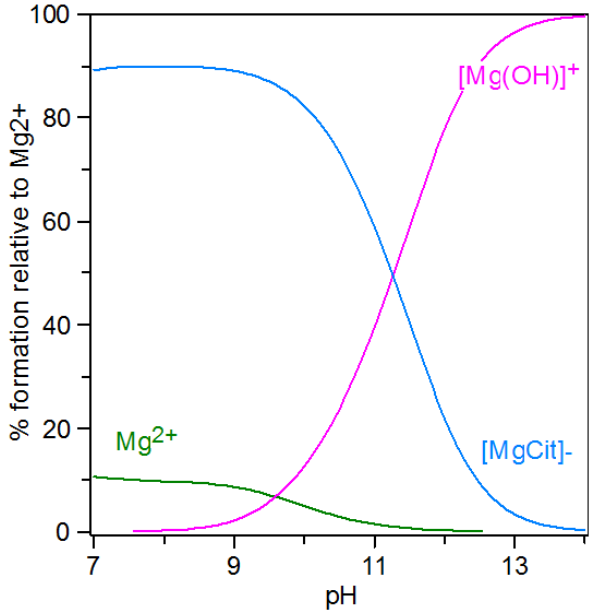

(c)5 mol% Mg 2mM citric acid

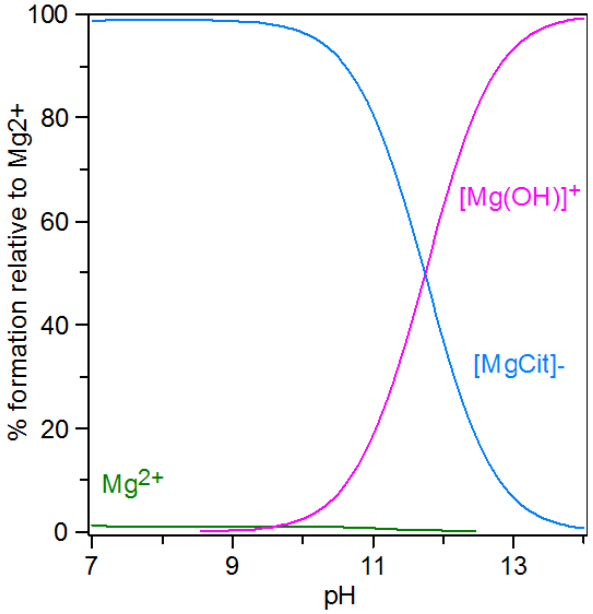

(d)5 mol% Mg 4mM citric acid

Figure 5.7: Speciation diagrams 0.002 mM $Mg(NO_3)_2$ in ammoniacal solution with different citric acid concentrations modelled at 80°C with data from the Hydra (Medusa) database

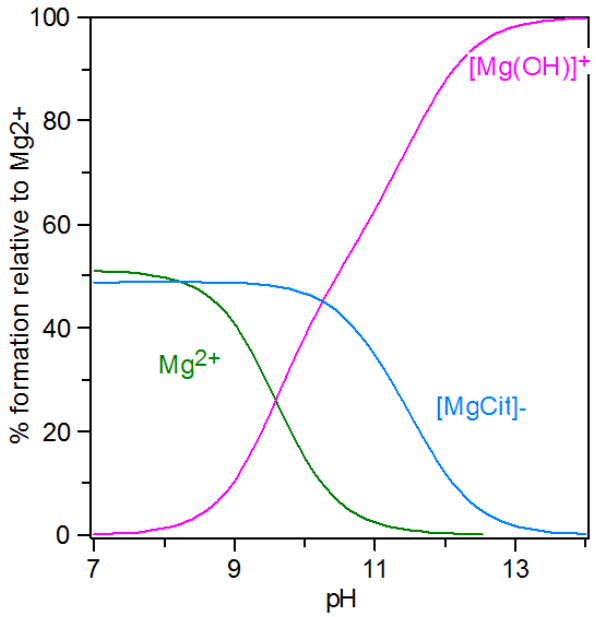

(a)5 mol% Mg (2 mM of $Mg(NO_3)_2$)

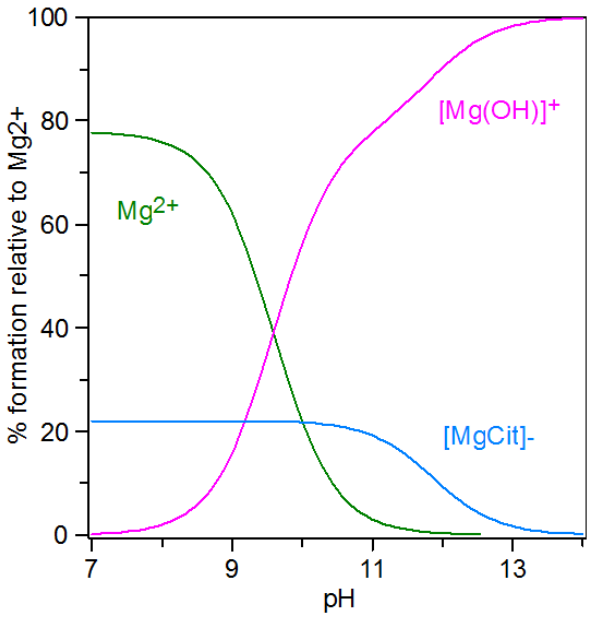

(b)10 mol% Mg (4.5 mM of $Mg(NO_3)_2$)

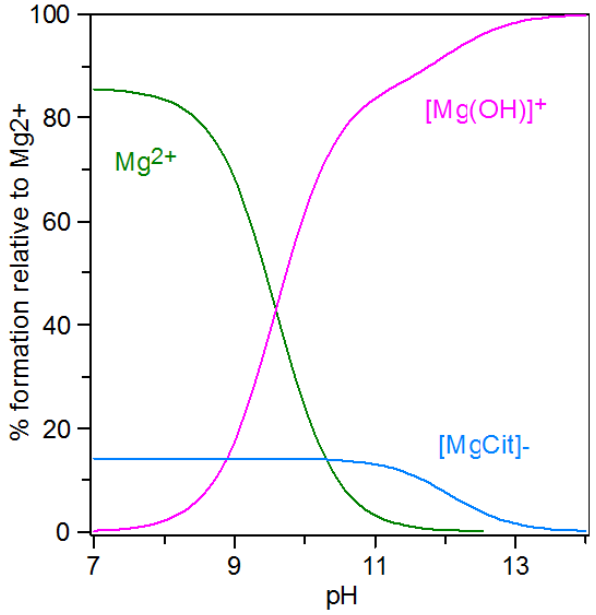

(c)15 mol% Mg (7 mM of $Mg(NO_3)_2$)

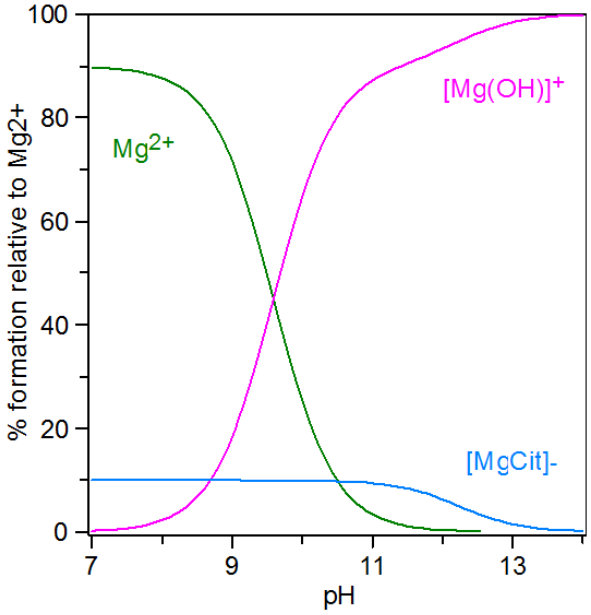

(d)20 mol% Mg (10 mM of $Mg(NO_3)_2$)

Figure 5.8: Speciation diagrams with different concentrations of $Mg(NO_3)_2$ in ammoniacal solution with 1mM citric acid modelled at 80°C with data from the Hydra (Medusa) database

6 Results and Discussion

6.1 Growth and Properties of ZnO films

The chemical bath deposition of ZnO involves the forced hydrolysis of metal complexes from the aqueous solution. This process involves the dehydration of $Zn(OH)_2$ species to ZnO, as discussed before. There is always an equilibrium between the formation of ZnO and $Zn(OH)_2$, which shifts, for temperatures higher than 60°C, almost entirely to the deposition of ZnO [110]. The supersaturation of $Zn(OH)_2$ is considered the thermodynamic driving force for nucleation and film growth. Therefore, the deposition of a high quality ZnO film requires the careful control of the $Zn(OH)_2$ supersaturation level, which is usually achieved by the complexation of the metal species.

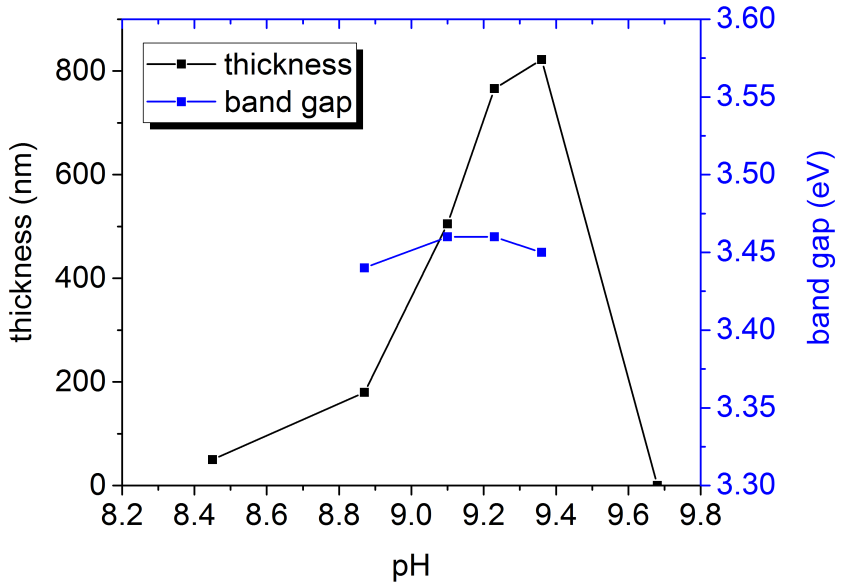

Figure 6.1: pH dependence of ZnO deposition

In the previous chapter speciation modelling gave insight on the distribution of the various Zn species in the chemical bath solution, in dependence of the pH (see also subsection 5.6.2). Experimentally it was seen that the deposition can only be carried out within the narrow pH window 8.4-9.7, as shown in Figure 6.1. It was observed that at the substrate immersion pH of 9.36 (at 80°C) the solution was still translucent,

while at pH=9.20 homogenous precipitates rendered the solution blurry. At pH=8.45 the solution became "milky", as further $Zn(OH)_2$ precipitation occurred. A high level of supersaturation is characterized by the dominance of homogeneous over heterogeneous precipitation. This was experimentally observed at low pH (< 9.00), where the the lack of heterogeneous precipitation strongly suppressed the film growth

These experimental results are in contradiction to speciation models of the solution at 80°C, based on various data sources (see Figure 5.5). All models predict a supersaturation of the aqueous $Zn(OH)_2$ around pH = 11. As mentioned before, the aqueous or solid $Zn(OH)_2$ in equilibrium with ZnO, is the key to film deposition. On the other hand, the experiments showed that, a high supersaturation of $Zn(OH)_2$ occurred for pH < 9 and a low supersaturation level within a narrow window around pH=9.20. In the following, several reasons for the discrepancy between the experimental results and the theoretical models are given.

First of all, speciation modelling depends on the data for complex formation constants and formation enthalpies, for which reliable sources are often in contradiction (see discussion in Table 5.2). The main problem is that there is no standardized method for determining these values. Therefore, the available data might not be accurate enough. Further, also the approximation of the complex formation constant at 80°C via the Van't Hoff equation has to be examined critically. Alternative approximations depend on the quality of the thermodynamic data for enthalpy, entropy and heat capacity at 80°C, which leads to even more uncertainties. An exact speciation model would also include the ionic strength, which is in most cases neglected due to the additional complexity (within this experimental work an ionic strength of 0.5 at 25°C was estimated). Another difficulty for the speciation modelling arises due the wide variety of the mixed hydroxide and ammonia complexes for which no data is available.

Considering these problems, we can conclude that the speciation modelling can certainly give fundamental insights on the solution chemistry and is therefore a useful qualitative tool, but its accuracy is limited and deviations from experimental results are to be expected.

To have an agreement with the experiment, the theoretically derived $Zn(OH)_2$ supersaturation should be in the pH range of 8-10. In order to demonstrate the sensitivity of the speciation curves on the complex stabilities, data from the reliable source (Richardson and Lange [115]) were considered and the complex stabilities of $Zn(OH)_2$ and $[Zn(NH_3)_4]^{2+}$ were adjusted to match the experimental results.

The stability constant β of $[Zn(NH_3)_4]^{2+}$ at 80°C is 15.71 according to [115]. If the stability of the ammine complex is decreased, $Zn(OH)_2$ supersaturation shifts to the lower pH region. This decrease in stability is in accordance with data from other sources (see Table 5.2), which propose lower stabilities for $[Zn(NH_3)_4]^{2+}$. The pH dependence of the $Zn(OH)_2$ concentration for decreasing $[Zn(NH_3)_4]^{2+}$ stability values is depicted in Figure 6.2 (a). We should point out that possible reasons for the decreased zinc amine stability can be the presence of various mixed zinc hydroxide and ammine complexes, as well as the adsorption of zinc ammine on the ZnO film.

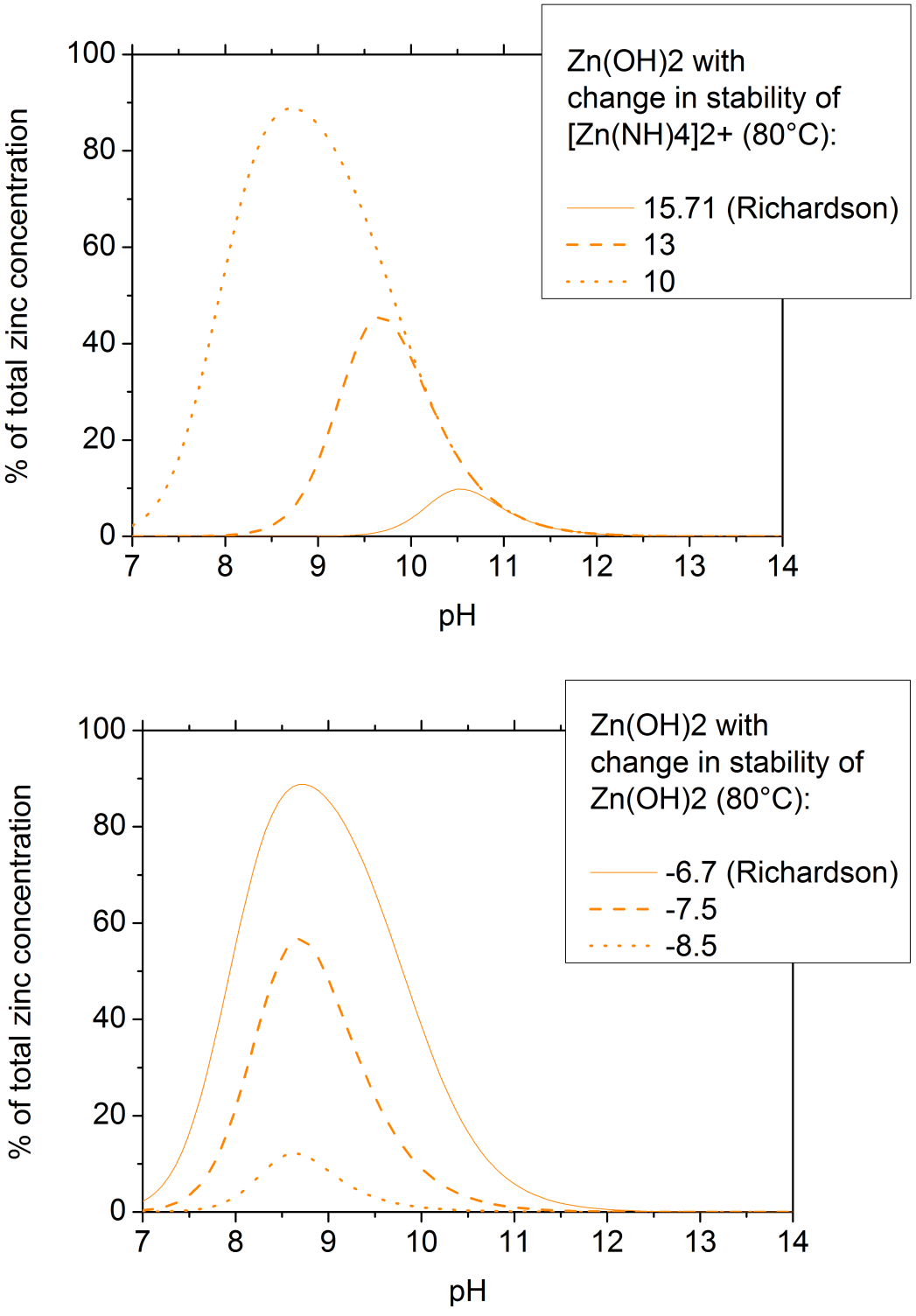

Figure 6.2: Optimization of stability constant of a) complex $[Zn(NH_3)_4]^{2+}$, b) complex $Zn(OH)_2$ values from [115]

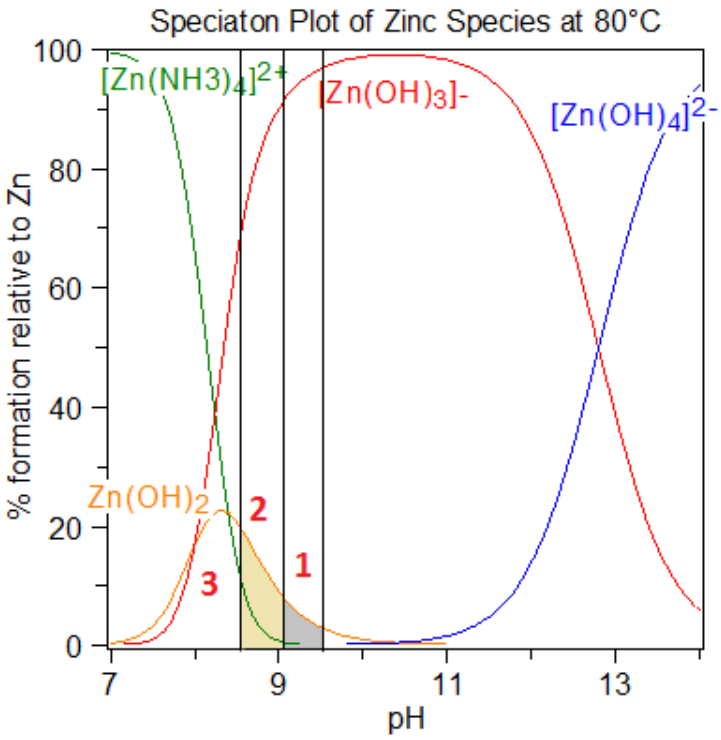

Figure 6.3: Speciation diagram of ZnO in ammonia solution at 80°C with formation constants fitted to experimental data

Further, even a small decrease in the $Zn(OH)_2$ stability, narrows the pH window notably, as seen in Figure 6.2 (b). The lower stability fits also to data from other sources (see Table 5.2). A diagram with stability constants adjusted to experimental results can be seen in Figure 6.3.

As explained in detail by O'Brien et. al. [108], in the region of low supersaturation, heterogeneous nucleation dominates and the crystal faces grow via ion-by-ion mechanism, as explained in section 5.2 (see region 1 in Figure 6.3). At higher level of supersaturation (region 2 in Figure 6.3) growth occurs via a mixture of ion-by-ion and cluster-mechanism on crystal faces. If the supersaturation is very high, homogeneous nucleation dominates and no film can be formed on the substrate (region 3 in Figure 6.3). To see which growth mechanism is dominant at a specific pH, the film morphology was investigated by XRD and SEM . From the SEM pictures it is difficult to distinguish morphological differences between the films grown at different pH, partly due to significant thickness variations between the films (see also Figure 6.4).

XRD spectra of the same samples showed that all films grow predominantly along the (002) direction, as shown in Figure 6.5. The thinnest film, grown at pH=8.45, is polycrystalline, with the (101), (002) and (103) reflections being most prominent. Indeed, the presence of multiple reflections in thin ZnO films is due to the competitive type of growth. As the films grow thicker, the fastest growing face (along the (002) direction) gradually dominates.

ZnO grows mainly in the (002) direction because citric acid selectively adsorbs onto

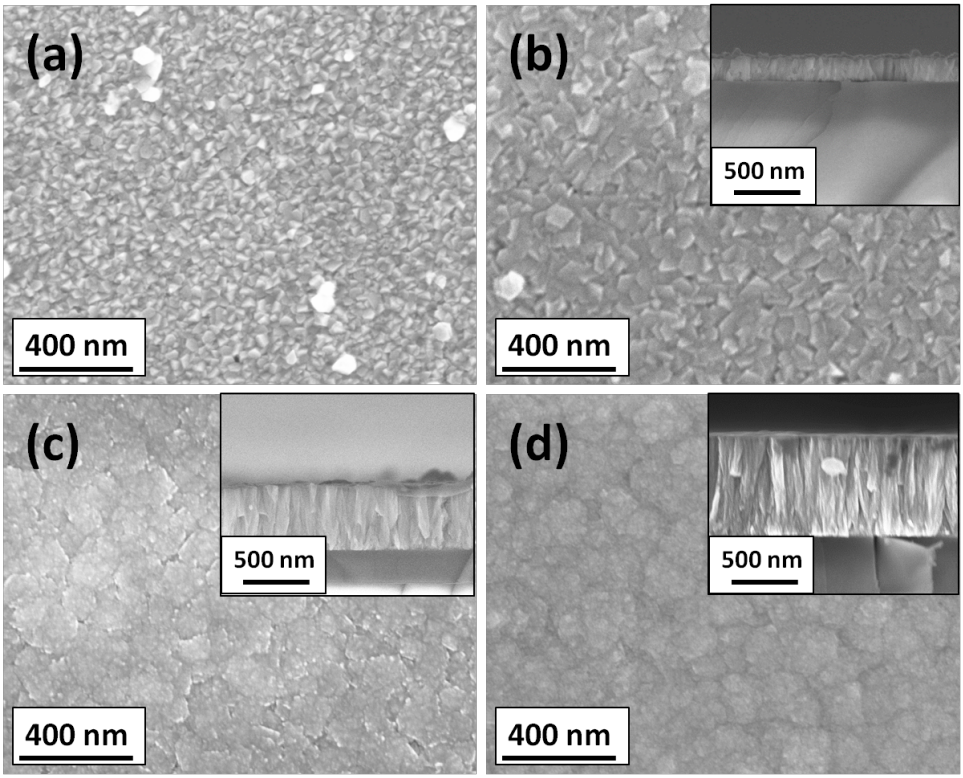

Figure 6.4: SEM pictures of ZnO thin films deposited at pH (a) 8.45, (b) 8.87, (c) 9.10, (d) 9.23

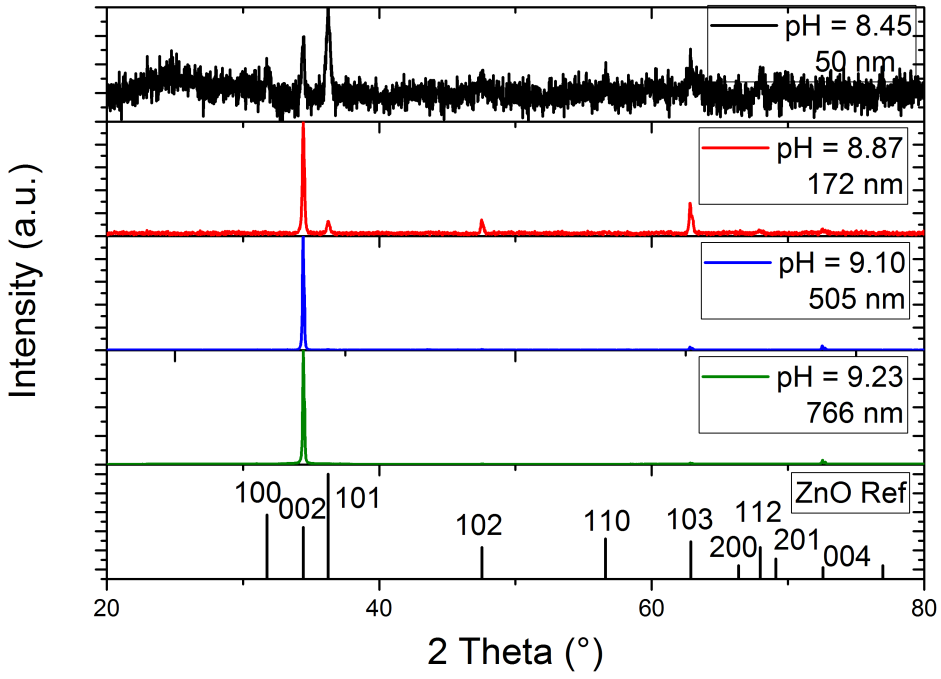

Figure 6.5: XRD spectra of ZnO films deposited at different pH values

the (002) plane, stabilizing it. This was confirmed by an experiment where citric acid was not added to the chemical bath deposition. In this case, the (002) plane is not adequately stabilized and growth proceeds through exposing the most stable ZnO faces, such as (101) or (100). The energetically most favorable morphology without stabilization of any crystal plane, are nanorods as shown in the SEM pictures of Figure 6.23. In order to deposit a dense film instead of a nanorod array, the addition of citric acid to the bath solution was proven essential.

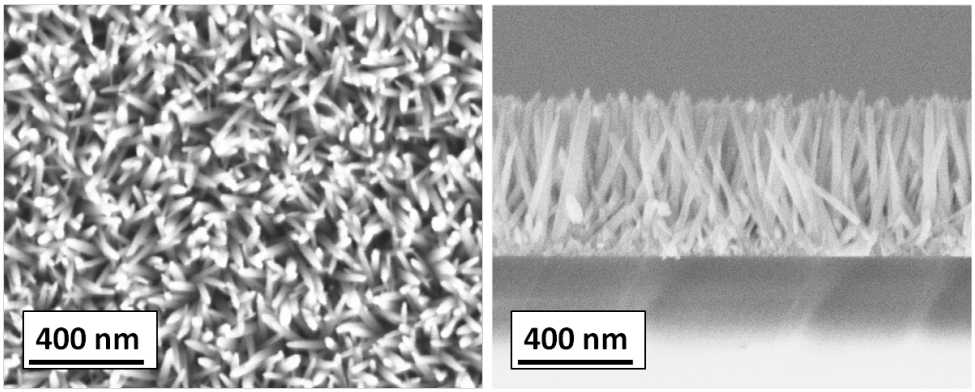

Figure 6.6: SEM pictures of ZnO deposition at pH = 9.2 without citric acid

The optical transmittance spectra of the ZnO films were measured (Figure 6.7) and through the Tauc's plot method the band gap was extracted for every case (insets of Figure 6.7). The transmittance was > 80% in the visible range for all ZnO films. The abrupt absorption edge and the appearance of clear interferences are illustrative of the compact character of the deposited films. The extracted band gap for all films was 3.46, except for the thinnest deposited at pH = 8.45, where a lower value of 3.38 eV was extracted. These calculated band gaps are rather high compared to the literature value of 3.37 eV [29]. The reason for this might be the presence of a small amount of $Zn(OH)_2$ in the films. It was proposed by [110] that if chemical bath deposition is performed at temperatures higher than 60°C only ZnO is present. In the same publication it was shown that deposition at 50°C always led to the presence of $Zn(OH)_2$, which increased the band gap from 3.2 to 3.7 eV. In our case $Zn(OH)_2$ was not detected by XRD, but it is possible that a small amount of it is either amorphous or accumulated in grain boundaries.

To sum up, many details about the ZnO growth mechanism are still unknown. The decrease in stability of the zinc-tetraamine complex with higher temperature is often considered as the driving force for the deposition, since it controls the supersaturation of $Zn(OH)_2$ as precursor for ZnO deposition. The stability of $Zn(OH)_2$ at 80°C determines therefore the pH range for ZnO deposition. If the temperature is increased, the stability of the zinc ammine complex decreases. Because of this, the driving force for deposition is higher, allowing ZnO film formation over wider pH range.

Face-selective adsorption is known to play an important role in the deposition process. Besides citrate, there are also positively charged zinc-ammine complexes as well as negatively charged zinc-hydroxide complexes present in the solution.

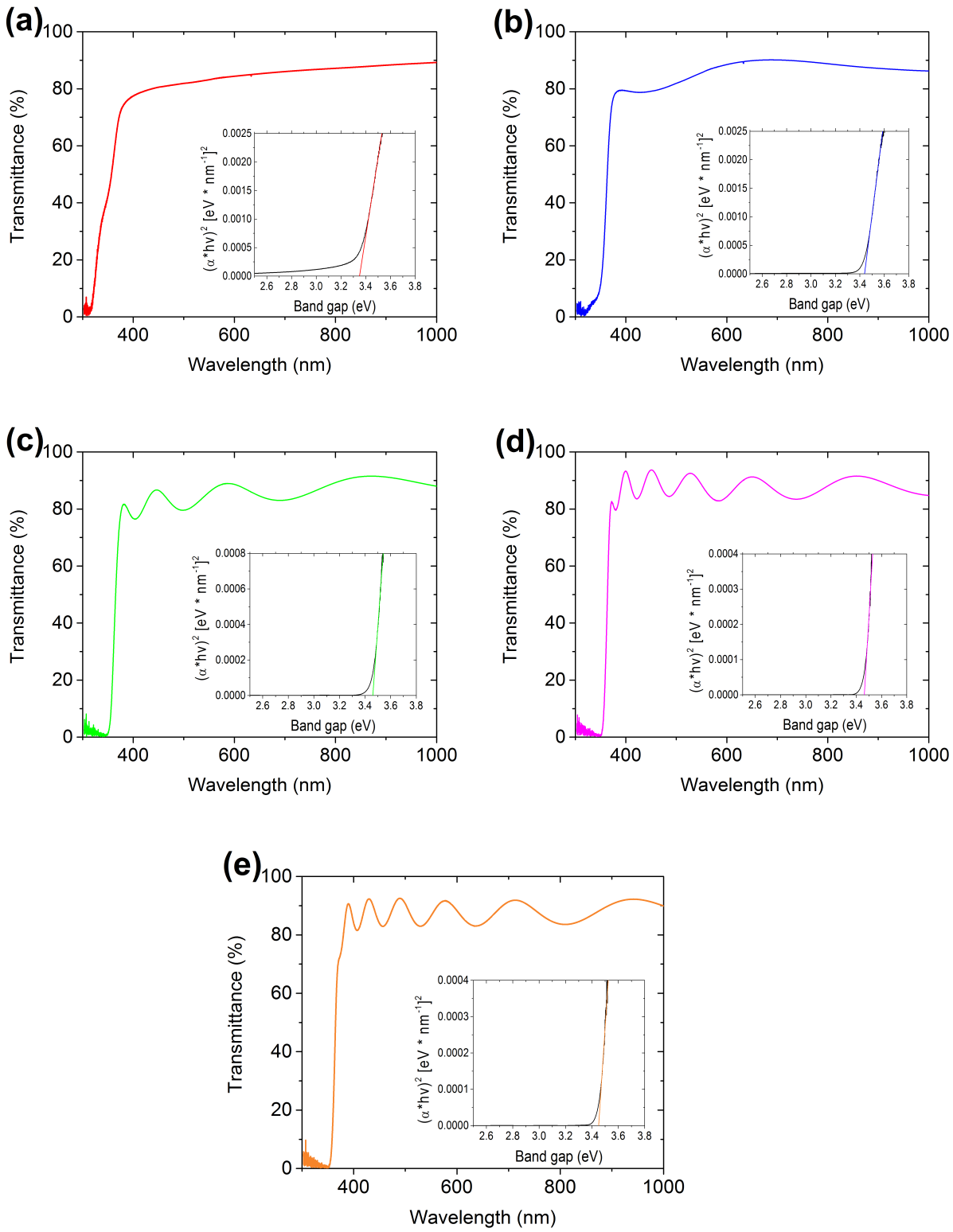

Figure 6.7: Transmittance Spectra and Tauc's Plot for (a) pH=8.45, (b) pH=8.87, (c) pH=9.10, (d) pH=9.23, (e) pH=9.36

Since citric acid is known to adsorb very strong onto the (002) plane, compared to

the Zn metal complexes (see also [118]), (002) is the most stabilized surface plane. Experiments confirmed that if citric acid was not added to the deposition solution, a vertically aligned nanorod array was deposited.

6.2 Growth and Properties of ZnMgO films

As seen in Figure 6.1 the pH window for ZnO deposition is between 8.4-9.7. With increasing magnesium concentration in the solution, the pH window becomes narrower and is simultaneously shifted to lower pH values, as illustrated in Figure 6.8.

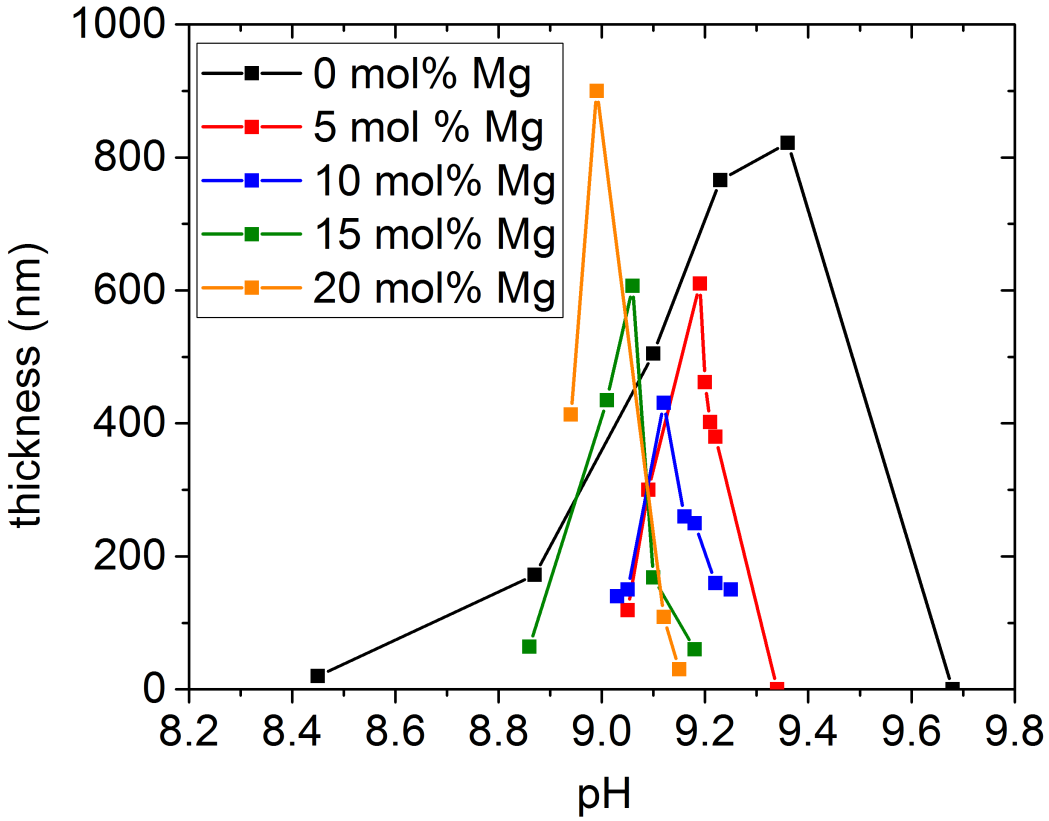

Figure 6.8: pH dependence of Mg doped ZnO deposition with various mol% Mg in solution

The ZnO growth is in general influenced by various parameters, such as the temperature, the level of supersaturation and the solution composition. The addition of Mg can further influence the growth by face-selective adsorption of specific Mg species onto certain ZnO crystal faces, but also via the possible precipitation of $Mg(OH)_2$ in the solution. The much narrower pH deposition window for ZnMgO as compared to ZnO, suggests a smaller driving force for film growth . This claim is supported by an experiment, where two depositions from the 5 mol% Mg solution were carried out,

one at 80 and the other at 90 °C at pH=9.1. SEM cross sections for the two films are presented in Figure 6.9. Clearly, a much thicker film is obtained at higher temperature. The two films have comparable optical transmittance and bandgap values (3.47 eV) as seen in Figure 6.10. Indeed, films of considerable thickness could be even deposited at pH=8.9 when the bath temperature was raised to 90 °C, showing the decisive role of the temperature as driving force for the films' growth. We note here that the majority of the experiments in this thesis took place at 80 °C, taking into account the faster ammonia evaporation at higher temperatures, leading to a more difficult control of the solution pH over time.

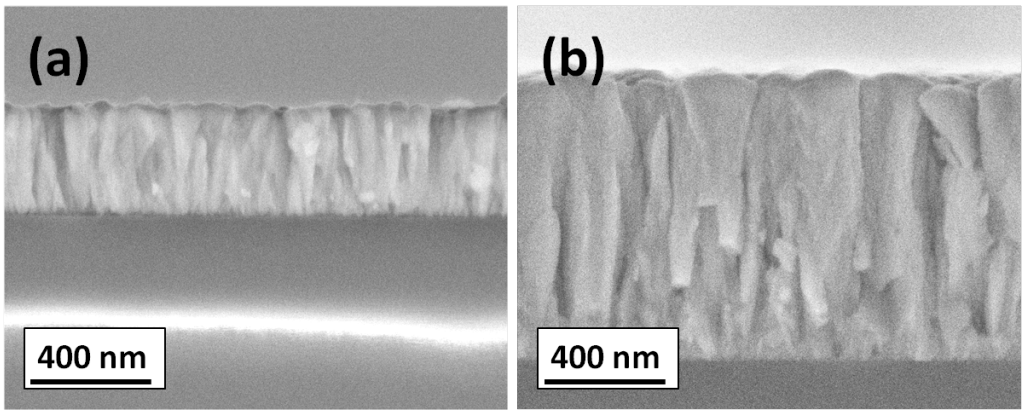

Figure 6.9: SEM crosssection of films deposited from 5 mol% Mg solution at pH = 9.1 and a temperature of (a) 80°C and (b) 90°C

In the following paragraph we will try to give an explanation for the narrowing of the deposition pH window, combined with its shift to lower pH values for increasing Mg content in the solution.

Figure 6.11 shows the concentration of $[Mg(OH)]^+$ versus pH for increasing amount of Mg in the solution, as extracted from the speciation diagrams Figure 5.8. In the same pH regime the Mg citrate concentration remains practically unchanged. The $[Mg(OH)]^+$ is assumed to give rise to larger $Mg(OH)_2$ precipitation. In the experiments we indeed observed the increase of the solid precipitation with increasing amount of Mg. An alteration of the relative stability of the various complexes in the solution would give rise to a corresponding alteration in the $Zn(OH)_2$ supersaturation window, which can explain the shift of the pH deposition window.

Another information derived from Figure 6.8 is the dependence of the growth rate on the Mg content in the solution. Films deposited from 10 mol% Mg solutions had the lowest growth rate and the ones deposited from the 20 mol% solution the highest, i.e. similar to the pure ZnO deposition. In the latter case, most of the Mg in the solution precipitates and the Zn species determine the growth rate. The minimum growth rate observed for the 10 mol% Mg solution can arise from the dependence of the growth rate on the film texture, which is in turn influenced by the adsorption of charged species as we will see later.

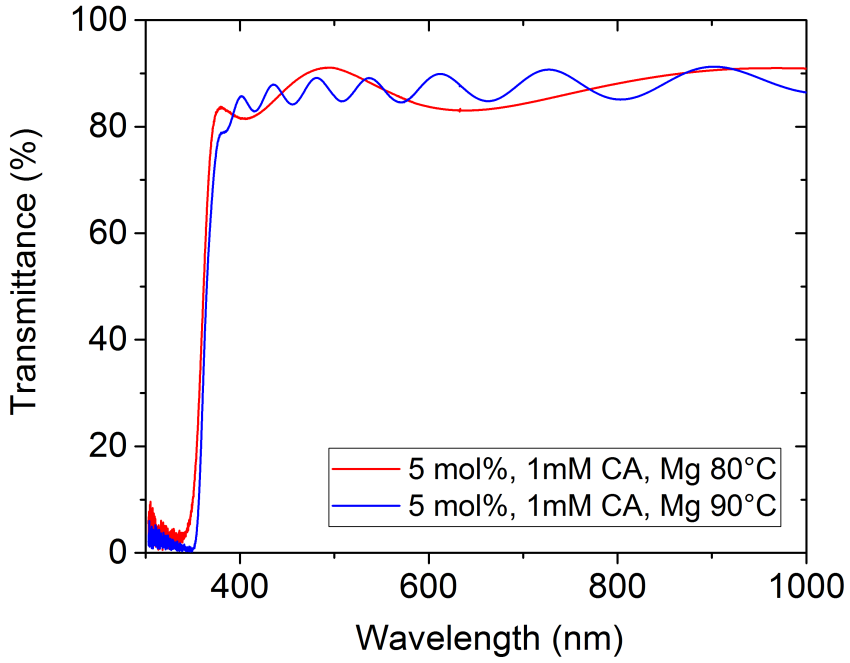

Figure 6.10: Transmittance spectra of films deposited from 5 mol% Mg solution at pH = 9.1 and a temperature of 80°C or 90°C

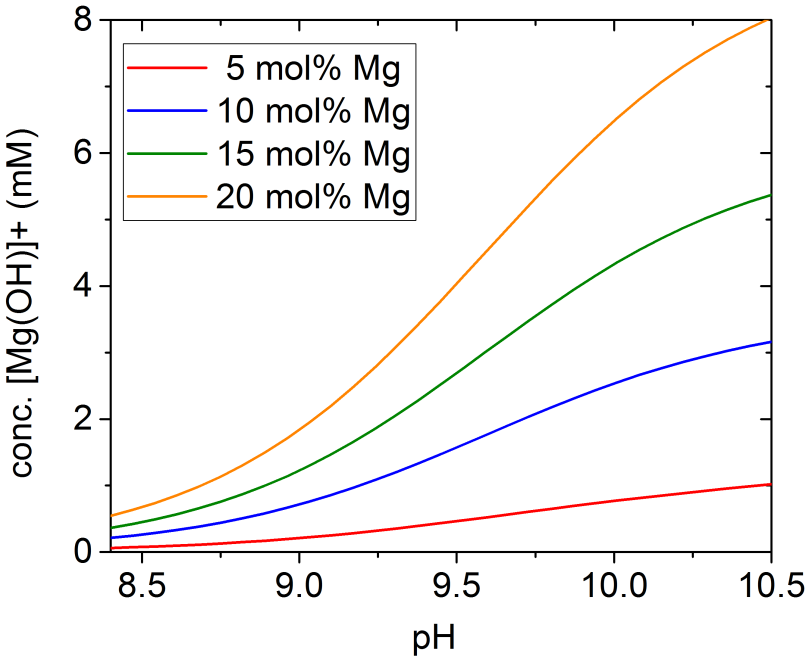

Figure 6.11: Amount of $[Mg(OH)]^+$ species between pH 8.5 - 10.5 in different deposition solutions

In order to prevent precipitation in the solution, someone may argue that the amount of citric acid as a complexant for Mg should be increased to higher levels. To test this, we have conducted experiments where the 10 mol% Mg solution was used and the citric acid concentration was increased to 4.5 mM. In this case no growth or only very slow growth of ZnO was achieved, while the reaction solution was completely clear, indicating that no homogeneous precipitation occurred . This low level of supersaturation leads to a smaller driving force for the ZnO deposition, hence fast ZnO growth cannot happen. In contrary to that, with 3 mM citric acid and 10 mol% Mg in the solution a thin film of 190 nm was deposited.

6.2.1 Morphology

The film morphology is strongly influenced by numerous parameters in the chemical bath solution. These include the temperature, the level of supersaturation and the nature of the substrate. Chemical speciation in the solution also influences the film morphology distinctively. The speciation is dependent on pH, metal counter-ion, complexing agents and other additives. Besides that, face-selective electrostatic adsorption of various Mg and Zn species can determine a certain morphology of the ZnO film. In section 6.1 it was illustrated that for undoped ZnO films deposited at various pH values or temperatures, no change in morphology was observed. In the case of ZnMgO films, drastic changes in film morphology in dependence of the Mg concentration in the solution, were observed, as will be seen later. Since the temperature and chemical reagents were the same for ZnO and ZnMgO deposition, this behaviour can be attributed to the various Mg species present in the solution, excluding other effects. It was further seen that the pH has a strong influence on ZnMgO film morphology.

The film morphology was studied via SEM and XRD analysis. The effects of the Mg molar concentration and the solution pH, are discussed in detail in the following sections.

6.2.1.1 Influence of Mg concentration

The Mg concentration in the solution has the most drastic influence on the film morphology. In order to exclude other effects in our investigation, the ammonia and citric acid concentration were fixed in the experiments to the values of 0.7 M and 1 mM, respectively. The resulting solution pH at 80°C was 9.1 +/- 0.05. The SEM pictures in Figure 6.12 clearly show different film morphologies as a function of the Mg concentration, suggesting that different ZnO surface planes are exposed to the solution. Also, the deposited film thickness, extracted from the cross section images, varies largely (Figure 6.12).

The XRD analysis of these samples confirmed that each solution composition gives rise to a specific film texture, as shown in Figure 6.13. If the solution does not contain magnesium, the (002) texture of ZnO is dominant, while with 5 mol% Mg the (100)

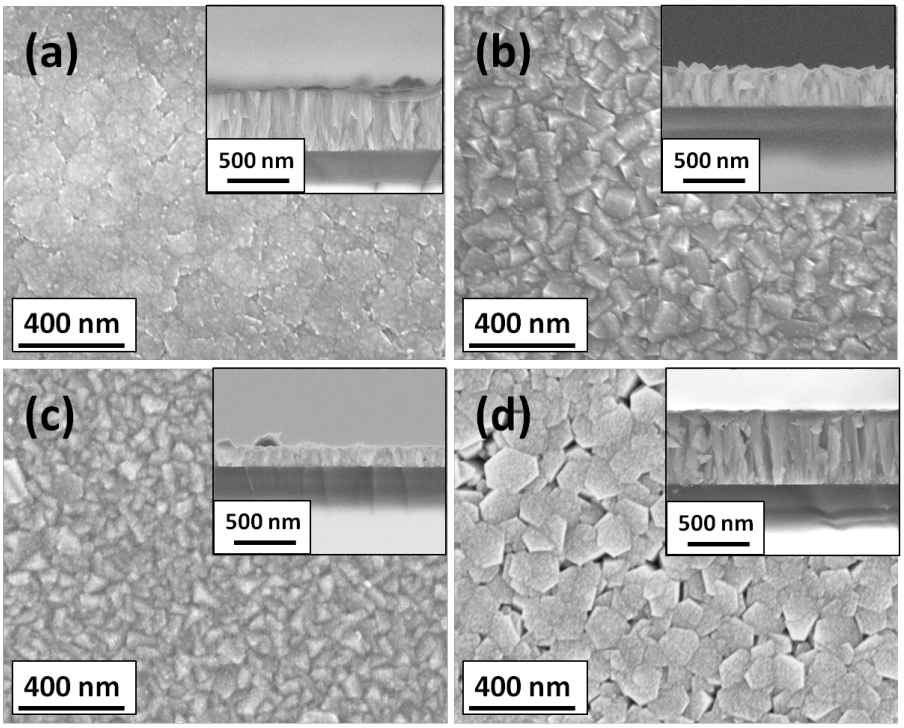

Figure 6.12: SEM pictures of ZnO thin films deposited at pH 9.1 with different Mg concentrations (a) only ZnO, (b) 5 mol% Mg, (c) 10 mol% Mg, (d) 15 mol% Mg

and (110) reflections are dominant. If 10 mol% Mg was added, the main peak stems from the (101) planes, while with concentrations > 15 mol% Mg, the (002) texture was again obtained.

It was previously seen that the deposition of undoped ZnO led to a (002) texture, due to the adsorption of Cit^{3-} onto the positve-charged (002) plane. In the following the origin of certain ZnO surface charges are explained, because this knowledge is essential to understand the occurance of distinct ZnMgO film morphologies.

The surface charge of ZnO faces in contact with an aqueous solution is determined by the pH value. At low pH, H^+ can be adsorbed onto the surface resulting in positive charge, while at high pH, H^+ ions are expelled, causing a negatively-charged surface. If solutions contain metal complexes, these species can also adsorb onto certain ZnO faces. To determine whether the surface exhibits mainly a positive or negative charge, the isoelectric point (IEP) defines the pH at which the surface charge passes from positive to negative. For ZnO powders the IEP point was estimated in the literature to be at pH 9.5 [128]. Other literature values range from 8.7 - 10.3 [129]. Since the experiments in this thesis were carried out at a pH < 9.5 it can be assumed, that the polar planes (e.g. (002)) are positively charged.

The charges of certain ZnO crystal planes were measured by [130], using atomic-force microscopy with a functionalized probe attached to the cantilever. It was found that the (002) facet was mainly positively charged, while the nonpolar (100) and oxygen-terminated planes were negatively charged. Since the polar pyramidal-shaped (101)

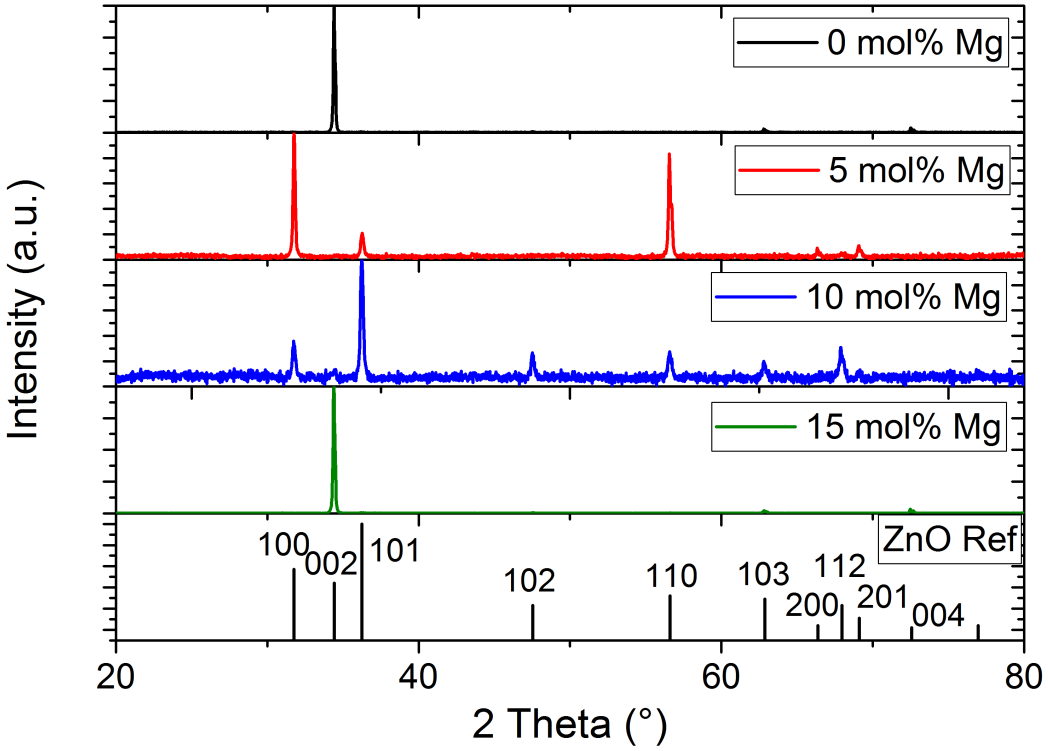

Figure 6.13: XRD spectra of Mg doped ZnO films with different Mg content in the deposition solutions at pH = 9.1

plane is oxygen-terminated [131], this surface is therefore negatively-charged. Figure 6.14 shows the (101) and (100) ZnO planes with their respective surface charge.

There are two main reasons leading to specific surface morphologies in ZnO deposition from Mg-containing solutions. Since Mg forms a complex with the capping agent citric acid, the citrate is completely in the form of $[MgCit]^-$. Compared to the strong adsorbant Cit^{3-}, which contains three acid groups [118], $[MgCit]^-$ only contains one acidic COO^--group, resulting in a less efficient adsorption onto positively charged planes. The second reason is the charge compensation of various Mg species via adsorption onto certain charged ZnO facets.

Depending on the Mg concentration in the solutions, certain amounts of positively and negatively charged Mg species are present and can adsorb onto opposite charged ZnO planes. To investigate which types of Mg species can be found in the solution, speciation diagrams were studied (see also Figure 5.8). Relevant Mg species for these experiments are: Mg^{2+}, $[MgCit]^-$ and $[Mg(OH)]^+$. Table 6.1 lists their concentrations for the 4 different solution compositions aforementioned. In the following, the results presented in this table are analyzed in detail.

As mentioned above, citric acid is completely in the form of $[MgCit]^-$ for all Mg-containing solutions. Table 6.1 further shows that the amounts of Mg^{2+} and $[Mg(OH)]^+$

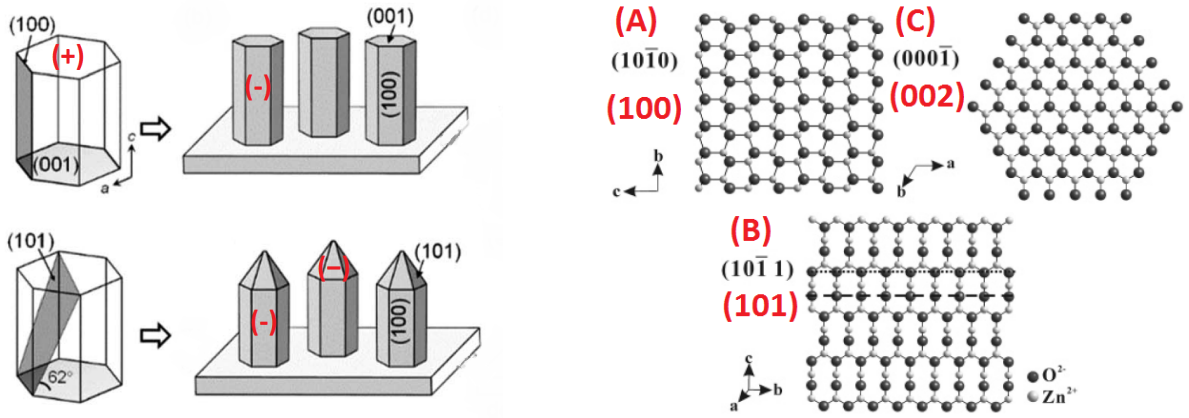

(a)(100) and (101) ZnO (modified from [132])

(b)Atomic structures on different ZnO crystal surfaces (modified from [131])

Figure 6.14: ZnO crystal faces

Table 6.1: Species present in Mg doped ZnO deposition solutions (1 mM citric acid)

Solution	c($[MgOH]^+$) [mM]	c(Mg^{2+}) [mM]	c($[MgCit]^-$) [mM]	c(Cit^{3-}) [mM]
0% Mg	0	0	0	1
5% Mg	0.26	0.76	0.98	0.02
10% Mg	0.99	2.52	0.99	0.01
15% Mg	1.54	4.48	0.98	0.02

increase for the solutions containing more Mg. After careful analysis of many samples deposited from various solutions, a correlation between the preferred ZnO orientation and the relative concentration of the negatively-charged $[MgCit]^-$ to the positive-charged Mg^{2+} and $[Mg(OH)]^+$ species could be drawn. Based on that, three different growth conditions were established (see also Figure 6.15):

(A) c($[MgCit]^-$) > c(Mg^{2+}) or c($[MgOH]^+$)
(B) c(Mg^{2+}) > c($[MgCit]^-$) or c($[MgOH]^+$ and c($[MgCit]^-$) = c($[MgOH]^+$)
(C) c(Mg^{2+}) » c($[MgCit]^-$) or c($[MgOH]^+$)

In the following, growth mechanisms for cases (A), (B) and (C), resulting in different film morphologies, are proposed. The argumentations are mainly based on the charge of different ZnO crystal faces and the electrostatic face-selective adsorption of various Mg species onto these faces. A fundamental investigation about face-selective electrostatic control during ZnO deposition from solutions was done by Joo et. al. [133].

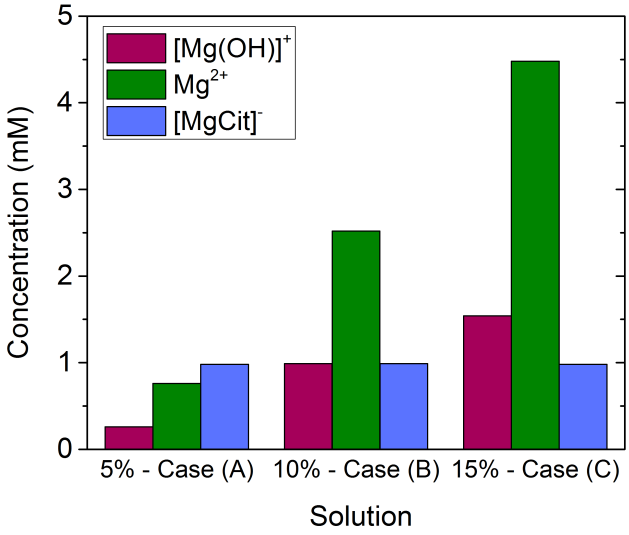

Figure 6.15: Growth mechanism devided in three cases (A), (B) and (C)

Case A: As shown earlier (see Figure 6.13), the deposition from the 5 mol% Mg solution gave rise to a pronounced (100) peak and a weaker (110). Speciation diagrams showed that the majority of the Mg in the solution was complexed by citric acid to form the bulky Mg citrate. Besides that, lower amounts of the positive Mg species are present. As discussed before, the (100) ZnO facet exhibits a negative charge while the (002) ZnO plane is positively charged. Under these assumptions, the negatively charged $[MgCit]^-$ can adsorb onto the positive (002) plane, while $[MgOH]^+$ and Mg^{2+} adsorb mainly onto the negative (100) face. A possible growth mechanism is shown in Figure 6.16.

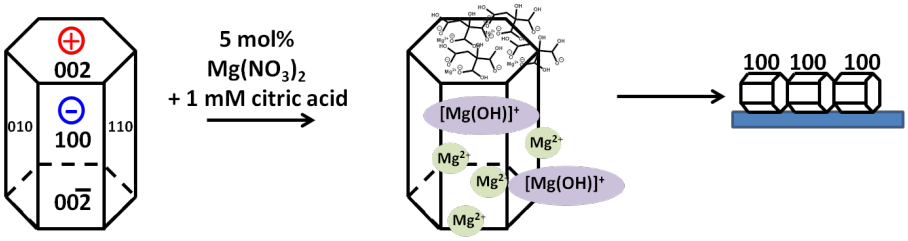

Figure 6.16: Deposition of ZnO according to case (A) exposing the (100) crystal face

Since the non-polar (100) ZnO face is the most stable one [134], it will be finally exposed to the solution. Besides that, stabilization of the least stable (002) ZnO face requires a strong adsorbant, such as Cit^{3-}, for adequate charge compensation.

To strengthen the arguments for the suggested growth scheme of case (A), a higher amount of citric acid (>1 mM) was added into solutions containing 10 and 15 mol% Mg, which previously showed a dominant (101) and (002) texture respectively. The concentrations of the three Mg species in the solutions of these experiments were

calculated from speciation diagrams and are shown in Table 6.2 and Figure 6.17. It can be seen that the amounts of the Mg species are similar to the speciation in the 5 mol% solution and therefore, a similar texture would be expected. SEM picture showed indeed a similar morphology as seen in Figure 6.18.

Table 6.2: Mg species for samples with adjusted citric acid concentration

Solution	c(MgOH+) [mM]	c(Mg2+) [mM]	c(MgCit-) [mM]
5% 1mM CA	0.26	0.76	0.98
5% 2mM CA	0.08	0.16	1.76
10% 3mM CA	0.41	1.17	2.92
15% 2.5mM CA	1.19	3.29	2.52

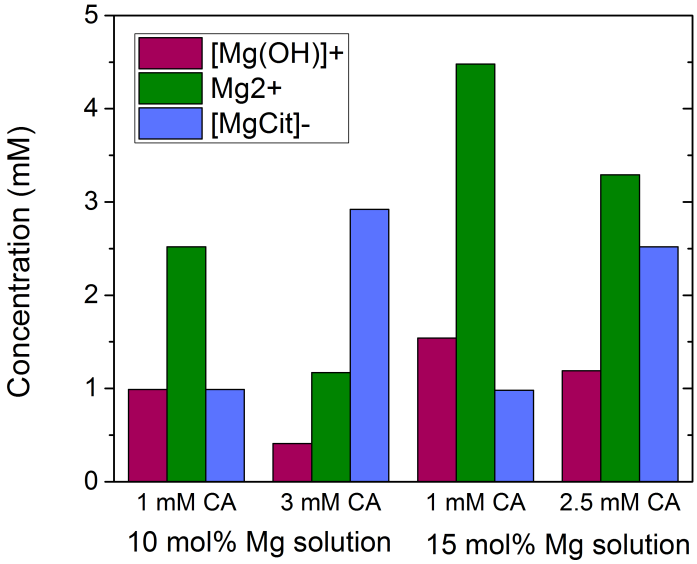

Figure 6.17: Mg species in 10 and 15 mol% Mg solution with higher amounts of citric acid

XRD measurements confirmed, that the samples with increased citric acid concentrations are dominantly (100) ZnO. In comparison to samples from the 5 mol% solution, the XRD peak intensities are similar, as shown in Figure 6.19. All samples exhibit a dominant (100) texture, with minor peaks originating from the (110) and the (101) planes.

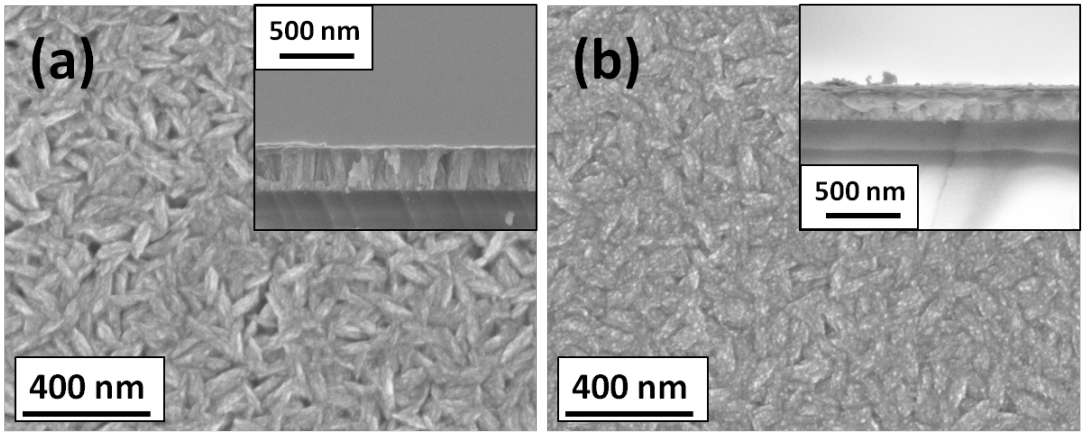

Figure 6.18: SEM pictures for the deposition of ZnMgO films with (a) 10 mol% Mg and 3 mM citric acid, (b) 5 mol% Mg and 2 mM citric acid

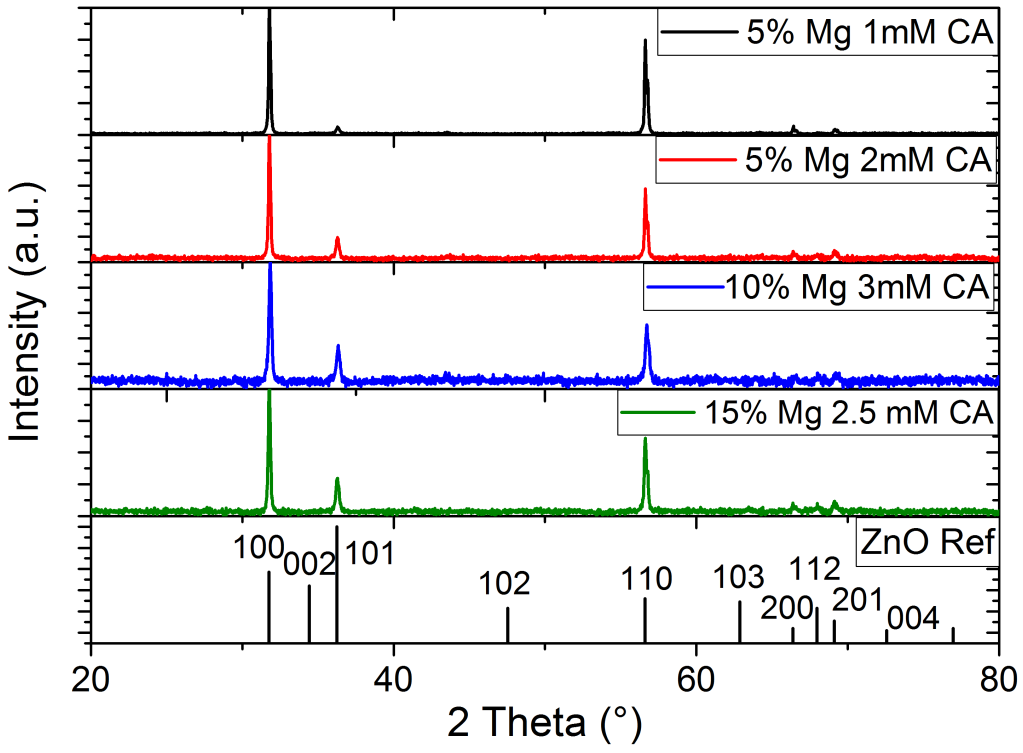

Figure 6.19: XRD spectra of Mg doped ZnO films with adjusted citric acid concentrations

Case (B): For this case the speciation diagrams showed a higher amount of positively-charged ions in the solution. Concentrations of $[MgCit]^-$ and $[MgOH]^+$ were almost equivalent. It is important to note, that a dominant (101) ZnO texture was only observed for solutions containing 10 mol% Mg and 1 mM of citric acid. This suggests that a specific Mg species composition is necessary to achieve this certain morphology. Table 6.3 lists the concentrations of Mg species of samples exhibiting (101) ZnO texture.

Table 6.3: Mg species for samples with 10 mol% Mg 1 mM and predominantly (101) face

Sample	c([MgOH]+) [mM]	c(Mg2+) [mM]	c([MgCit]- [mM])
10% pH=9.23	1.125	2.385	0.99
10% pH=9.16	0.99	2.52	0.99
10% pH=9.05	0.72	2.79	0.99

The higher amount of $[MgOH]^+$ (as precursor for $Mg(OH)_2$) gave rise to increased precipitation in the solution. The strong precipitation might also cause $[MgCit]^-$ to loose the Mg ion in the form of $Mg(OH)_2$, because the stability of Mg citrate is rather low. Therefore, a small amount of Cit^{3-} can be expected in the solution resulting in adsorption onto the (002) ZnO plane. The high concentration of Mg^{2+} ions can adsorb on both the (100) and (101) faces, and stabilize them. Considering this, a growth scheme for the pyrimidal (101) dominated ZnO film morphology is proposed and can be seen in Figure 6.20.

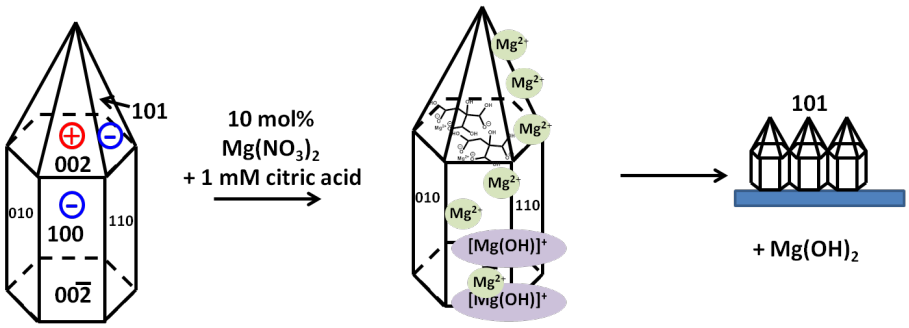

Figure 6.20: Deposition of ZnO according to case (B) exposing the 101 crystal face

The oxygen-terminated (101) surface plane is non-polar and rather unstable without charge compensation through adsorption. A possible scenario is, that through this simultanous adsorption onto various planes, it is energetically most favorable to expose the (101) face to the solution. Another reason might be a certain reconstruction leading to a (101) morphology. Both explanation are plausible and supported by the low film growth rate observed during thes depositions. High adsorption of many complexes might cause steric hindrance for incoming species and slow down the ZnO growth.

To investigate mechanism (B) further, XRD spectra were analyzed (see also Figure 6.21). It can be seen that when the $[MgOH]^+$ concentration is highest (top graph), both (100) and (101) faces are exposed to the solution to the same extent. A higher amount of

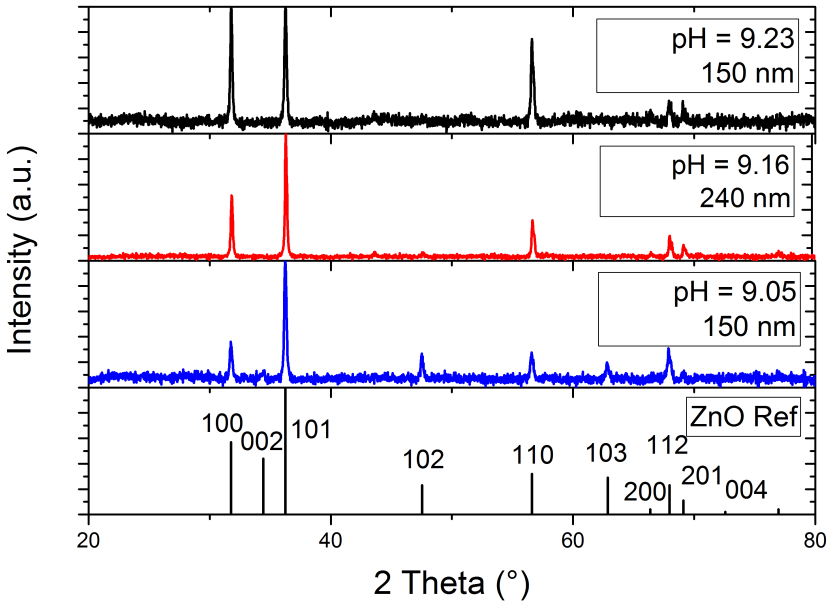

Figure 6.21: XRD spectra of Mg doped ZnO films with predominantly (101) ZnO face

positive Mg species can cause a higher adsorption onto both negatively-charged (100) and (101) faces. To make a definite statement what causes the preference of either (100) or (101) ZnO, more depositions of ZnMgO films from solutions with various compositions and XRD analysis have to be realized.

Case C: In the solutions according to case (C) the concentration of Mg^{2+} ions is the highest among all Mg species. Further, the amount of $[MgOH]^{+}$ is rather high, which results in a high amount of $Mg(OH)_2$ precipitation in the solution. Experimentally it was seen that solutions containing a Mg concentration > 15 mol% were completely "milky" at 80°C. As mentioned before, it is very likely that a rather high amount of Cit^{3-} is present in the solution, because of the low stability of the $[MgCit]^{-}$ complex. The strong adsorbant Cit^{3-} will immediately adsorb onto the positive-charged (002) ZnO plane, causing film growth along this direction. Further, also Mg^{2+} can precipitate in the form of $Mg(OH)_2$, because there is not a high enough amount of complexant in the solution to stabilize the Mg. A reaction scheme according to these explanations can be seen in Figure 6.22.

To strenghten the arguments for mechanism (C) and exclude an influence of $[MgCit]^{-}$, deposition from a solution that usually results in another film morphology was done without citric acid. The 5 mol% Mg solution, which usually exhibts a (100) structure was chosen and at pH=9.2 the solution contained only Mg^{2+} and $[MgOH]^{+}$ Mg species (as seen in table Table 6.4). It was shown by SEM cross sections of the samples (see also Figure 6.23), that nanorods instead of a dense film were deposited. Deposition from a 24 mol% Mg solution with very high concentrations of Mg^{2+} and $[MgOH]^{+}$ also led to the deposition of nanorods. This and the high amounts of precipitates

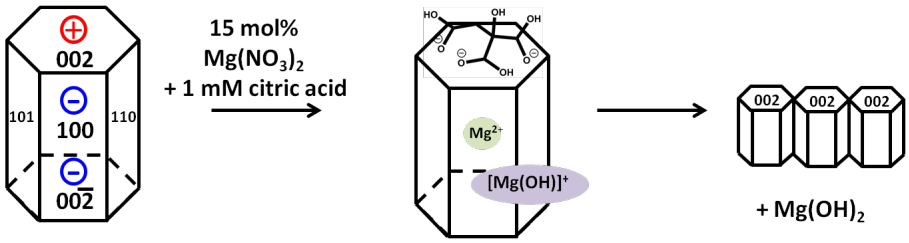

Figure 6.22: Deposition of ZnO according to case (C) exposing the 002 crystal face

in the solution, strengthened the assumptions that Mg^{2+} and $[MgOH]^{+}$ precipitate without a complexant and Cit^{3-} is necessary for a stabilization of the (002) plane. It also shows, that the (002) ZnO plane is positively-charged under our experimental conditions, because otherwise as shown in [133] (pH=11), Mg^{2+} would be able to stabilize a negatively-charged (002) plane.

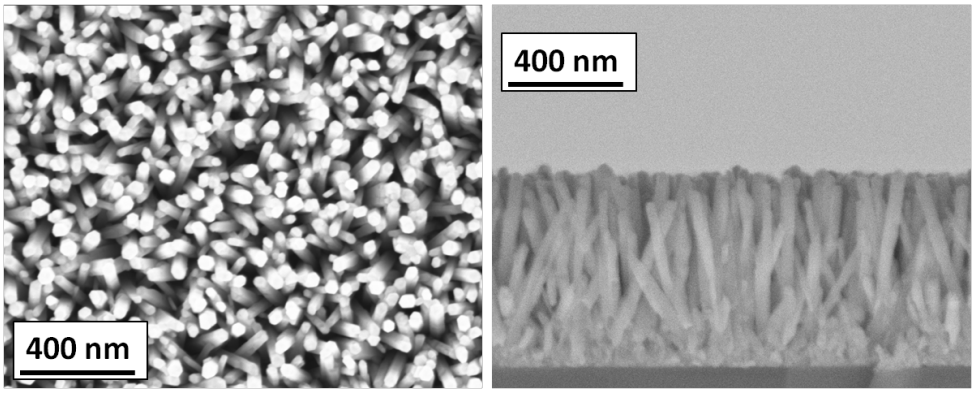

Figure 6.23: SEM pictures of Mg doped ZnO deposition at pH = 9.2 without citric acid

Table 6.4: Mg species for samples with higher amount of Mg^{2+} for explanation of reaction scheme (C)

Sample	c([MgOH]+) [mM]	c(Mg2+) [mM]	c([MgCit]- [mM])
15% Mg 1 mM CA	1.54	4.48	0.98
5% Mg without CA	0.74	1.16	0
24% Mg without CA	2.96	9.64	0

In summary, the addition of Mg in the solution resulted in a (100), (101) or (002) ZnO film texture. Mg caused on the one hand citric acid to complex as $[MgCit]^{-}$, which weakened the acid's strength as capping agent for the stabilization of the (002) ZnO plane. On the other hand, the positively-charged Mg^{2+} and $[MgOH]^{+}$ could adsorb onto the negatively-charged (100) and (101) planes, causing distinct film morphologies. Further, a high amount of Mg in the solution, caused the precipitation of $Mg(OH)_2$. Because of this, Mg might be separated from the $[MgCit]^{-}$ complex and the free Cit^{3-} could adsorb onto the (002) plane for stabilization.

6.2.1.2 Influence of the solution pH

The amount of certain species present in the solution is determined by the pH value. The pH is also the reason for the charging of certain ZnO faces in solution. Therefore all discussed theories in the previous chapter are based on the solutions' pH. Since two important factors that influence the ZnO film morphology, namely the level of $Zn(OH)_2$ supersaturation and the growth rate are also pH dependent, the pH influence on its own is very difficult to investigate. Neglecting the level of supersaturation, the morphology of two films of the same thickness (= same growth rate) is compared by XRD in Figure 6.24. It can be seen that at higher pH values the amounts of the (100) and (110) ZnO faces increase. An explanation for this is, that either the pH dependent Mg species distribution causes the different morphology or the (101) ZnO face is in a lower pH environment more stable.

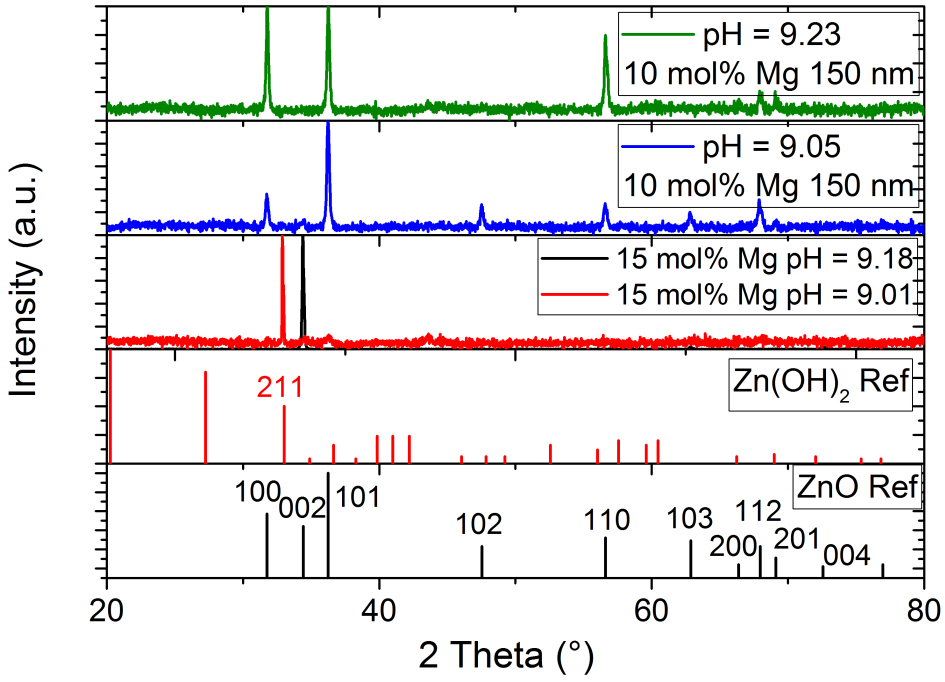

Figure 6.24: XRD spectra of Mg doped ZnO films from 5 and 10 mol% Mg solution with different pH

Deposition from 15 mol% Mg solution at high pH gave rise to a crystalline $Zn(OH)_2$ film instead of ZnO (see XRD spectrum Figure 6.24). It has to be noted that the $Zn(OH)_2$ film was very thin (50 nm). $Zn(OH)_2$ was not detected by XRD in any other samples. This suggests that under certain pH and solution species conditions (pH = 9.2) deposition of $Zn(OH)_2$ is favored over ZnO. In all other solution conditions $Zn(OH)_2$ was either directly dehydrated to ZnO or always present as amorphous $Zn(OH)_2$.

6.2.2 Mg Incorporation Into ZnO Lattice

The incorporation of Mg into the ZnO lattice was one of the main goals within this thesis. Since under equilibrium conditions the solublity of MgO in ZnO is limited to 4 mol% (see also subsection 3.1.1) it was not clear if more incorporation through chemical bath deposition is possible.

To demonstrate Mg incorporation into the ZnO, the optical band gap was calculated from transmittance spectra via Tauc approximation. Furthermore, ICP OES was used to determine the Zn:Mg ratio in the films and calculate the mol% Mg incorporated. In order to see whether phase separation of MgO happens, XRD spectra were measured to confirm the ZnO crystal structure. XRD diffractograms were also used to calculate possible peak shifts caused through incorporation of the slightly smaller Mg atom. The lattice parameters a and c of the hexagonal ZnO were calculated from XRD data.

Since deposition solutions with 5, 10 and 15 mol% Mg were used for the chemical bath deposition, a correlation between the amount of Mg in the solution and in the resulting film was expected. Experimentally it was shown that, with the citric acid amount remaining constant (1 mM), the 5 mol% Mg solution had the highest incorporation of Mg in the film. A further increase of Mg content in the solution led to a decrease of Mg content in the film. Transmittance spectra indicated a clear band edge shift between films exhibiting the highest and lowest Mg content in the film, as seen in Figure 6.25. Table 6.5 shows calculated band gaps through Tauc's plot approximation as well as the amount of Mg in the film confirmed via ICP OES.

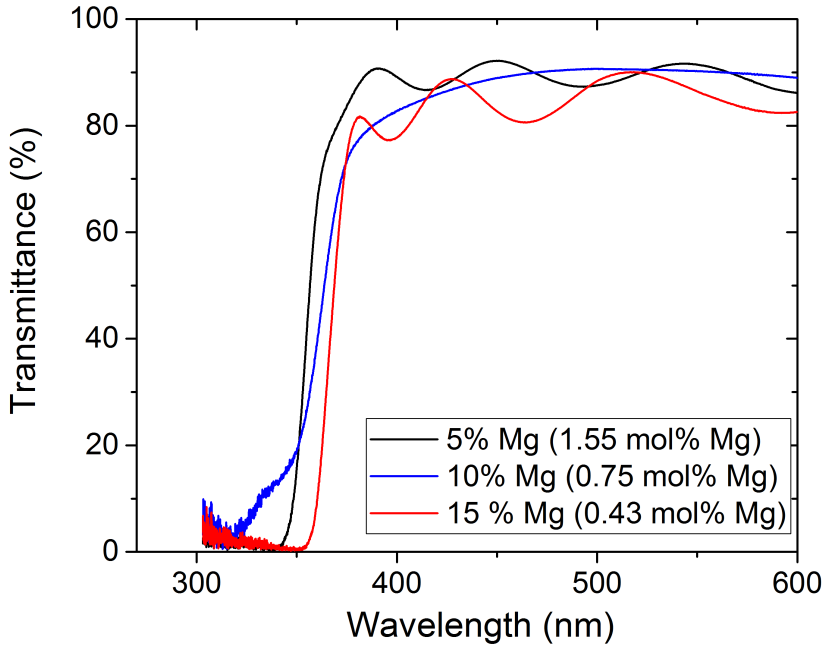

Figure 6.25: Transmittance spectra of 5, 10 and 15 mol% Mg (+ 1 mM citric acid) solutions

Table 6.5: Band gap and Mg content of 5, 10 and 15 mol% Mg solutions samples

mol% Mg (in solution)	thickness [nm]	Band gap [eV]	mol% Mg in film (ICP OES)
5	610	3.5350	1.55
10	150	3.4054	0.75
15	540	3.4277	0.41

In order to explain these results, the influence of the growth mechanism on the Mg incorporation was examined precisely. In the previous chapter three different growth mechanisms depending on the amount of Mg in the solution were proposed subsubsection 6.2.1.1. XRD measurements of 5 mol% Mg solution samples displayed mainly a (100) ZnO morphology, while samples from 10 mol% Mg solution exhibit (101) ZnO and 15 mol% Mg solution samples grew dominantly along (002) ZnO (see also Figure 6.13). In connection with the Mg content in the film, a (100) morphology led to the highest incorporation of Mg, while (101) ZnO showed a lower incorporation of Mg. The lowest Mg incorporation was seen when ZnO grew along (002). None of the samples displayed an evidence of a MgO phase, suggesting that the film composition lies within the solubility range of MgO in ZnO.

To strengthen the argument that Mg incorporation depends on the ZnO crystal orientation, the Mg content of samples with inreased citric acid concentrations, deposited from 10 and 15 mol% solutions, were measured. This samples also showed dominantly a (100) ZnO face as shown in Figure 6.19. It was found that these samples incorporated the highest amounts of magnesium. Table Table 6.6 displays the amount of Mg measured via ICP OES and the calculated optical band gaps from transmittance spectra. The bold highlighted samples are the ones with higher citric acid concentration and therefore more Mg incorporated as well as preferred (100) ZnO crystal orientation.

Table 6.6: Highest amounts of Mg incorporated

mol% Mg (solution)	Citric Acid [mM]	thickness [nm]	Bandgap [eV]	mol% Mg (ICP OES)	dominant ZnO crystal orientation
5	1	610	3.535	1.55	(100)
5	0.5	335	3.4798	0.88	(100) + (110)
5	2	344	3.4908	0.80	(100)
10	**3**	190	**3.5488**	**2.10**	(100)
10	1	150	3.4054	0.75	(101)
15	**2.50**	197	**3.4975**	**1.16**	(100)
15	1	540	3.4277	0.41	(002)

These results suggest that a high amount of Mg citrate (see deposition mechanism (A) in subsubsection 6.2.1.1) causes incorporation of Mg. Citric acid on the one hand keeps the Mg complexed in the solution. On the other hand $MgCit^-$ might adsorb onto the positive-polarized (002) plane of ZnO. The high amount of incorporated Mg most

likely arises from the high amount of adsorbants, because also Mg^{2+} and $[Mg(OH)]^{+}$ adsorb onto the negatively charged (100), (110) or (101) plane. In order to increase the amount of possible adsorbants for ZnO, experiments with an increased citric acid and Mg concentration were performed. It was seen that if a certain amount of Mg citrate is exceeded, no film or only a very thin film was deposited. An explanation for this is, that for high adsorption levels of the bulky citrate incoming species are blocked, leading to a decrease in film growth rate.

Previously it was shown that certain pH and Mg species conditions, can cause the deposition of a thin $Zn(OH)_2$ film. Surprisingly these films exhibited the highest amount of Mg (4.12 mol% in a 50 nm film). The cause of this is not clear, but will be investigated further.

Table 6.6 also shows that for the thin sample (150 nm) the band gap calculation was not accordance with the other results (highlighted in red). Reasons for this are, that the lower wavelength region in transmittance spectra of thin samples, can not be taken for Tauc's approximation as in thicker films. Therefore band gaps only for films with a thickness higher than 190 nm were calculated. To confirm the amount of Mg in the films ICP OES was measured. The band gap dependence on the measured Mg amount in the films is demonstrated in Figure 6.26. As expected, the band gap increases almost linearly with Mg content. These findings are first indicators of a successful incorporation of Mg into the ZnO lattice. Transmittance spectra and Tauc's plots of four samples can be seen in Figure 6.27.

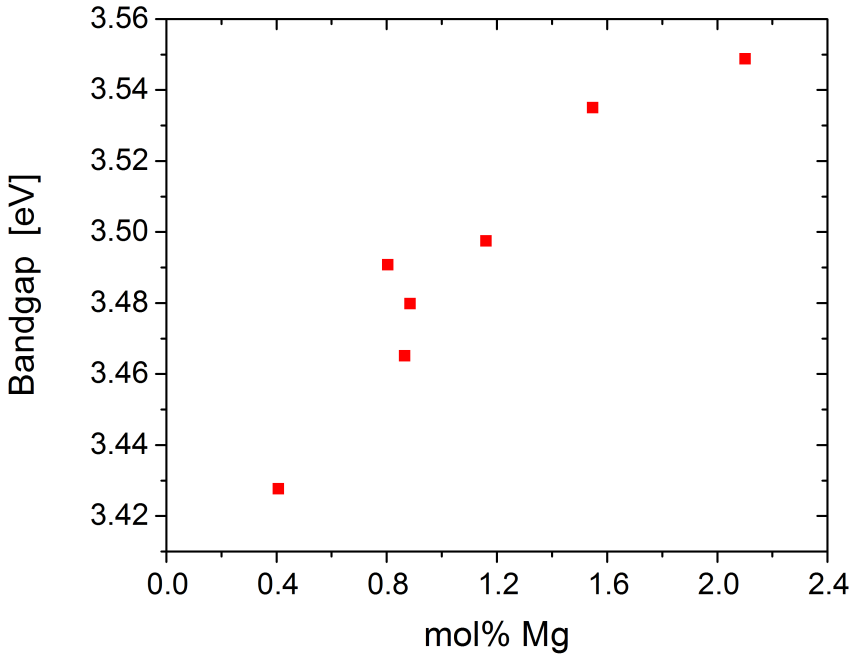

Figure 6.26: Increase of band gap with Mg content in the film confirmed by ICP OES

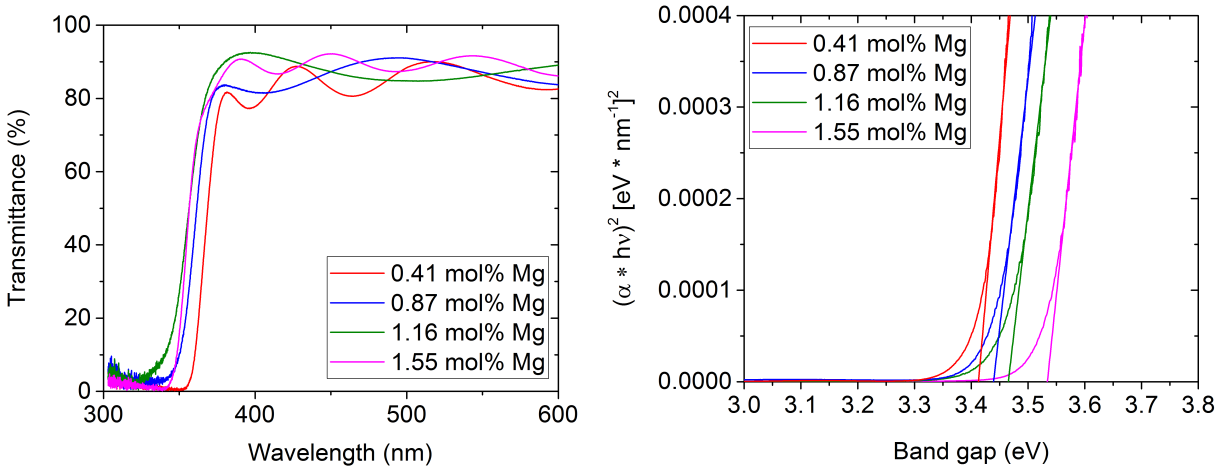

Figure 6.27: Transmittance spectrum and Tauc's plot from ICP measured Mg doped ZnO samples

To prove whether Mg is indeed incorporated, XRD spectra were studied. The tetrahedral ionic radius of Mg is with 0.57 Å[40] smaller than that of Zn with 0.60 Å[40]. Thus Mg incorporation causes a lattice shrinkage. Because of Bragg's law for constructive interference (see Equation 4.3) a lattice shrinkage shifts the XRD diffraction peaks to higher 2Θ angles. The shift of (100) and (101) peaks for samples containing the highest amounts of incorporated Mg, can be seen in Figure 6.28. The largest shift to higher angles can be seen for the highest amount of Mg (2.1 mol%) detected by ICP OES. This sample was deposited from 10 mol% solution with increased citric acid concentration of 3 mM.

The 2Θ angles in dependence of the Mg content for the (100) and (101) peaks can be seen in Figure 6.29. Lattice constant a was calculated from the (100) plane, while c was determined from the (101) ZnO plane. As reference, the lattice constants for undoped ZnO were calculated from the (002) and (101) peaks.

Calculated lattice constants for a few samples are listed in Table 6.7. Lattice constants for the hexagonal lattice were calculated with follwing equation, in which hkl refers to the Miller indices of the crystal planes:

$$\frac{1}{d^2} = \frac{4}{3}\left(\frac{h^2 + hk + k^2}{a^2}\right) + \frac{l^2}{c^2} \tag{6.1}$$

From Table 6.7 and Figure 6.30 it can be seen that the lattice paramters a and c decrease with higher Mg content in the deposited films. Altough especially for lattice paramter a the decrease is very small. This fits to results of [3] (PLD deposition) who reported a decrease in lattice paramter c. In the same publication lattice paramter a increased with higher Mg content, but for Mg contents < 10% lattice paramter a remains about the same. For MBE deposited Mg doped ZnO films, a decrease in lattice paramter c and a constant parameter a with increasing Mg content, was reported [43]. This fits well to the calculated lattice paramters within this experimental work.

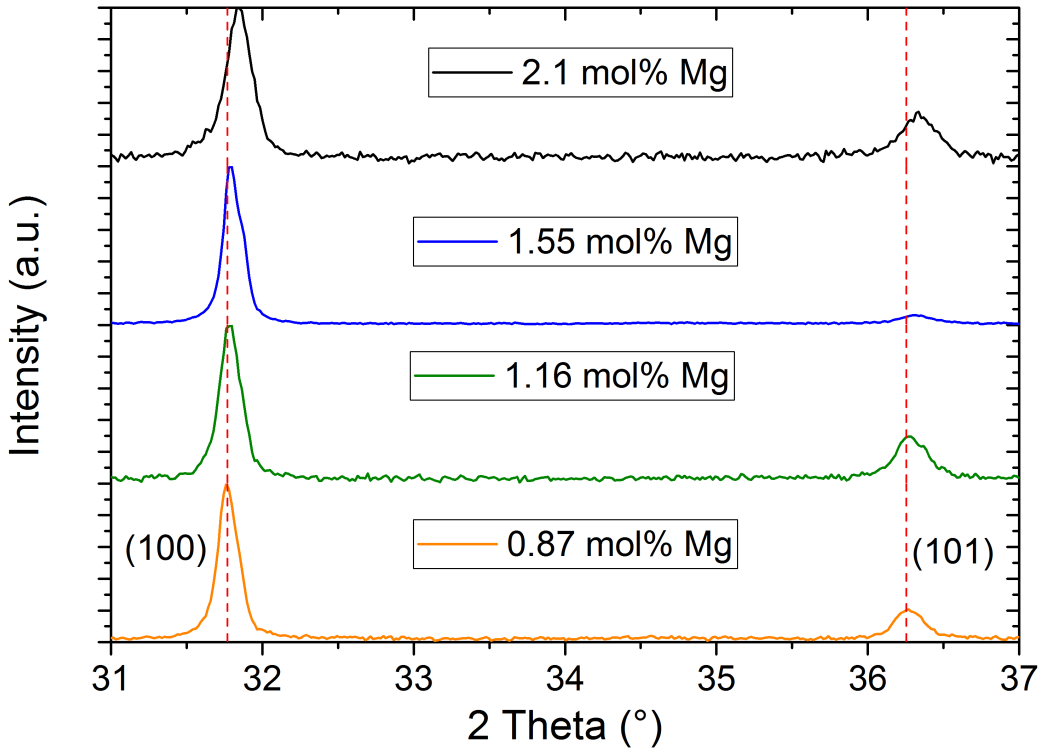

Figure 6.28: (100) and (101) ZnO peak shifts with different amount of Mg incorporated

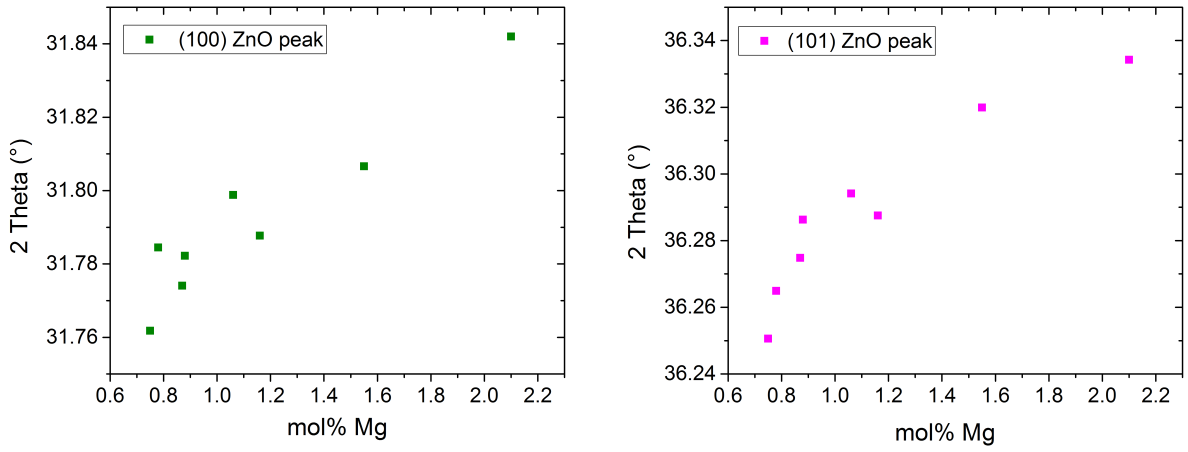

Figure 6.29: 2Θ angles in dependence of the Mg content for the (100) and (101) Mg doped ZnO peaks

Table 6.7: Calculated lattice constants of Mg doped ZnO samples

mol% Mg in solution	Citric Acid [mM]	mol% Mg (ICP OES)	2Θ (100)	a	2Θ (101)	c
0				3.2485	36.268	5.2050
5	0.5	0.88	31.782	3.2485	36.286	5.1942
5	1	1.55	31.807	3.2460	36.320	5.1869
5 (lower pH)	1	0.87	31.774	3.2493	36.275	5.1968
5	2	1.06	31.799	3.2468	36.294	5.1984
5	4	0.63	31.806	3.2461	36.290	5.2049
10	1	0.78	31.785	3.2482	36.265	5.2085
10 (lower pH)	1	0.75	31.762	3.2505	36.251	5.2049
10	3	2.10	31.842	3.2425	36.334	5.1974
15	2.5	1.16	31.788	3.2479	36.288	5.1964

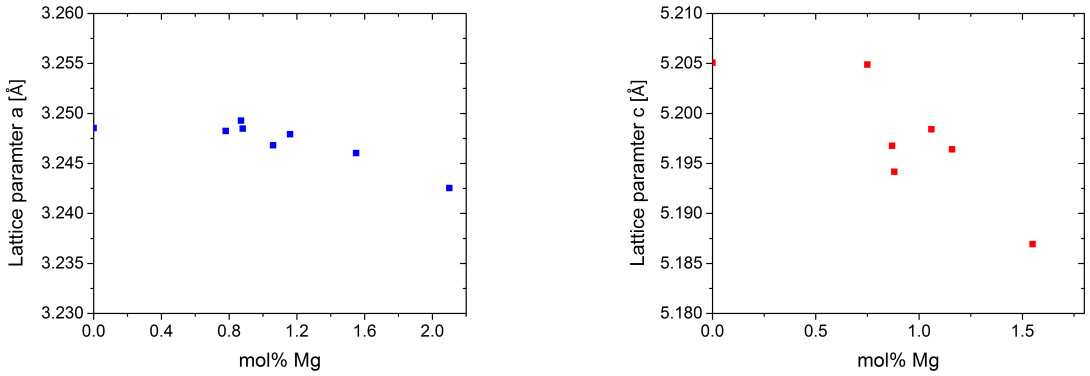

Figure 6.30: Lattice constants a and c in dependence of the Mg content for Mg doped ZnO films

In summary, a band edge shift was seen from transmittance spectra and calculated band gaps were as high as 3.54 eV. XRD diffraction patterns showed peak shifts to higher 2Θ with increasing Mg content in the films, determined via ICP OES. Because of this, Mg incorporation via chemcial bath deposition process is considered sucessful to a certain extent. The highest amount incorporated Mg was 2.1 mol%. These findings suggest that, because of the solubility limit of 4 mol% of MgO in ZnO under equilibrium conditions, it is difficult to incorporate much higher amounts of Mg. Only for the deposition of a thin $Zn(OH)_2$ film showed 4.12 mol% Mg present in the film

Further it is proposed that the growth mechanism with the resulting ZnO crystal orientation influences the Mg incorporation. It was shown that films exhibiting mainly (100) ZnO, incorporated the highest amounts of Mg. Altough proof for this was only found experimentally. Further investigations are necessary to confirm this correlation.

6.3 Applications of thin Mg doped ZnO films in a photovoltaic device

To demonstrate that the CBD deposited ZnMgO films are applicable in thin film photovoltaics, a model solar cell was fabricated and tested. The used device structure is displayed in Figure 6.31.

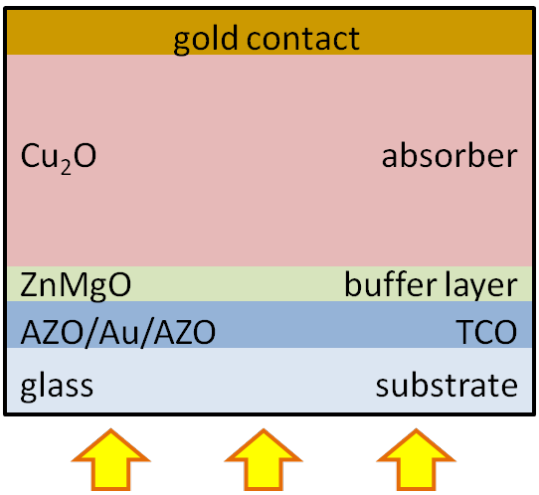

Figure 6.31: Device structure of fabricated model solar cell

As electrode, 50 nm AZO, 7.5 nm Au and 50 nm AZO were sputtered onto a glass substrate. A thin layer of Au was necessary to achieve a conductivity that is high enough for the electrodeposition of an absorber layer. The ZnMgO layers (20 - 130 nm) were deposited from a 5 mol% Mg solution directly onto the AZO layer by chemical bath deposition method at 80°C. SEM pictures of the films are displayed in Figure 6.32.

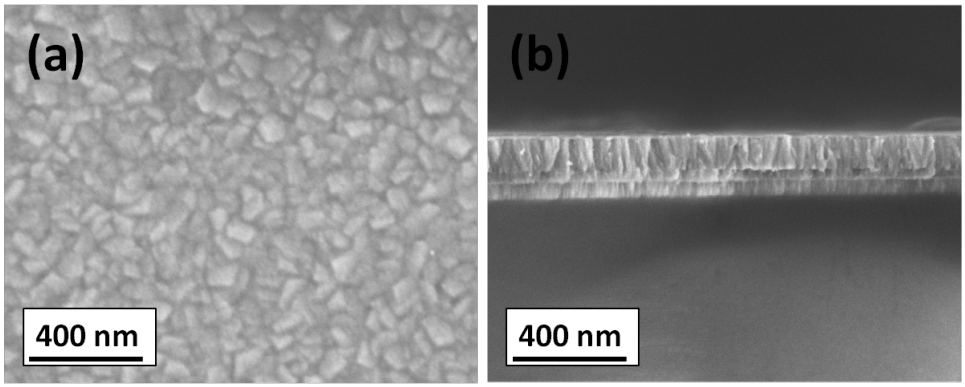

Figure 6.32: SEM pictures 113 nm ZnMgO on AZO/Au/AZO as buffer layer for a Cu_2O solar cell

As absorber layer about 2.5 μ Cu_2O were electrodeposited at the constant voltage of around - 0.6 V onto the ZnMgO buffer. The recipe for the electrodeposition was taken from [135]. As a top-contact layer 100 nm of Au was sputtered on the absorber. Images

of the entire solar cell can be seen in Figure 6.33. In order to test the functionality of the solar cell an IV-measurements were performed. Results are displayed in **??**.

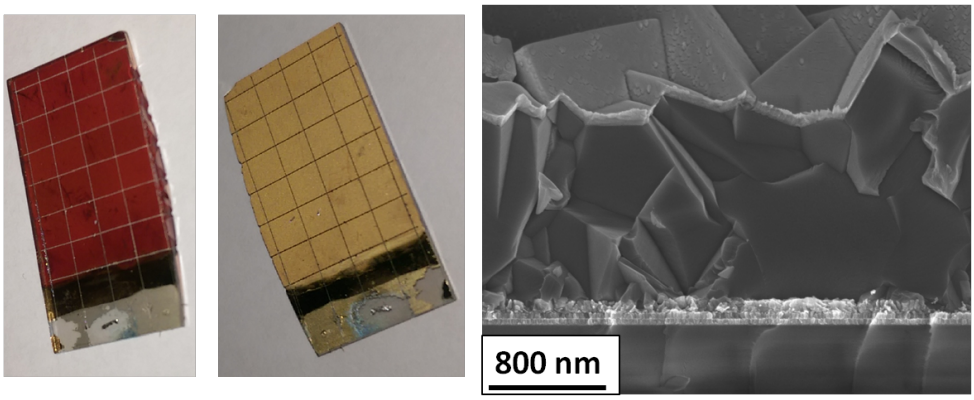

Figure 6.33: Cu_2O solar cell

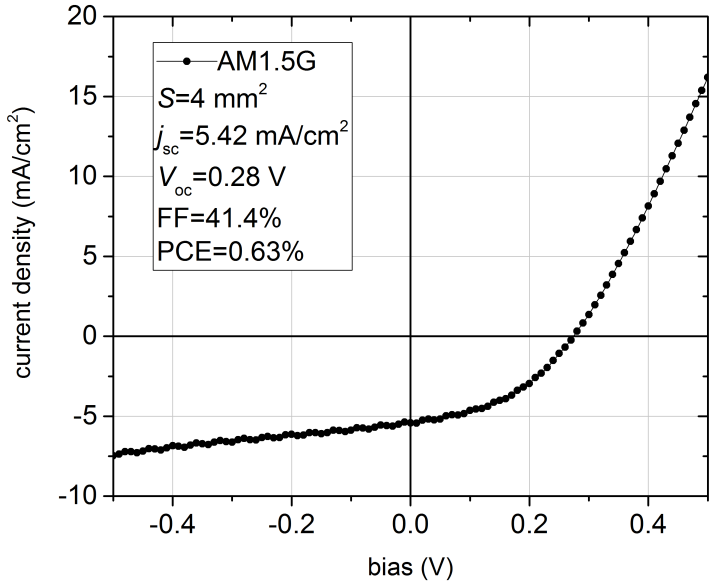

Figure 6.34: IV-curve of fabricated Cu_2O solar cell

7 Conclusion and Outlook

Within this thesis ZnO and ZnMgO thin films were deposited onto ZnO seeded glass substrates via chemical bath deposition. A solution chemistry including ammonium hydroxide, citric acid, Zn and Mg nitrates was employed. The solution chemistry was theoretically investigated via speciation modelling and a systematic experimental investigation followed, varying the concentrations of the chemical reagents and the bath temperature.

It was shown, that ZnO deposition is only possible in a narrow pH window (8.4 - 9.7) due to the pH and temperature-dependent supersaturation of $Zn(OH)_2$ as precursor for ZnO. The supersaturation was controlled by the stability of the $[Zn(NH_3)_4]^{2+}$ complex. In ZnMgO film deposition this pH window was even narrower and shifted simultaneously to lower pH values with increasing Mg content in the solution. This lower driving force for film growth arises from the presence of the additional Mg species in the solution, which are positively- and negatively-charged. Further, the essential role of citric acid to obtain compact film growth was demonstrated, whereas the absence of citric acid gave rise to nanorod arrays in every case.

The film morphology is an important property for many applications. Via X-Ray diffraction measurements a distinct (002) ZnO texture for undoped ZnO films was shown. In contrary to that, ZnMgO films exhibited (100), (101) or (002) textures, depending on the solution composition . Different growth mechanisms, depending on the amount of Mg species in the solution (Mg^{2+}, $[Mg(OH)]^{+}$, $[MgCit]^{-}$) were proposed to explain the appearance of different textures.

In order for ZnMgO buffer layers to match band edges of various thin film absorbers, the band gap of deposited ZnMgO films was an important characteristic. The optical band gap of the CBD deposited ZnMgO films varied in the range of 3.43 up to 3.55 eV. Optical emission spectroscopy measurements showed that the highest Mg incorporation in the film was 2.1 mol%. This finding suggests that due to the solubility limit of MgO in ZnO of 4 mol%, under equilibrium conditions, it is not possible to incorporate higher amounts of Mg into the ZnO lattice. The incorporation of the slightly smaller Mg atom was demonstrated by the shift of the XRD peak to higher 2Θ angles caused by the shrinkage of the lattice. A possible dependence of the Mg incorporation on the adsorption of Mg species onto particular ZnO faces was proposed.

To show the potential of the deposited ZnMgO films as buffer layer, Cu_2O/ZnMgO heterojunction solar cells were fabricated and tested. Although the cells require further optimization, especially concerning the heterojunction interface, a rectifying junction was obtained, giving rise to measurable PV performance under solar illumination.

For the successful use of chemical bath deposited ZnMgO as buffer layers in various types of thin film solar cells, many film properties have to be optimized. The fabrication of a test solar cell containing a chemical bath deposited ZnMgO buffer layer demonstrated that many film properties have to be optimized to achieve state-of-the-art lab cell efficiencies. There are many reasons for that, such as a high amount of defects in the film, too low band gap or transparency. Possible defects can be avoided by subsequent annealing procedures. The main goal for a further film optimization is the achievement of higher Mg incorporation that results in higher band gaps. It was shown that Mg citrate plays a key role in the Mg incorporation process. An optimized solution composition (Mg:citric acid = 1:2) in combination with higher deposition temperatures, to obtain a stronger driving force for growth, might result in higher Mg content in ZnMgO films. Besides already used complexants, the influence of ethylendiamine which selectively adsorbs onto (101) ZnO [118] as well as a complexant of Mg that selectively adsorbs onto (100) ZnO, would give more insights on the Mg incorporation mechanism.

A high potential of the deposited ZnMgO films, lies in the control over the film morphology through the solution composition. This behaviour is especially interesting as a trigger for growth along a certain crystal orientation of a subsequently grown absorber layer. Advantages of this are that the interface between buffer and absorber layer can be optimized, as well as the deposition of distinct absorber morphologies that are known for high cell efficiencies can be promoted.

Besides thin film photovoltaics, another area of interest are sensors. Especially in biosensing a cheap and non-toxic material that exhibits a distinct morphology of a certain crystal face is desired for a face-selective adsorption of molecules. ZnO has been proven an interesting candidate because of strong adsorption onto certain ZnO crystal faces.

Evenif a higher incorporation of Mg through chemical bath deposition would not be possible , we can still use much of the know-how acquired in this thesis concerning the solution chemistry and applying it to other solution-based methods. For example the SILAR method is considering the solution chemistry very similar to chemical bath deposition with the advantage of Zn and Mg species being in separate solutions. If the temperature is the main difficulty to overcome the solubility limit for Mg incorporation in CBD, spray pyrolysis is proposed as an alternative method.

It can been seen that ZnMgO offers many areas of interest for further experimental work. Since the used material is low-cost, earth-abundant and non-toxic with a variable band gap via the Mg content, most likely the research on solution-processed films will be intensified in the future. This thesis hopefully helped to understand some problems and challenges for depositing ZnMgO films from the solution and can be used as a guideline for further investigations.

Bibliography

[1] T. Negami, T. Aoyagi, T. Satoh, S. ichi Shimakawa, S. Hayashi, and Y. Haskimoto, "Cd free CIGS solar cells fabricated by dry processes," in *Photovoltaic Specialists Conference, 2002. Conference Record of the Twenty-Ninth IEEE*, pp. 656–659, May 2002.

[2] C. Platzer-Björkman, T. Toerndahl, A. Hultqvist, J. Kessler, and M. Edoff, "Optimization of ALD-(Zn,Mg)O buffer layers and (Zn,Mg)O/Cu(In,Ga)Se2 interfaces for thin film solar cells," *Thin Solid Films*, vol. 515, no. 15, pp. 6024 – 6027, 2007.

[3] A. Ohtomo, M. Kawasaki, T. Koida, K. Masubuchi, H. Koinuma, Y. Sakurai, Y. Yoshida, T. Yasuda, and Y. Segawa, "MgxZn1-xO as a II-VI widegap semiconductor alloy," *Applied Physics Letters*, vol. 72, no. 19, pp. 2466–2468, 1998.

[4] E. R. SEGNIT and A. E. HOLLAND, "The System MgO-ZnO-SiO2," *Journal of the American Ceramic Society*, vol. 48, no. 8, pp. 409–413, 1965.

[5] C. of Climate and E. Solution, "Outcomes of the U.N. climate change conference in Paris," tech. rep., Framework Convention on Climate Change (COP 21), December 2015.

[6] S. Europe, "Global Market Outlook for Solar Power 2015-2019," tech. rep., SolarPower Europe (European Photovoltaic Industry Association), 2015.

[7] F. ISE, "Photovoltaics Report, updated: 11 March 2016," tech. rep., Fraunhofer Institute of Solar Energy Systems, ISE, 2016.

[8] S. FRONTIER, "Solar Frontier Achieves World Record Thin-Film Solar Cell Efficiency: 22.3%." http://www.solar-frontier.com/eng/news/2015/C051171.html. Accessed: 2016-04-08.

[9] E. Wesoff, "First Solar Hits Record 22.1% Conversion Efficiency for CdTe Solar Cells." http://www.greentechmedia.com/articles/read/First-Solar-Hits-Record-22.1-Conversion-Efficiency-For-CdTe-Solar-Cell. Accessed: 2016-04-20.

[10] S. Abermann, "Non-vacuum processed next generation thin film photovoltaics: Towards marketable efficiency and production of CZTS based solar cells ," *Solar Energy*, vol. 94, pp. 37 – 70, 2013.

[11] H. P. R.L. Moss, E. Tzimas and J. Kooroshy, "Accessing Rare Metal as Supply-Chain Bottlenecks in Low-Carbon Energy Technologies," tech. rep., European Commission Joint Research Centre, 2011.

[12] J. Godt, F. Scheidig, C. Grosse-Siestrup, V. Esche, P. Brandenburg, A. Reich, and D. A. Groneberg, "The toxicity of cadmium and resulting hazards for human health," *J Occup Med Toxicol*, vol. 1, no. 22, pp. 1–6, 2006.

[13] A. hoc Working Group on defining critical raw materials, "Report on Critical Raw Materials for the EU," tech. rep., European Commision, 2014.

[14] J. B. H. Gordon B. Haxel and G. J. Orris, "Rare Earth Elements - Critical Resources for High Technology," tech. rep., U.S. Geological Survey, 2002.

[15] N. R. E. Laboratory, "Best Research-Cell Efficiencies," tech. rep., National Center of Photovoltaics, 2016.

[16] W. Wang, M. T. Winkler, O. Gunawan, T. Gokmen, T. K. Todorov, Y. Zhu, and D. B. Mitzi, "Device Characteristics of CZTSSe Thin-Film Solar Cells with 12.6Efficiency," *Advanced Energy Materials*, vol. 4, no. 7, 2014. 1301465.

[17] N. Naghavi, D. Abou-Ras, N. Allsop, N. Barreau, S. Bücheler, A. Ennaoui, C.-H. Fischer, C. Guillen, D. Hariskos, J. Herrero, R. Klenk, K. Kushiya, D. Lincot, R. Menner, T. Nakada, C. Platzer-Björkman, S. Spiering, A. Tiwari, and T. Törndahl, "Buffer layers and transparent conducting oxides for chalcopyrite Cu(In,Ga)(S,Se)2 based thin film photovoltaics: present status and current developments," *Progress in Photovoltaics: Research and Applications*, vol. 18, no. 6, pp. 411–433, 2010.

[18] D. Hariskos, S. Spiering, and M. Powalla, "Buffer layers in Cu(In,Ga)Se2 solar cells and modules," *Thin Solid Films*, vol. 480-481, pp. 99 – 109, 2005. {EMRS} 2004Proceedings of Symposium O on Thin Film Chalcogenide Photovoltaic Materials, {EMRS} 2004 Conference, Strasbourg, France, May 24-28, 2004.

[19] H. Hiroi, Y. Iwata, S. Adachi, H. Sugimoto, and A. Yamada, "New World-Record Efficiency for Pure-Sulfide Cu(In,Ga)S2 Thin-Film Solar Cell With Cd-Free Buffer Layer via KCN-Free Process," *IEEE Journal of Photovoltaics*, vol. PP, no. 99, pp. 1–4, 2016.

[20] D. Hariskos, B. Fuchs, R. Menner, N. Naghavi, C. Hubert, D. Lincot, and M. Powalla, "The Zn(S,O,OH)/ZnMgO buffer in thin-film Cu(In,Ga)(Se,S)2-based solar cells part II: Magnetron sputtering of the ZnMgO buffer layer for in-line co-evaporated Cu(In,Ga)Se2 solar cells," *Progress in Photovoltaics: Research and Applications*, vol. 17, no. 7, pp. 479–488, 2009.

[21] Z.-H. Li, E.-S. Cho, and S. J. Kwon, "Mg-doped ZnO thin films deposited by the atomic layer chemical vapor deposition for the buffer layer of CIGS solar cell," *Applied Surface Science*, vol. 314, pp. 97 – 103, 2014.

[22] Y. Ievskaya, R. Hoye, A. Sadhanala, K. Musselman, and J. MacManus-Driscoll, "Fabrication of ZnO/Cu2O heterojunctions in atmospheric conditions: Improved interface quality and solar cell performance," *Solar Energy Materials and Solar Cells*, vol. 135, pp. 43 – 48, 2015. EMRS 2014 Spring Meeting Advanced materials and characterization techniques for solar cells.

[23] T. Minami, Y. Nishi, T. Miyata, and S. Abe, "Photovoltaic Properties in Al-doped ZnO/non-doped Zn1-XMgXO/Cu2O Heterojunction Solar Cells," *ECS Transactions*, vol. 50, no. 51, pp. 59–68, 2013.

[24] K. Karthick and K. Vijayalakshmi, "Influence of Mg doping on the properties of ZnO films prepared on c-cut sapphire by sputtering," *Superlattices and Microstructures*, vol. 67, pp. 172 – 180, 2014.

[25] Y. E. Romanyuk, H. Hagendorfer, P. Stücheli, P. Fuchs, A. R. Uhl, C. M. Sutter-Fella, M. Werner, S. Haass, J. Stückelberger, C. Broussillou, P.-P. Grand, V. Bermudez, and A. N. Tiwari, "All Solution-Processed Chalcogenide Solar Cells - from Single Functional Layers Towards a 13.8% Efficient CIGS Device," *Advanced Functional Materials*, vol. 25, no. 1, pp. 12–27, 2015.

[26] S. E. Habas, H. A. S. Platt, M. F. A. M. van Hest, and D. S. Ginley, "Low-Cost Inorganic Solar Cells: From Ink To Printed Device," *Chemical Reviews*, vol. 110, no. 11, pp. 6571–6594, 2010. PMID: 20973478.

[27] R. Mikami, H. Miyazaki, T. Abe, A. Yamada, and M. Konagai, "Chemical bath deposited (CBD)-ZnO buffer layer for CIGS solar cells," in *Proceedings of 3rd World Conference on Photovoltaic Energy Conversion*, vol. 1, pp. 519–522 Vol.1, May 2003.

[28] A. Yamada, H. Miyazaki, Y. Chiba, and M. Konagai, "High-efficiency Cu(InGa)Se2 solar cells with a zinc-based buffer layer," *Thin Solid Films*, vol. 480-481, pp. 503 – 508, 2005. {EMRS} 2004Proceedings of Symposium O on Thin Film Chalcogenide Photovoltaic Materials, {EMRS} 2004 Conference, Strasbourg, France, May 24-28, 2004.

[29] A. Mang, K. Reimann, and S. Raebenacke, "Band gaps, crystal-field splitting, spin-orbit coupling, and exciton binding energies in ZnO under hydrostatic pressure," *Solid State Communications*, vol. 94, no. 4, pp. 251 – 254, 1995.

[30] D. Reynolds, D. Look, and B. Jogai, "Optically pumped ultraviolet lasing from ZnO," *Solid State Communications*, vol. 99, no. 12, pp. 873 – 875, 1996.

[31] T. Shibata, K. Unno, E. Makino, Y. Ito, and S. Shimada, "Characterization of sputtered ZnO thin film as sensor and actuator for diamond {AFM} probe," *Sensors and Actuators A: Physical*, vol. 102, no. 1-2, pp. 106 – 113, 2002.

[32] P. D. C. King, T. D. Veal, A. Schleife, J. Zuniga-Perez, B. Martel, P. H. Jefferson, F. Fuchs, V. Munoz-Sanjose, F. Bechstedt, and C. F. McConville, "Valence-band electronic structure of CdO, ZnO, and MgO from x-ray photoemission spectroscopy and quasi-particle-corrected density-functional theory calculations," *Phys. Rev. B*, vol. 79, p. 205205, May 2009.

[33] A. Kaushal and D. Kaur, "Effect of Mg content on structural, electrical and optical properties of Zn 1- xMgxO nanocomposite thin films," *Solar Energy Materials and Solar Cells*, vol. 93, no. 2, pp. 193–198, 2009.

[34] S. Desgreniers, "High-density phases of ZnO: Structural and compressive parameters," *Phys. Rev. B*, vol. 58, pp. 14102–14105, Dec 1998.

[35] C. Jagadish and S. Pearton, *Zinc Oxide Bulk, Thin Films and Nanostructures: Processing, Properties, and Applications*. No. 1-6, Elsevier Science, 2011.

[36] W.-J. Li, E.-W. Shi, W.-Z. Zhong, and Z.-W. Yin, "Growth mechanism and growth habit of oxide crystals," *Journal of Crystal Growth*, vol. 203, no. 1-2, pp. 186 – 196, 1999.

[37] P. V. Balachandran, J. Theiler, J. M. Rondinelli, and T. Lookman, "Materials Prediction via Classification Learning," *Scientific reports*, vol. 5, 2015.

[38] S. Das, K. Dutta, and A. Pramanik, "Morphology control of ZnO with citrate: a time and concentration dependent mechanistic insight," *CrystEngComm*, vol. 15, pp. 6349–6358, 2013.

[39] S. Fujii, A. Tomozawa, E. Fujii, H. Torii, R. Takayama, and T. Hirao, "Preparation of La modified PbTiO3 thin films on the oxide buffer layers with NaCl type structure," *Applied Physics Letters*, vol. 65, no. 11, pp. 1463–1465, 1994.

[40] R. D. Shannon, "Revised effective ionic radii and systematic studies of interatomic distances in halides and chalcogenides," *Acta Crystallographica Section A*, vol. 32, no. 5, pp. 751–767, 1976.

[41] L. A. Bendersky, I. Takeuchi, K.-S. Chang, W. Yang, S. Hullavarad, and R. D. Vispute, "Microstructural study of epitaxial Zn1-xMgxO composition spreads," *Journal of Applied Physics*, vol. 98, no. 8, 2005.

[42] I. V. Maznichenko, A. Ernst, M. Bouhassoune, J. Henk, M. Däne, M. Lüders, P. Bruno, W. Hergert, I. Mertig, Z. Szotek, and W. M. Temmerman, "Structural phase transitions and fundamental band gaps of $Mg_xZn_{1-x}O$ alloys from first principles," *Phys. Rev. B*, vol. 80, p. 144101, Oct 2009.

[43] T. A. Wassner, B. Laumer, S. Maier, A. Laufer, B. K. Meyer, M. Stutzmann, and M. Eickhoff, "Optical properties and structural characteristics of ZnMgO grown by plasma assisted molecular beam epitaxy," *Journal of Applied Physics*, vol. 105, no. 2, 2009.

[44] G. Vijayaprasath, M. Manikandan, M. Arivananhan, M. Navaneethan, and Y. Hayakawa, "A Comparative Study on Pure and Mg Doped ZnO Nano Structured Thin Films," *Asian Journal of Chemistry*, vol. 25, 2013.

[45] A. Janotti and C. G. V. de Walle, "Fundamentals of zinc oxide as a semiconductor," *Reports on Progress in Physics*, vol. 72, no. 12, p. 126501, 2009.

[46] R. Swanepoel, "Determination of the thickness and optical constants of amorphous silicon," *Journal of Physics E: Scientific Instruments*, vol. 16, no. 12, p. 1214, 1983.

[47] P. Struk, T. Pustelny, and Z. Opilski, "Researches on the Spectral Transmittance of Zinc Oxide ZnO Semiconductor Layers," *Acta Physica Polonica A*, vol. 118, pp. 1239–1241, 12 2010.

[48] S. E. Harrison, "Conductivity and Hall Effect of ZnO at Low Temperatures," *Phys. Rev.*, vol. 93, pp. 52–62, Jan 1954.

[49] A. F. Kohan, G. Ceder, D. Morgan, and C. G. Van de Walle, "First-principles study of native point defects in ZnO," *Phys. Rev. B*, vol. 61, pp. 15019–15027, Jun 2000.

[50] S. B. Zhang, S.-H. Wei, and A. Zunger, "Intrinsic *n* -type versus *p* -type doping asymmetry and the defect physics of ZnO," *Phys. Rev. B*, vol. 63, p. 075205, Jan 2001.

[51] A. Janotti and C. G. Van de Walle, "Native point defects in ZnO," *Phys. Rev. B*, vol. 76, p. 165202, Oct 2007.

[52] Y. Liu, Y. Li, and H. Zeng, "ZnO-Based Transparent Conductive Thin Films: Doping, Performance, and Processing," *Journal of Nanomaterials*, 2013.

[53] C. G. V. de Walle, "Defect analysis and engineering in ZnO," *Physica B: Condensed Matter*, vol. 899, pp. 308–310, 2001. International Conference on Defects in Semiconductors.

[54] J. G. Reynolds and C. L. Reynolds, "Progress in ZnO Acceptor Doping: What Is the Best Strategy?," *Advances in Condensed Matter Physics*, vol. 2014, 2014.

[55] Y. Zeng, Z. Ye, W. Xu, J. Lu, L. Zhu, and B. Zhao, "Dopant source choice for formation of p-type ZnO: Li acceptor," *Applied Physics Letters*, vol. 88, no. 6, pp. 1–3, 2006.

[56] X.-L. Guo, J.-H. Choi, H. Tabata, and T. Kawai, "Fabrication and Optoelectronic Properties of a Transparent ZnO Homostructural Light-Emitting Diode," *Japanese Journal of Applied Physics*, vol. 40, no. 3A, p. L177, 2001.

[57] D. C. Look, D. C. Reynolds, C. W. Litton, R. L. Jones, D. B. Eason, and G. Cantwell, "Characterization of homoepitaxial p-type ZnO grown by molecular beam epitaxy," *Applied Physics Letters*, vol. 81, no. 10, pp. 1830–1832, 2002.

[58] S. Lany and A. Zunger, "Generalized Koopmans density functional calculations reveal the deep acceptor state of N_O in ZnO," *Phys. Rev. B*, vol. 81, p. 205209, May 2010.

[59] K. Thonke, M. Schirra, R. Schneider, A. Reiser, G. Prinz, M. Feneberg, J. Biskupek, U. Kaiser, and R. Sauer, "The role of stacking faults and their associated 0.13 ev acceptor state in doped and undoped ZnO layers and nanostructures," *Microelectronics Journal*, vol. 40, no. 2, pp. 210 – 214, 2009. Wide Band Gap Semiconductor Nanostructures for Optoelectronic Applications.

[60] J. L. Lyons, A. Janotti, and C. G. V. de Walle, "Chapter One - Theory and Modeling of Oxide Semiconductors," in *Oxide Semiconductors* (S. J. P. Bengt G. Svensson and C. Jagadish, eds.), vol. 88 of *Semiconductors and Semimetals*, pp. 1 – 37, Elsevier, 2013.

[61] J. Chen, W. Z. Shen, N. B. Chen, D. J. Qiu, and H. Z. Wu, "The study of composition non-uniformity in ternary MgxZn1-xO thin films," *Journal of Physics: Condensed Matter*, vol. 15, no. 30, p. L475, 2003.

[62] Zhang, X. D., Guo, M. L., Liu, C. L., Zhang, L. A., Zhang, W. Y., Ding, Y. Q., Wu, Q., and Feng, X., "First-principles investigation of electronic and optical properties in wurtzite Zn1-xMgxO," *Eur. Phys. J. B*, vol. 62, no. 4, pp. 417–421, 2008.

[63] M. Herman and H. Sitter, *Molecular Beam Epitaxy: Fundamentals and Current Status*. Springer Series in Materials Science, Springer Berlin Heidelberg, 2013.

[64] R. Eason, *Pulsed Laser Deposition of Thin Films: Applications-Led Growth of Functional Materials*. Wiley, 2007.

[65] K. Wasa, I. Kanno, and H. Kotera, *Handbook of Sputter Deposition Technology: Fundamentals and Applications for Functional Thin Films, Nano-materials and MEMS*. No. 14-22, William Andrew, 2012.

[66] H. Adachi and K. Wasa, "Thin Films and Nanomaterials," in *Handbook of Sputtering Technology (Second Edition)* (K. Wasa, , I. Kanno, , and H. Kotera, eds.), pp. 3 – 39, Oxford: William Andrew Publishing, second edition ed., 2012.

[67] H. Tanaka, S. Fujita, and S. Fujita, "Fabrication of wide-band-gap MgxZn1-xO quasi-ternary alloys by molecular-beam epitaxy," *Applied Physics Letters*, vol. 86, no. 19, 2005.

[68] J. Chen, W. Z. Shen, N. B. Chen, D. J. Qiu, and H. Z. Wu, "The study of composition non-uniformity in ternary MgxZn1-xO thin films," *Journal of Physics: Condensed Matter*, vol. 15, no. 30, p. L475, 2003.

[69] N. Pinna and M. Knez, *Atomic Layer Deposition of Nanostructured Materials*. Wiley, 2012.

[70] J. Van Delft, D. Garcia-Alonso, and W. Kessels, "Atomic layer deposition for photovoltaics: applications and prospects for solar cell manufacturing," *Semiconductor Science and Technology*, vol. 27, no. 7, p. 074002, 2012.

[71] S. Lindroos and M. Leskelä, *Successive Ionic Layer Adsorption and Reaction (SILAR) and Related Sequential Solution-Phase Deposition Techniques*, ch. 8, pp. 239–282. John Wiley & Sons, Inc., 2008.

[72] M. Paunovic and M. Schlesinger, *Fundamentals of Electrochemical Deposition*. The ECS Series of Texts and Monographs, Wiley, 2006.

[73] D. Perednis and L. J. Gauckler, "Thin film deposition using spray pyrolysis," *Journal of electroceramics*, vol. 14, no. 2, pp. 103–111, 2005.

[74] L. Znaidi, "Sol-gel-deposited ZnO thin films: A review," *Materials Science and Engineering: B*, vol. 174, no. 1-3, pp. 18 – 30, 2010. Advances in Semiconducting Materials.

[75] A. Yang, H. Wei, X. Liu, H. Song, G. Zheng, Y. Guo, C. Jiao, S. Yang, Q. Zhu, and Z. Wang, "Synthesis and characterization of well-aligned Zn1-xMgxO nanorods and film by metal organic chemical vapor deposition," *Journal of Crystal Growth*, vol. 311, no. 2, pp. 278 – 281, 2009.

[76] L. Guo, "Characterization of MgxZn1-xO Films Grown by Electrochemical Deposition," in *Advanced Materials Research*, vol. 926, pp. 22–25, Trans Tech Publ, 2014.

[77] H. Zhang, T. Zhao, G. Hu, L. Miao, and Y. Yang, "Role of Mg doping on morphology and photoluminescence features of MgxZn1-xO films prepared by ultrasonic spray pyrolysis," *Journal of Materials Science: Materials in Electronics*, vol. 23, no. 11, pp. 1933–1937, 2012.

[78] S. Fujihara, C. Sasaki, and T. Kimura, "Effects of Li and Mg doping on microstructure and properties of sol-gel ZnO thin films," *Journal of the European Ceramic Society*, vol. 21, no. 10-11, pp. 2109 – 2112, 2001.

[79] T. Yasuda, T. Sakurai, and A. Kikawada, "Synthesis of ZnO/MgZnO multilayer films by sol-gel dip method," *physica status solidi (c)*, vol. 11, no. 7-8, pp. 1365–1368, 2014.

[80] S. Chawla, K. Jayanthi, and H. Chander, "Enhancement of luminescence in ZnMgO thin-film nanophosphors and application for white light generation," *physica status solidi (a)*, vol. 205, no. 2, pp. 271–274, 2008.

[81] İ. Polat, S. Yılmaz, E. Bacaksız, Y. Atasoy, and M. Tomakin, "Synthesis and fabrication of Mg-doped ZnO-based dye-synthesized solar cells," *Journal of Materials Science: Materials in Electronics*, vol. 25, no. 7, pp. 3173–3178, 2014.

[82] R. Maekawa, H. Suto, T. Sakai, and M. Ishikiriyama, "Preparation of Zn1-xMgxO films with high Mg content by novel chemical bath deposition," *Journal of Materials Science*, vol. 50, no. 11, pp. 3956–3961, 2015.

[83] I. Dharmadasa, *Advances in Thin-Film Solar Cells*. Pan Stanford, 2012.

[84] U. Rau, D. Abou-Ras, and T. Kirchartz, *Advanced Characterization Techniques for Thin Film Solar Cells*. Wiley, 2011.

[85] R. E. Brandt, M. Young, H. H. Park, A. Dameron, D. Chua, Y. S. Lee, G. Teeter, R. G. Gordon, and T. Buonassisi, "Band offsets of n-type electron-selective contacts on cuprous oxide (Cu2O) for photovoltaics," *Applied Physics Letters*, vol. 105, no. 26, p. 263901, 2014.

[86] S. Kim, C.-S. Lee, S. Kim, R. B. V. Chalapathy, E. A. Al-Ammar, and B. T. Ahn, "Understanding the light soaking effect of ZnMgO buffer in CIGS solar cells," *Physical Chemistry Chemical Physics (Incorporating Faraday Transactions)*, vol. 17, pp. 19222–19229, 2015.

[87] Y. Hou, Z. Mei, and X. Du, "Semiconductor ultraviolet photodetectors based on ZnO and MgxZn1-xO," *Journal of Physics D: Applied Physics*, vol. 47, no. 28, p. 283001, 2014.

[88] K. Liu, D. Shen, C. Shan, J. Zhang, D. Jiang, Y. Zhao, B. Yao, and D. Zhao, "The growth of ZnMgO alloy films for deep ultraviolet detection," *Journal of Physics D: Applied Physics*, vol. 41, no. 12, p. 125104, 2008.

[89] K. Koike, D. Takagi, M. Kawasaki, T. Hashimoto, T. Inoue, K. ichi Ogata, S. Sasa, M. Inoue, and M. Yano, "Ion-Sensitive Characteristics of an Electrolyte-Solution-Gate ZnO/ZnMgO Heterojunction Field-Effect Transistor as a Biosensing Transducer," *Japanese Journal of Applied Physics*, vol. 46, no. 10L, p. L865, 2007.

[90] H. Wu, J. Liang, G. Jin, Y. Lao, and T. Xu, "Transparent Thin-Film Transistors Using ZnMgO as Dielectrics and Channel," *IEEE Transactions on Electron Devices*, vol. 54, pp. 2856–2859, Nov 2007.

[91] H.-C. Hsu, C.-Y. Wu, H.-M. Cheng, and W.-F. Hsieh, "Band gap engineering and stimulated emission of ZnMgO nanowires," *Applied Physics Letters*, vol. 89, no. 1, 2006.

[92] G. Bruckmann, "Darstellung und Eigenschaften dünner Bleisulfid-Schichten unter besonderer Berücksichtigung ihrer Detektorwirkung, II," *Kolloid-Zeitschrift*, vol. 65, no. 2, pp. 148–161.

[93] C. Brundle, C. Evans, and S. Wilson, *Encyclopedia of Materials Characterization: Surfaces, Interfaces, Thin Films*. Characterization Series, Butterworth-Heinemann, 1992.

[94] C. R. R. Nave, "Michelson Interferometer." http://hyperphysics.phy-astr.gsu.edu/hbase/phyopt/michel.html. Accessed: 2016-04-07.

[95] M. E. Sanchez-Vergara, J. C. Alonso-Huitron, A. Rodriguez-Gomez, and J. N. Reider-Burstin, "Determination of the Optical GAP in Thin Films of Amorphous Dilithium Phthalocyanine Using the Tauc and Cody Models," *Molecules*, vol. 17, no. 9, p. 14, 2012.

[96] Delaware Mineralogical Society, "Bragg's law diagram." http://www.delminsociety.net/motm/motm_mar2007.shtml. Accessed: 2016-07-04.

[97] J. Speight, *Lange's Handbook of Chemistry, 70th Anniversary Edition*. McGraw-Hill Standard Handbooks, McGraw-Hill Companies,Incorporated, 2004.

[98] G. Hodes, *Chemical Solution Deposition Of Semiconductor Films*. CRC Press, 2002.

[99] P. O'Brien and J. McAleese, "Developing an understanding of the processes controlling the chemical bath deposition of ZnS and CdS," *J. Mater. Chem.*, vol. 8, pp. 2309–2314, 1998.

[100] M. Kokotov, A. Biller, and G. Hodes, "Reproducible Chemical Bath Deposition of ZnO by a One-Step Method: The Importance of Contaminants in Nucleation," *Chemistry of Materials*, vol. 20, no. 14, pp. 4542–4544, 2008.

[101] M. Ohyama, H. Kouzuka, and T. Yoko, "Sol-gel preparation of ZnO films with extremely preferred orientation along (002) plane from zinc acetate solution," *Thin Solid Films*, vol. 306, no. 1, pp. 78 – 85, 1997.

[102] S. Yamabi and H. Imai, "Growth conditions for wurtzite zinc oxide films in aqueous solutions," *J. Mater. Chem.*, vol. 12, pp. 3773–3778, 2002.

[103] M. Kuwabara, "Effect of Seed Layer on the Orientation of Zinc Oxide Film on Silicon Substrate," *Journal of Materials Science & Technology*, vol. 6, p. 023, 2005.

[104] L. E. Greene, M. Law, J. Goldberger, F. Kim, J. C. Johnson, Y. Zhang, R. J. Saykally, and P. Yang, "Low-temperature wafer-scale production of ZnO nanowire arrays," *Angewandte Chemie*, vol. 115, no. 26, pp. 3139–3142, 2003.

[105] P. Fuchs, H. Hagendorfer, Y. E. Romanyuk, and A. N. Tiwari, "Doping strategies for highly conductive Al-doped ZnO films grown from aqueous solution," *physica status solidi (a)*, vol. 212, no. 1, pp. 51–55, 2015.

[106] C. Mortimer and U. Müller, *Chemie: das Basiswissen der Chemie ; 126 Tabellen*. No. 290-298, Thieme, 2007.

[107] K. D. M. . e. a. Ernits, K.; Muska, "Anion Effect of Zinc Source on Chemically Deposited ZnS(O,OH) Films," *Advances in Materials Science and Engineering*, 2009.

[108] O'Brien, P.; Govender, K.; Boyle, D.S.; Kenway, P.B., "Understanding the factors that govern the depostion and morphology of thin films of ZnO from Aqueous solution," *Journal of Materials Chemistry*, vol. 14, pp. 2575–2591, 2004.

[109] B. Sharma, *Objective Question Bank in Chemistry Doping strategies for highly conductive Al-doped ZnO films grown from aqueous solution*. Krishna Prakashan, 1997.

[110] F. V. Molefe, L. F. Koao, B. F. Dejene, and H. C. Swart, "Phase formation of hexagonal wurtzite ZnO through decomposition of Zn(OH)2 at various growth temperatures using {CBD} method," *Optical Materials*, vol. 46, pp. 292 – 298, 2015.

[111] V. Strano, R. G. Urso, M. Scuderi, K. O. Iwu, F. Simone, E. Ciliberto, C. Spinella, and S. Mirabella, "Double Role of HMTA in ZnO Nanorods Grown by Chemical Bath Deposition," *The Journal of Physical Chemistry C*, vol. 118, no. 48, pp. 28189–28195, 2014.

[112] K. Govender, D. S. Boyle, P. B. Kenway, and P. O'Brien, "Understanding the factors that govern the deposition and morphology of thin films of ZnO from aqueous solution," *J. Mater. Chem.*, vol. 14, pp. 2575–2591, 2004.

[113] H.-C. Cheng, C.-F. Chen, C.-Y. Tsay, and J.-P. Leu, "High oriented ZnO films by sol-gel and chemical bath deposition combination method," *Journal of Alloys and Compounds*, vol. 475, no. 1-2, pp. L46 – L49, 2009.

[114] K. M. McPeak, T. P. Le, N. G. Britton, Z. S. Nickolov, Y. A. Elabd, and J. B. Baxter, "Chemical Bath Deposition of ZnO Nanowires at Near-Neutral pH Conditions without Hexamethylenetetramine (HMTA): Understanding the Role of HMTA in ZnO Nanowire Growth," *Langmuir*, vol. 27, no. 7, pp. 3672–3677, 2011. PMID: 21361384.

[115] J. J. Richardson and F. F. Lange, "Controlling Low Temperature Aqueous Synthesis of ZnO. 1. Thermodynamic Analysis," *Crystal Growth & Design*, vol. 9, no. 6, pp. 2570–2575, 2009.

[116] H. Khallaf, G. Chai, O. Lupan, H. Heinrich, S. Park, A. Schulte, and L. Chow, "Investigation of chemical bath deposition of ZnO thin films using six different complexing agents," *Journal of Physics D: Applied Physics*, vol. 42, no. 13, p. 135304, 2009.

[117] S. Cho, J.-W. Jang, S.-H. Jung, B. R. Lee, E. Oh, and K.-H. Lee, "Precursor Effects of Citric Acid and Citrates on ZnO Crystal Formation," *Langmuir*, vol. 25, no. 6, pp. 3825–3831, 2009.

[118] Nicholas, N. J.; Franks, G.V.; Ducker, W.A., "Selective Adsorption to Particular Crystal Faces of ZnO," *Langmuir*, vol. 28, pp. 7189–7196, 2012.

[119] R. Cornelis, *Handbook of Elemental Speciation II: Species in the Environment, Food, Medicine and Occupational Health*. Handbook of Elemental Speciation II: Species in the Environment, Food, Medicine and Occupational Health, Wiley, 2005.

[120] J. P. Gustafsson, "Visual MINTEQ, ver. 3.0.," October 2012.

[121] Ignasi, "MEDUSA: Make Equilibrium Diagrams Using Sophisticated Algorithms." www.kemi.kth.se/medusa, December 2010.

[122] "Critically Selected Stability Constants of Metal Complexes Database." Compiled by Smith, R. M.; Martell, A. E.; Motekaitis, R. J. Version 7.0 for Windows., 2003.

[123] I. Puigdomenech, "Hydrochemical Equilibrium-Constant Database," Aug. 2009.

[124] S. Pawar, B. Pawar, J. Kim, O.-S. Joo, and C. Lokhande, "Recent status of chemical bath deposited metal chalcogenide and metal oxide thin films," *Current Applied Physics*, vol. 11, no. 2, pp. 117 – 161, 2011.

[125] "Stability Constants Database and Mini-SCDatabase." IUPAC and Academic Software Version 5.3, 2003.

[126] P. Gans, A. Sabatini, and A. Vacca, "Hyperquad Simulation and Speciation," 2009.

[127] L. G. Sillen and A. E. A. E. Martell, *Stability constants of metal-ion complexes : supplement*. London : Chemical Society, 1971. Supplement to 2nd edition.

[128] A. Degen and M. Kosec, "Effect of pH and impurities on the surface charge of zinc oxide in aqueous solution," *Journal of the European Ceramic Society*, vol. 20, no. 6, pp. 667 – 673, 2000.

[129] M. Kosmulski, *Chemical Properties of Material Surfaces*. Surfactant Science, CRC Press, 2001.

[130] . Dmytro S. Golovko, R. Munoz-Espi , and G. Wegner, "Interaction between Poly(styrene acrylic acid) Latex Nanoparticles and Zinc Oxide Surfaces," *Langmuir*, vol. 23, no. 7, pp. 3566–3569, 2007. PMID: 17315902.

[131] X. Zhou, Q. Kuang, Z.-Y. Jiang, . Zhao-Xiong Xie, T. Xu, R.-B. Huang, , and L.-S. Zheng, "The Origin of Green Emission of ZnO Microcrystallites:â%■ Surface-Dependent Light Emission Studied by Cathodoluminescence," *The Journal of Physical Chemistry C*, vol. 111, no. 32, pp. 12091–12093, 2007.

[132] T. Shinagawa, K. Shibata, O. Shimomura, M. Chigane, R. Nomura, and M. Izaki, "Solution-processed high-haze ZnO pyramidal textures directly grown on a TCO substrate and the light-trapping effect in Cu2O solar cells," *J. Mater. Chem. C*, vol. 2, pp. 2908–2917, 2014.

[133] J. Joo, B. Y. Chow, M. Prakash, E. S. Boyden, and J. M. Jacobson, "Face-selective electrostatic control of hydrothermal zinc oxide nanowire synthesis," *Nature materials*, vol. 10, no. 8, pp. 596–601, 2011.

[134] W.-J. Li, E.-W. Shi, W.-Z. Zhong, and Z.-W. Yin, "Growth mechanism and growth habit of oxide crystals," *Journal of Crystal Growth*, vol. 203, no. 1-2, pp. 186 – 196, 1999.

[135] Dimopoulos, T., Peic, A., Abermann, S., Postl, M., List-Kratochvil, E. J.W., and Resel, R., "Effect of thermal annealing in vacuum on the photovoltaic properties of electrodeposited Cu2O-absorber solar cell," *EPJ Photovolt.*, vol. 5, p. 50301, 2014.